

Teske, A., Lizarralde, D., Höfig, T.W., and the Expedition 385 Scientists *Proceedings of the International Ocean Discovery Program* Volume 385 publications.iodp.org







Expedition 385 summary¹

Contents

- 1 Abstract
- 2 Introduction
- 4 Background
- 7 Site summaries
- **40** Preliminary scientific assessment
- 45 References

Keywords

International Ocean Discovery Program, IODP, JOIDES Resolution, Expedition 385, Guaymas Basin Tectonics and Biosphere, Gulf of California, Site U1545, Site U1546, Site U1547, Site U1548, Site U1549, Site U1550, Site U1551, Site U1552, Biosphere Frontiers, off-axis, on-axis, Ringvent, hydrothermal activity, heat flow, sill emplacement, thermal alteration, mineralization, contact aureole, hydrocarbon, methane, seepage, carbon budget, cell counts, subsurface biosphere spreading center, transect, sedimentation, hydrothermal alteration, thermal gradient, doleritic sill, thermal aureole, carbon source, carbon sink, organic matter

Core descriptions

Supplementary material

References (RIS)

MS 385-101 Published 27 September 2021

Funded by NSF OCE1326927

A. Teske, D. Lizarralde, T.W. Höfig, I.W. Aiello, J.L. Ash, D.P. Bojanova, M.D. Buatier, V.P. Edgcomb, C.Y. Galerne, S. Gontharet, V.B. Heuer, S. Jiang, M.A.C. Kars, S. Khogenkumar Singh, J.-H. Kim, L.M.T. Koornneef, K.M. Marsaglia, N.R. Meyer, Y. Morono, R. Negrete-Aranda, F. Neumann, L.C. Pastor, M.E. Peña-Salinas, L.L. Pérez Cruz, L. Ran, A. Riboulleau, J.A. Sarao, F. Schubert, J.M. Stock, L.M.A.A. Toffin, W. Xie, T. Yamanaka, and G. Zhuang²

¹Teske, A., Lizarralde, D., Höfig, T.W., Aiello, I.W., Ash, J.L., Bojanova, D.P., Buatier, M.D., Edgcomb, V.P., Galerne, C.Y., Gontharet, S., Heuer, V.B., Jiang, S., Kars, M.A.C., Khogenkumar Singh, S., Kim, J.-H., Koornneef, L.M.T., Marsaglia, K.M., Meyer, N.R., Morono, Y., Negrete-Aranda, R., Neumann, F., Pastor, L.C., Peña-Salinas, M.E., Pérez Cruz, L.L., Ran, L., Riboulleau, A., Sarao, J.A., Schubert, F., Stock, J.M., Toffin, L.M.A.A., Xie, W., Yamanaka, T., and Zhuang, G., 2021. Expedition 385 summary. *In* Teske, A., Lizarralde, D., Höfig, T.W., and the Expedition 385 Scientists, *Guaymas Basin Tectonics and Biosphere*. Proceedings of the International Ocean Discovery Program, 385: College Station, TX (International Ocean Discovery Program). https://doi.org/10.14379/iodp.proc.385.101.2021

² Expedition 385 Scientists' affiliations.

1. Abstract

International Ocean Discovery Program Expedition 385 drilled organic-rich sediments and intruded sills in the off-axis region and axial graben of the northern spreading segment of Guaymas Basin, a young marginal seafloor spreading system in the Gulf of California. Guaymas Basin is characterized by high heat flow and magmatism in the form of sill intrusions into sediments, which extends tens of kilometers off axis, in contrast with the localized volcanism found at most mid-ocean ridge spreading centers. Sill intrusions provide transient heat sources that mobilize buried sedimentary carbon, in part as methane and other hydrocarbons, and drive hydrothermal circulation. The resulting thermal and geochemical gradients shape abundance, composition, and activity of the deep subsurface biosphere of the basin.

Drill sites extend over a broad region of Guaymas Basin. Adjacent Sites U1545 and U1546, located ~52 km northwest of the northern Guaymas Basin axial graben, recovered sediment successions to ~540 meters below seafloor (mbsf) (equivalent to the core depth below seafloor, Method A [CSF-A] scale), including a thin sill (a few meters thick) drilled near the bottom of Site U1545 and a massive sill (~355-430 mbsf) at Site U1546 that chemically and physically affects the surrounding sediments. Sites U1547 and U1548, located ~27 km northwest of the axial graben, were drilled to investigate an active sill-driven hydrothermal system evident at the seafloor as an 800 m wide, circular bathymetric high called Ringvent because of its outline of a ring of active vent sites. Ringvent is underlain by a thick sill at shallow depth (Site U1547). Geothermal gradients steepen toward the Ringvent periphery (Holes U1548A-U1548C), and the zones of authigenic carbonate precipitation and of highest microbial cell abundance correspondingly shallow toward the periphery. The underlying sill was drilled several times and yielded diverse igneous rock textures, sediment/sill interfaces, and alteration minerals in veins and vesicles. The Ringvent sill became the target of an integrated, interdisciplinary sampling and research effort that included geological, geochemical, and microbiological components. The thermal, lithologic, geochemical, and microbiological contrasts between the northwestern sites (U1545 and U1546) and the Ringvent sites (U1547 and U1548) form the core scientific observations informing the direct influence of sillsediment interaction. These observations are supplemented by results from sites that exhibit persistent influence of thermally equilibrated sill intrusions, including supporting long-lived methane cold seeps, as observed at off-axis Sites U1549 and U1552, and the persistent geochemical record of hydrocarbon formation near the sill/sediment contact, as observed at the northern axial trough Site U1550, which confirms observations from Deep Sea Drilling Project (DSDP) Leg 64. Drilling at Site U1551 ~29 km southeast of the axial graben was not successful due to unstable shallow

sands, but it confirmed the dominant influence of gravity-flow sedimentation processes southeast of the axial graben.

The scientific outcomes of Expedition 385 will (1) revise long-held assumptions about the role of sill emplacement in subsurface carbon mobilization versus carbon retention, (2) comprehensively examine the subsurface biosphere of Guaymas Basin and its responses and adaptations to hydrothermal conditions, (3) redefine hydrothermal controls on authigenic mineral formation in sediments, and (4) yield new insights into the long term influence of sill-sediment interaction on sediments deposited at the earliest stages of seafloor spreading, that is, when spreading centers are proximal to a continental margin. The generally high quality and high degree of completeness of the shipboard data sets present opportunities for inter- and multidisciplinary collaborations during shore-based studies. In comparison to DSDP Leg 64 to Guaymas Basin in 1979, continuous availability of sophisticated drilling strategies (e.g., the advanced piston corer [APC] and half-length APC systems) and numerous analytical innovations greatly improved sample recovery and scientific yield, particularly in the areas of organic geochemistry and microbiology. For example, microbial metagenomics did not exist 40 y ago. However, these technical refinements do not change the fact that Expedition 385 in many respects builds on the foundations of understanding laid by Leg 64 drilling in Guaymas Basin.

2. Introduction

Guaymas Basin is a young marginal rift basin characterized by active seafloor spreading and rapid sediment deposition, including organic-rich sediments derived from biologically highly productive overlying waters and terrigenous sediments from nearby continental margins (van Andel, 1964) (Figure F1). The combination of active seafloor spreading and rapid sedimentation within a narrow basin results in a dynamic environment where linked physical, chemical, and biological processes regulate the cycling of sedimentary carbon (Figure F2). This continuum of interrelating processes from magma to microbe motivated International Ocean Discovery Program (IODP) Expedition 385 and is reflected in its title, "Guaymas Basin Tectonics and Biosphere."

Formation of new igneous crust in Guaymas Basin involves the intrusion of sills into sedimentary sequences (Einsele et al., 1980; Saunders et al., 1982). Heat introduced by intruding sills releases CO_2 , CH_4 , low molecular weight (LMW) organic acids, and petroleum from organic-rich sediments and drives fluid advection through sill-sediment sequences that can release these thermogenic products toward the sediment–seawater interface (Von Damm et al., 1985; Whelan and Hunt, 1982; Kawka and Simoneit, 1987; Didyk and Simoneit, 1989; Martens, 1990; Peter et al., 1991). Thermal and chemical gradients linked to gas and fluid seepage create environments rich in chemical energy that supports microbial life at and below the seafloor (Teske et al., 2014). These microbes in turn participate in chemical transformations that influence the stability and transport of carbon in subsurface biospheres. Collectively, these physical, chemical, and biological processes have implications for the exchange of heat and mass between the lithosphere and overlying seawater column and may determine the long-term fate of carbon accumulation in organic-rich sediments in new ocean basins.

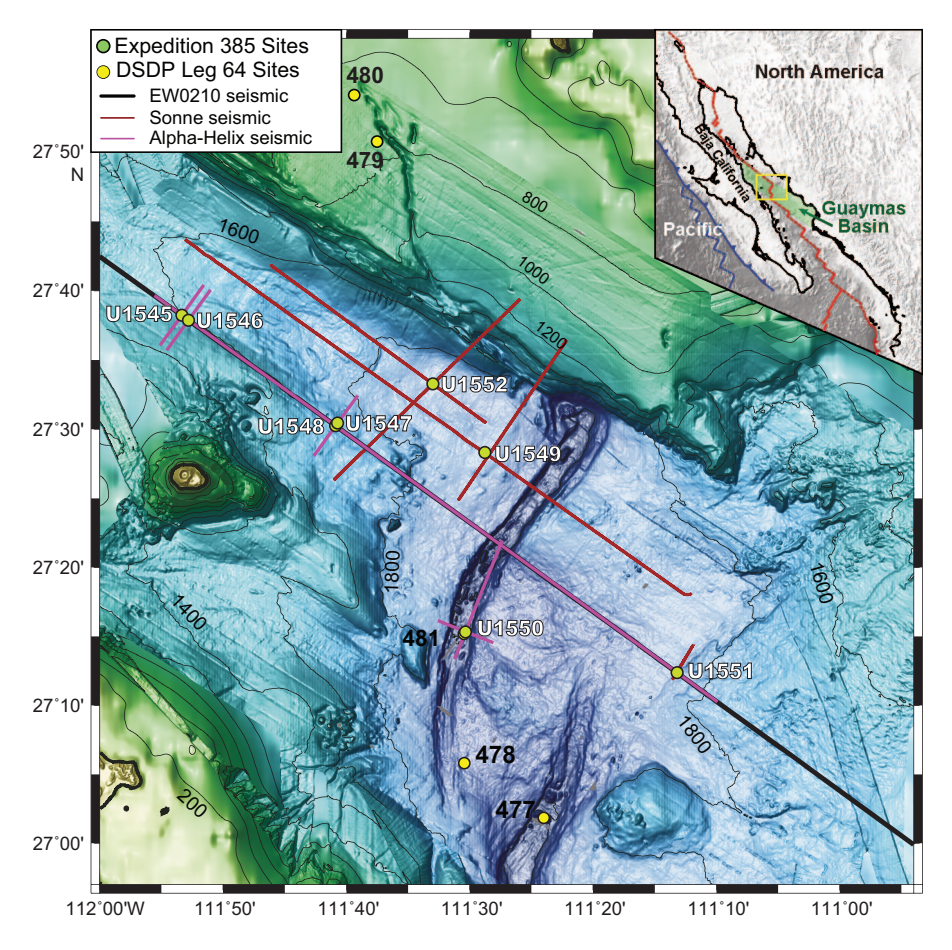


Figure F1. Bathymetry of Guaymas Basin with Baja California in the southwest and the Sonora margin in the northeast, showing all DSDP Leg 64 and IODP Expedition 385 sites drilled in the area. Seismic = seismic transects conducted prior to Expedition 385. Inset: tectonic setting of the Gulf of California; green shading = Guaymas Basin; blue box = main figure area. Contour lines = 200 m. DSDP = Deep Sea Drilling Project.

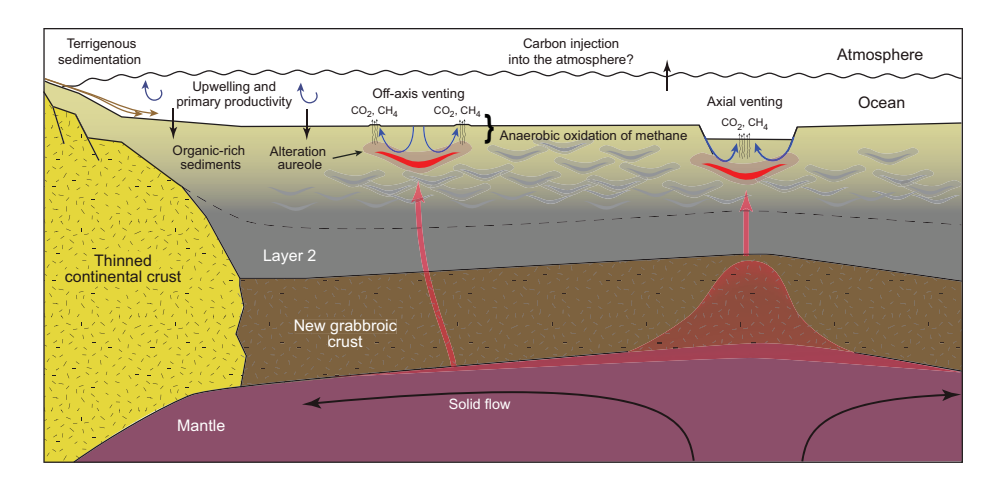


Figure F2. Conceptual model of interacting tectonic, igneous, sedimentological, and microbial processes at work in Guaymas Basin and the associated carbon pathways.

3. Background

3.1. Geological and microbiological roles in carbon cycling

The Gulf of California is a narrow sea that formed through continental rifting between the Baja California Peninsula and the western margin of mainland Mexico (Figure **F1**, inset), starting when the Baja Peninsula began to separate from North America at ~12–15 Ma (Stock and Lee, 1994). At present, the gulf is made up of a number of narrow spreading segments separated by transform faults that together represent the northern extent of the East Pacific Rise plate boundary (Figure **F1**, inset). Most of these segments have rifted to completion, including the northern Guaymas Basin spreading segment, where seismic observations indicate that continental rupture was complete by ~7 Ma and that new igneous crust formation has been accommodating Pacific/North American plate motion since that time (Lizarralde et al., 2007; Miller and Lizarralde, 2013).

The combination of distinct sedimentation patterns as well as active tectonics and magmatism in the Gulf of California creates a rich environment for scientific discovery. Sedimentation and sediment thickness in the basins of the Gulf of California vary substantially from the very thick (>4 km) sediments blanketing Wagner, Tiburón, and Delfin Basins in the northernmost part of the gulf (e.g., Persaud et al., 2003; González-Fernández et al., 2005) to Alarcón Basin in the southern part of the gulf, where the spreading center is only thinly sedimented (e.g., Sutherland et al., 2012). The northern Guaymas Basin segment, the focus of Expedition 385, lies between these extremes, and both sediment deposition and sediment type vary significantly within the segment. Sedimentation in the northwestern half of the segment is dominantly biogenic and driven by highly productive waters with minor terrigenous input from the arid Baja California Peninsula (Calvert, 1966). In contrast, sedimentation in the southeastern portion of the basin is dominated by terrigenous input from the Yaqui River delta system of the Sonora margin, and the ~200 m deep graben that defines the plate boundary in this segment tends to confine the turbidites from the Yaqui system to the southeastern horst region.

Scientific drilling in Guaymas Basin has a profound history. Sites drilled in Guaymas Basin during Deep Sea Drilling Project (DSDP) Leg 64 were motivated by both accessing the sediments themselves and by investigating the interaction of these sediments with magmatic processes. DSDP Sites 479 and 480 on the Sonora margin "focused on the paleoceanography of laminated, homogeneous, diatom-rich, anoxic sediments within the zone of low oxygen" typical of this setting (Shipboard Scientific Party, 1982). Sites 477, 478, and 481 within the spreading segments were drilled to investigate "the nature of young ocean crust in the Guaymas Basin, where high accumulation rates are common and variable high heat flow indicates active rifting and hydrothermal activity" (Kelts et al., 1982; Shipboard Scientific Party, 1982). The scientific results from Leg 64 contributed substantially to our understanding of the hydrothermal and geochemical processes that accompany igneous intrusions into sediments (Curray et al., 1979; Curray, Moore, et al., 1982; Einsele et al., 1980; Gieskes et al. 1982). Leg 64 results documented important changes in the sediments due to sill intrusion, including the expulsion of pore fluids and decreased porosity (Einsele, 1982), the breakdown and creation of organic compounds (Galimov and Simoneit, 1982; Simoneit and Bode, 1982), and the dissolution of primary mineral phases and the formation of secondary ones (Kastner, 1982), demonstrating that both temperature and vigor of fluid flow through the alteration zone are important factors in alteration processes.

At the time of Leg 64, it was believed that active magmatic emplacement was confined to the spreading centers (Einsele et al., 1980), and most of the subsequent work studying high-temperature biogeochemical processes in Guaymas Basin has been focused on the axial troughs. There is now strong evidence that magmatic intrusion into sediments occurs broadly throughout the basin, to more than 50 km off axis (Lizarralde et al., 2011) (Figure F3). Magmatism that is not confined to the spreading axis but instead is distributed throughout Guaymas Basin challenges models for the natural sequestration of carbon in sediments, the formation of oceanic crust at the earliest evolutionary stages of a spreading center, and life in the subsurface in marginal rift basins. Broadly distributed magmatism expands the fraction of organic-rich sediments that may be subject to thermal alteration and associated carbon release, potentially limiting the role of rift basin sedimentation in the long-term removal of atmospheric CO₂ (Figure F2). Differences in sub-

surface hydrology and thermal gradients in off-axis environments relative to the fault-bounded spreading center expand the range of environments that may support hydrocarbon generation and microbial populations in the subsurface.

The impact of sill-driven thermogenic sediment alteration on carbon cycling extends to regions of large igneous province (LIP) formation. It has been postulated that the Paleocene/Eocene Thermal Maximum (PETM) was driven by widespread carbon release caused by numerous sill intrusions into existing sedimentary basins during the formation of the North Atlantic Igneous Province (Svensen et al., 2004; Higgins and Schrag, 2006). Sill-sediment processes have similarly been implicated in other global-scale environmental crises, for example by linking the Permian—Triassic and Early Jurassic extinctions to the Siberian Traps and the Karoo Traps LIP events (Svensen et al., 2004, 2007, 2009a, 2009b; Sell et al., 2014; Galerne and Hasenclever, 2019), respectively. In addition, Cretaceous ocean anoxia events have been linked to concurrent submarine magmatism such as in the Caribbean (Turgeon and Creaser, 2008; Bralower, 2008). Guaymas Basin provides a modern analog to many aspects of these events.

The fate of carbon deposited in Guaymas Basin and in similar marginal basins across the world during punctuated episodes of regional magmatism depends on the relative efficiencies of interacting physical, chemical, and microbial processes, some working to sequester carbon and others working to release carbon back to the ocean and atmosphere (Figure F2). The physical and chemical processes immediately driven by a sill intrusion event include thermal heating of sediments by the intruding sill, thermal cracking of organic compounds within sediments, mineral dehydration and dissolution, pore space desiccation, contact metamorphism and potentially partial melting of the host sediment, and hydrothermal fluid convection (Simoneit et al., 1978, 1981; Simoneit and Lonsdale, 1982; Saxby and Stephenson, 1987; Kastner, 1982; Fisher and Narasimhan, 1991; Aarnes et al., 2010, 2011, 2015; Iyer et al. 2013, 2017; Galerne and Hasenclever, 2019). The dominant thermogenic alteration products resulting from sills intruding into organic-rich sediments are methane and CO₂ (Galimov and Simoneit, 1982; Seewald et al., 1990). For the Jurassic Karoo LIP event, quantitative modeling recently estimated a total degassing of ~22.3 10³ Gt of thermogenic methane during the 500,000 y of Karoo magmatism, showing that degassing rates peaking above 100 Mt/y could be sustained over a period of 5,000–60,000 y (Galerne and Hasenclever, 2019).

The extent and function of the deep subsurface biosphere in these settings has not been probed since Leg 64 demonstrated microbial methanogenesis in Guaymas Basin subsurface sediments; this was the first time that microbiological studies were performed during a deep-sea drilling expedition (Oremland et al., 1982; Galimov and Simoneit, 1982; Whelan et al., 1988). Because the present project has a strong microbiological research component, we briefly summarize how studies of pure cultures and natural enrichments from near-surface hydrothermal sediments of Guaymas Basin, usually obtained using submersibles, have outlined the thermal boundaries for microbial processes in Guaymas Basin sediments. At the hyperthermophilic end of the spectrum, the H₂/CO₂-dependent methanogen *Methanopyrus kandleri* survives at 110°C under atmospheric

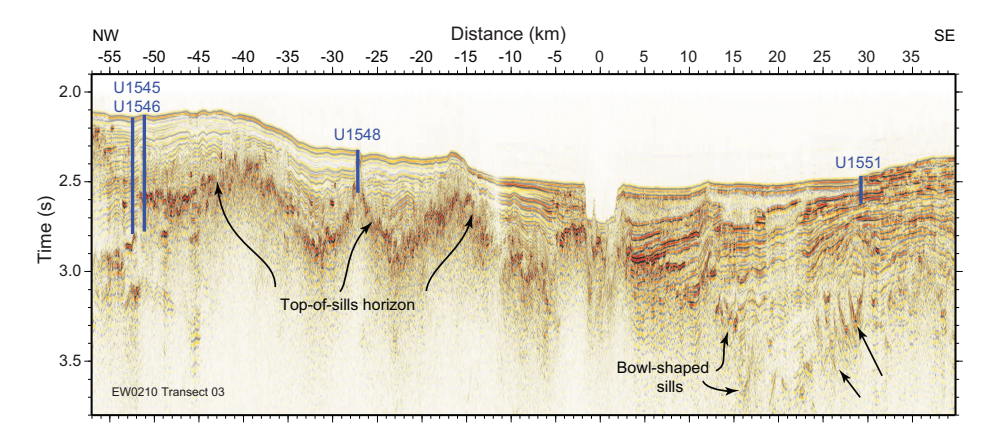


Figure F3. Migrated stack of seismic data from *Maurice Ewing* Cruise EW0210 Transect 3 (see Figure F1), along which Sites U1545, U1546, U1548, and U1551 are located. Blue line = maximum penetration depths.

pressure (Kurr et al., 1991) and at 122°C under deep-sea pressure (Takai et al., 2008). Sulfur-reducing Thermococcales thrive near 100°C (Teske et al., 2009; Edgcomb et al., 2007), and microbial sulfate reducers are active near 90°C (Elsgaard et al., 1994; Jørgensen et al., 1990; Weber and Jørgensen, 2002) and potentially near 120°C (Jørgensen et al., 1992). Hyperthermophiles commonly utilize hydrogen as an electron donor, which leads to selective hydrogen depletion in the hydrothermal subsurface (Wankel et al., 2011). Recently, anaerobic methane-oxidizing archaea that are active at temperatures as high as 75°C were identified in Guaymas Basin and at other vent sites (Holler et al., 2011; Biddle et al., 2012; Merkel et al., 2013; McKay et al., 2016). At cooler, off-axis locations and in the upper sediment column, less extreme microbiota gain a foothold, increasing overall microbial biomass and activity and broadening the chemical spectrum of microbially catalyzed reactions. For example, alkane-degrading syntrophic archaea and sulfate-reducing bacteria with a temperature preference of 50°-60°C thrive in Guaymas Basin sediments (Rueter et al., 1994; Kniemeyer et al., 2007; Laso-Pérez et al., 2016; Krukenberg et al., 2016); uncultured representatives are detectable with gene assays for anaerobic hydrocarbon degradation (Callaghan et al., 2010). Finally, surface sediments harbor microbial mats of sulfide-oxidizing filamentous bacteria at the seawater interface (Gundersen et al., 1992; McKay et al., 2012), along with mesophilic, aerobic aromatics degraders (Goetz and Jannasch, 1993; Gutierrez et al., 2015). In general, microbial communities in surficial sediments of Guaymas Basin overlap compositionally with those in seeps and cold subsurface sediments (Teske et al., 2002; Teske, 2006). Collectively, these diversified microbial communities are capable of assimilating fossil organic carbon into microbial biomass (Pearson et al., 2005). The habitat preference, biogeography, and activity patterns of these Guaymas Basin microorganisms remain to be investigated in the subsurface. We should also remain open to the possibility of finding new organisms that currently have no precedent. For example, metagenomic analyses of hydrothermal Guaymas Basin sediments have detected new lineages of the Asgardarchaeota (Dombrowski et al., 2018; Seitz et al., 2019), the archaeal superphylum that shares eukaryotic genes to an uncommon degree and is considered the closest living affiliate to ancestral eukaryotes.

3.2. Site surveys and seismic studies

Expedition 385 is supported by site survey data acquired on five ships during cruises led by chief scientists from three countries (US, Germany, and Mexico). The three seismic data sets were acquired during research vessel (R/V) Maurice Ewing Cruise EW0210 (2002), R/V Sonne Cruise SO-241 (2015), and R/V Alpha Helix Cruise AH1605 (2016). The Cruise EW0210 seismic data, acquired with a 6 km streamer (led by Chief Scientist Daniel Lizarralde, Woods Hole Oceanographic Institution, US), provided seismic-velocity control for time-to-depth estimations at all Expedition 385 sites. Ultimately, five of eight sites drilled during Expedition 385 were proposed based on features observed in the migrated stack of the transect (Figure F3). The seismic feature observed at Site U1548 motivated the hypothesis that active magmatism occurs at substantial distances from the plate boundary. From this, it follows that active, methane-hosted seafloor communities are expected to be present throughout Guaymas Basin, a hypothesis that was tested through a deep-tow multibeam survey conducted during R/V Atlantis Cruise AT15-54 in 2009. By means of deep-tow backscatter and compressed high-intensity radar pulse (CHIRP) subbottom images, seafloor photography, and water chemistry samples, this cruise identified multiple methanehosted seafloor communities at off-axis locations (Lizarralde et al., 2011). The observations from Cruise AT15-54 motivated several drill sites for which no seismic data were available. The second seismic survey was performed during Cruise SO-241 in 2015 (led by Chief Scientist Christian Berndt, GEOMAR Helmholtz Centre for Ocean Research Kiel, Germany). The transect of these high-quality data crossed some but not all of the proposed drill sites. The third seismic survey (led by Chief Scientist Antonio González-Fernández, Centro de Investigación Científica y de Educación Superior de Ensenada [CICESE], Mexico) acquired seismic crossing lines through all of the proposed drill sites during Cruise AH-1605.

Sites initially selected based on the Cruise EW0210 multichannel seismic profiles (Lizarralde et al., 2007) and the observations from Cruise AT15-54 (Lizarralde et al., 2011) were adjusted based on results from the new seismic lines and two additional site survey cruises by the R/V *El Puma* (7–27 October 2014) and *Atlantis* (9–27 December 2016). The 2014 *El Puma* cruise (led by Chief

Scientist Carlos Mortera, Universidad Nacional Autónoma de México [UNAM], Mexico) performed a detailed bathymetric survey of the central portion of the northern Guaymas Basin spreading segment and collected sediment piston cores 3-5 m in length from the northwestern side of the northern spreading segment, the Sonora margin, and the circular seep structure called Ringvent. These cores provided shallow subsurface sediments near several proposed Expedition 385 drill sites and enabled a preliminary geochemical and microbial characterization of the proposed off-axis drill sites (Teske et al., 2019; Ramírez et al., 2020). Numerous shallow sediment cores and seafloor grab samples were also collected during Sonne Cruise 241 (Núñez-Useche et al., 2018; Geilert et al., 2018). A major discovery from that cruise was a large, active hydrothermal vent field located on the southeastern edge of the northern Guaymas Basin graben (Berndt et al., 2016). The last site survey cruise on Atlantis studied the Ringvent sites (U1547 and U1548) with human occupied vehicle (HOV) Alvin Dives 4864 and 4865 and autonomous underwater vehicle (AUV) Sentry Dives 410 and 411 (led by Chief Scientist Andreas Teske, University of North Carolina at Chapel Hill, US) providing faunal observations, microbial analyses, thermal gradient measurements in surficial sediments, and mineralogic and pore water chemistry analyses that demonstrated this site is hydrothermally active (Teske et al., 2019). These results were used to further characterize the proposed Ringvent drill sites and to adjust their locations.

3.3. Scientific objectives

The following three primary scientific objectives were outlined in the Expedition 385 *Scientific Prospectus* (Teske et al., 2018):

- Quantify the sedimentary and elemental inputs to the basin through time and their variation with changing oceanographic and climatic conditions.
- Sample sill intrusions and the surrounding sediments to determine the products and efficiency of hydrothermal alteration and key hydrologic factors such as sediment type, faulting, and permeability evolution and how they impact the subsurface storage and flow of sedimentary carbon.
- Study subsurface microbial communities hosted by alteration products to determine their efficiency at capturing carbon-bearing alteration products and to further our understanding of the conditions that limit life in the deep biosphere.

The northwest–southeast transect of drill sites established during Expedition 385 represents all kinds of depositional settings in Guaymas Basin that have sills intruding the local sediment successions on and off axis at a wide range of depths (from <100 to >600 meters below seafloor [mbsf]). The comprehensive characterization of these sill-sediment packages in terms of the interacting physical, chemical, and microbial processes will enable us to decipher the fate of sedimentary carbon (sequestration versus release) in Guaymas Basin. From this study we will be able to draw conclusions for the entire Gulf of California and similar marginal seas on Earth.

4. Site summaries

4.1. Site U1545

4.1.1. Background and objectives

Site U1545 (proposed Site GUAYM-01B) is located \sim 52 km northwest of the axial graben of the northern Guaymas Basin spreading segment (Figure F1). The primary objective for this site is shared with Site U1546, located just 1.1 km away (Figure F4). The objective is to compare the sediments at two sites that are very close to each other but that, as seismic data suggest, have had very different degrees of alteration from intruding sills. Preexpedition seismic survey data indicate an undisturbed sedimentary succession at Site U1545 from the seafloor to \sim 2.8 s two-way traveltime (TWT) (\sim 540 mbsf), where an interpreted sill was observed. In contrast, seismic data show the same stratigraphic sequence at Site U1546 to be substantially disturbed between an apparent unconformity at \sim 2.3 s TWT and a bright reflector at \sim 2.6 s TWT (\sim 350 mbsf), which was interpreted to be a sill intrusion. Sills deeper than 2.6 s TWT were also interpreted at Site U1546. Com-

parison of Sites U1545 and U1546 thus enables the quantification of thermal and hydrothermal alteration driven by sill intrusion at Site U1546.

4.1.2. Operations

We cored three holes at Site U1545. Hole U1545A is located at 27°38.2325′N, 111°53.3406′W in a water depth of 1593.5 m. In Hole U1545A, we used the advanced piston corer (APC), half-length APC (HLAPC), and extended core barrel (XCB) systems to advance from the seafloor to a final depth of 503.3 mbsf with a recovery of 389.0 m (77%). We made formation temperature measurements at several depths using the advanced piston corer temperature (APCT-3) and Sediment Temperature 2 (SET2) tools. We terminated coring based on the safety monitoring protocol for hydrocarbon gases after measuring a low methane/ethane (C_1/C_2) value. We then conducted downhole measurements in Hole U1545A: (1) recovery of borehole fluid with the Kuster Flow Through Sampler (Kuster FTS) and (2) downhole logging with the triple combination (triple combo) and Formation MicroScanner (FMS)-sonic logging tool strings. In Hole U1545B, located at 27°38.2301′N, 111°53.3295′W in a water depth of 1594.2 m, we deployed the APC, HLAPC, and XCB systems. Cores penetrated from the seafloor to a final depth of 387.3 mbsf and recovered 340.1 m (88%). Formation temperature measurements were carried out at several depths with the APCT-3 and SET2 tools. In Hole U1545C, located at 27°38.2420'N, 111°53.3290'W in a water depth of 1595.0 m, we deployed the APC, HLAPC, and XCB systems to advance from the seafloor to a final depth of 329.0 mbsf with a recovery of 324.6 m (99%). Holes U1545B and U1545C were dedicated to extensive microbial and biogeochemical sampling that required the deployment of perfluorocarbon tracers (PFTs) downhole on all cores to monitor drilling fluid (seawater) contamination (House et al., 2003; Lever et al., 2006). During the first 2 days of coring in Hole U1545B, the pace of coring was adjusted to accommodate the complex microbial sampling program conducted on the core receiving platform. A total of 232.1 h, or 9.7 days, were spent at Site U1545. Cores, penetration depths, core recovery, and operations schedule for all holes of Site U1545 are listed in Table **T1**.

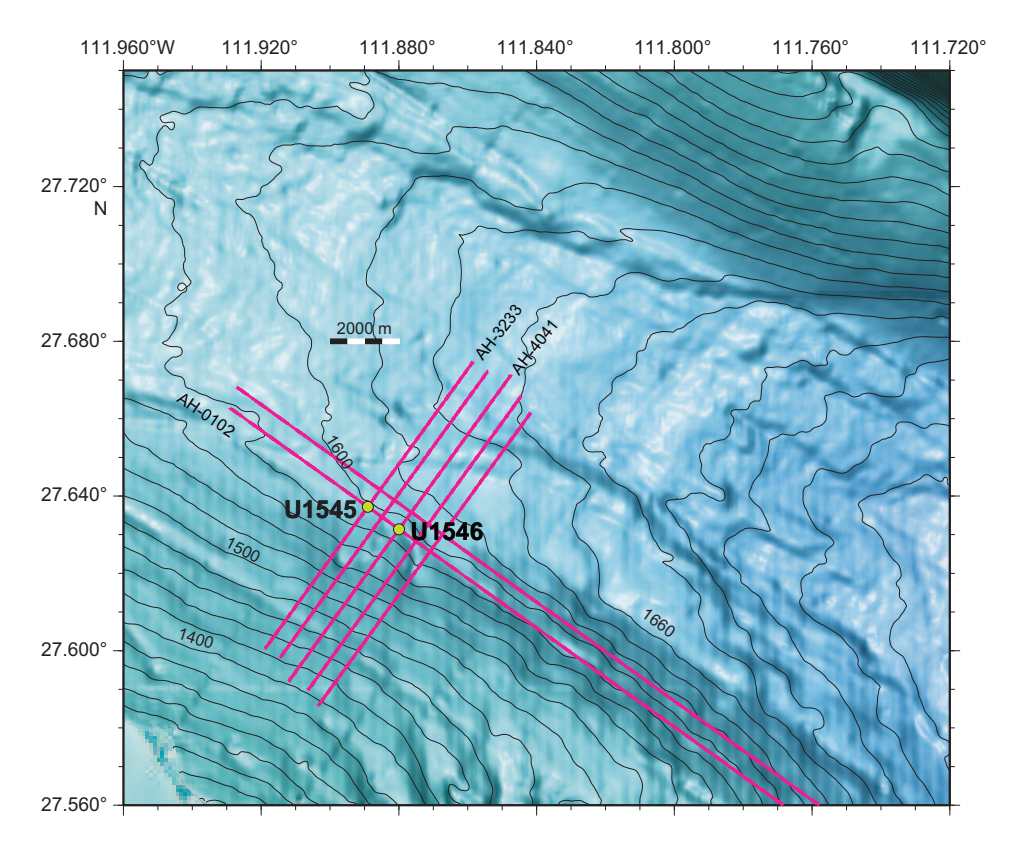


Figure F4. Bathymetric map, Sites U1545 and U1546. Seismic Lines AH-0102 and crossing Seismic Lines AH-0304 and AH-0506 are also shown. The locations of drilled holes at each site are not distinguishable at the given scale. Contour lines = 20 m.

4.1.3. Principal results

4.1.3.1. Lithostratigraphy

The deepest record of sediments and igneous rocks was recovered in Hole U1545A from a curated depth of 507.27 mbsf, whereas recovery reached 387.23 and 328.88 mbsf in Holes U1545B and U1545C, respectively. Site U1545 is composed of late to middle Pleistocene sediments that are primarily a mixture of laminated diatom ooze and clay minerals (Figure F5). Minor components encompass nannofossils and silt-sized siliciclastic particles and authigenic minerals. The latter include pyrite and clay- to silt-sized carbonate (micrite) particles (mainly dolomite) that occur both scattered in the sediment and concentrated in discrete nodules/concretions with different degrees of lithification. Downhole changes in lithology are not significant enough to require a division of the site into more than one lithostratigraphic unit (Unit I). However, the presence of minor yet significant downhole lithologic changes and/or changes in sediment induration and physical properties prompt the division of Unit I into four subunits (IA-ID). These differences arise mainly from different degrees and types of diagenetic processes and overprinting that have resulted in the formation of authigenic minerals (e.g., micrite in Subunit IB) and/or the selective dissolution of sedimentary particles (e.g., dissolution of diatoms during opal-A to opal-CT phase transformation in Subunits IC and ID). The transitions between subunits are gradual, occur over more than one core, and may be locally obscured in low-recovery zones. The mixed biogenic and siliciclastic nature of the sediments and the abundance of fine lamination in the sedimentary record suggest that the depositional environment at Site U1545 has remained essentially hemipelagic and suboxic

Table T1. Expedition 385 operations summary. mbsl = meters below sea level, APC = advanced piston corer, HLAPC = half-length advanced piston corer, XCB = extended core barrel, RCB = rotary core barrel, UTC = Coordinated Universal Time. (Continued on next page.) **Download table in CSV format.**

U1545A 2738.2325'N 111"53.3406'W 1593.52 503.3 0.0 503.3 389.0 77.3 74 17 31 26 0 0 0 0 0 0 0 0 0	Hole	Latitude	Longitude	Water depth (mbsl)	Total penetration (m)	Drilled interval (m)	Cored interval (m)	Core recovered (m)	Recovery (%)	Total cores (N)	APC cores (N)	HLAPC cores (N)	XCB cores (N)	RCB cores (N)
U1545C V738_2420'N 111"53.3290 N 594.96 329.0 0.0 329.0 324.6 98.7 63 16 42 5 0	U1545A	27°38.2325′N	111°53.3406′W	1593.52	503.3	0.0	503.3	389.0	77.3	74	17	31	26	0
Sire U1545 totals	U1545B	27°38.2301′N	111°53.3295′W	1594.24	387.3	0.0	387.3	340.1	87.8	67	17	40	10	0
U1546A ZP*37.8851'N U11*52.7939'W 1586.10 361.2 0.0 361.2 365.7 101.3 64 21 25 18 0 U1546B ZP*37.8840'N U11*52.7869'W 1585.58 333.8 0.0 333.8 351.2 105.2 59 22 21 16 0 U1546C ZP*37.8943'N U11*52.7568'W 1585.56 540.2 308.2 232.0 139.7 60.2 41 0 0 0 41 U1546D ZP*37.8943'N U11*52.7568'W 1585.59 300.1 0.0 300.1 31.4 704.9 47 27 714 6 0 U1547A ZP*30.4561'N U11*40.6980'W U1547B 200.8 0.0 200.1 117.3 105.9 27 11 8 8 0 U1547B ZP*30.4128'N U11*40.7064'W U1547B 200.8 0.0 200.8 161.3 76.9 50 10 14 26 0 U1547C ZP*30.4551'N U11*40.7064'W U1542.2 159.2 81.3 77.9 9.0 U15.3 8 0 0 0 0 0 U1547C ZP*30.3598'N U11*40.7483'W U1542.9 U1547B U15	U1545C	27°38.2420′N	111°53.3290′W	1594.96	329.0	0.0	329.0	324.6	98.7	63	16	42	5	0
U1546B Z°737.8840'N U11"52.7809'W 1585.58 333.8 30.0 333.8 351.2 105.2 59 22 21 16 0 0 0 0 0 0 0 0 0			Site I	J1545 totals:	1219.6	0.0	1219.6	1053.7	86.4	204	50	113	41	0
U1546C 27°37.8724′N U11°52.7568′W 1585.96 540.2 308.2 232.0 139.7 60.2 41 0 0 0 0 41	U1546A	27°37.8851′N	111°52.7939′W	1586.10	361.2	0.0	361.2	365.7	101.3	64			18	0
$ \begin{array}{c c c c c c c c c c c c c c c c c c c $	U1546B	27°37.8840′N	111°52.7809′W	1585.58	333.8	0.0	333.8	351.2	105.2	59	22	21	16	0
Site U1546 totals: 1535.3 308.2 1227.1 1171.3 95.5 211 70 60 40 41	U1546C	27°37.8724′N	111°52.7568′W	1585.56	540.2	308.2	232.0	139.7	60.2	41	0	0	0	41
U1547A 27°30.4561'N 111°40.6980'W 1733.72 141.3 0.0 141.3 145.3 102.9 27 11 8 8 0 0 0 0 0 0 0 0	U1546D	27°37.8943′N	111°52.7812′W	1585.92	300.1	0.0	300.1	314.7	104.9	47	27	14	6	0
U1547B 27°30.4128'N 111°40.7341'W 1732.22 209.8 0.0 209.8 161.3 76.9 50 10 14 26 0 U1547C 27°30.34455'N 111°40.7064'W 1732.22 159.2 81.3 77.9 9.0 11.5 8 0 0 0 8 U1547D 27°30.3947'N 111°40.7483'W 1732.22 193.0 81.3 111.7 34.9 31.3 20 0 0 0 20 U1547E 27°30.3598'N 111°40.756'W 1732.09 191.2 61.8 129.4 44.9 34.7 23 0 0 0 0 23 U1548A 27°30.2546'N 111°40.8665'W 1739.94 103.4 0.0 103.4 114.0 110.2 20 14 0 6 0 U1548B 27°30.2546'N 111°40.8665'W 1738.94 95.1 0.0 95.1 87.7 92.2 12 9 0 3 0 U1548B 27°30.2546'N 111°40.8476'W 1737.03 69.8 0.0 69.8 71.0 101.7 10 7 0 3 0 U1548D 27°30.5316'N 111°41.3855'W 1729.33 110.0 0.0 110.0 120.5 109.6 13 12 1 0 0 U1548C 27°30.4829'N 111°40.844'W 1840.07 168.0 0.0 48.3 508.5 104.1 67 54 1 12 0 U1549B 27°28.3387'N 111°28.7927'W 1841.17 166.9 0.0 168.0 166.9 164.4 98.5 18 18 0 0 0 U1550B 27°15.1602'N 111°30.4163'W 2000.81 207.0 0.0 27.0 190.9 92.2 32 12 7 13 0 U1551B 27°12.3887'N 111°30.4451'W 1843.90 48.5 0.0 48.5 50.0 103.1 6 6 0 0 0 U1551B 27°12.3887'N 111°31.841'W 1843.90 48.5 0.0 48.5 50.0 103.1 6 6 0 0 0 U1552C 27°33.2885'N 111°32.9665'W 1841.59 107.5 0.0 168.8 172.1 102.0 25 21 4 0 0 U1552C 27°33.2885'N 111°32.9665'W 1841.59 50.0 55.0 40.0 72.6 6 6 0 0 0 U1552C 27°33.2885'N 111°32.9665'W 1841.59 50.0 0.0 55.0 40.0 72.6 6 6 0 0 0 U1552C 27°33.2885'N 111°32.9665'W 1841.99 55.0 0.0 55.0 40.0 72.6 6 6 0 0 0 U1552C 27°33.2885'N 111°32.8557'W 1841.99 55.0 0.0 55.0 40.0 72.6 6 6 0 0 0 U1552C 27°33.2181'N 111°32.8557'W 1841.99 55.0 0.0 261.8 192.2 73.4 29 99 0 0 0	-				1535.3	308.2	1227.1	1171.3	95.5	211	70	60	40	41
U1547C 27°30.4455′N 111°40.7064′W 1732.22 159.2 81.3 77.9 9.0 11.5 8 0 0 0 0 20	U1547A	27°30.4561′N	111°40.6980′W	1733.72	141.3	0.0	141.3	145.3	102.9	27	11	8	8	0
U1547D 27°30,3947'N 111°40,7483'W 1732.22 193.0 81.3 111.7 34.9 31.3 20 0 0 0 0 20	U1547B	27°30.4128′N	111°40.7341′W	1732.22	209.8	0.0	209.8	161.3	76.9	50	10	14	26	0
U1547E 27°30.3598′N 111°40.7756′W 1732.09 191.2 61.8 129.4 44.9 34.7 23 0 0 0 0 23	U1547C	27°30.4455′N	111°40.7064′W	1732.22	159.2	81.3	77.9	9.0	11.5	8	0	0	0	8
Site U1547 totals:	U1547D	27°30.3947′N	111°40.7483′W	1732.22	193.0	81.3	111.7	34.9	31.3	20	0	0	0	20
U1548A 27°30.2466′N 111°40.8665′W 1739.94 103.4 0.0 103.4 114.0 110.2 20 14 0 6 0 0 U1548B 27°30.2540′N 111°40.8601′W 1738.94 95.1 0.0 95.1 87.7 92.2 12 9 0 3 0 0 0 U1548C 27°30.2698′N 111°40.8476′W 1737.03 69.8 0.0 69.8 71.0 101.7 10 7 0 3 0 0 U1548D 27°30.5316′N 111°41.3855′W 1729.33 110.0 0.0 110.0 120.5 109.6 13 12 1 0 0 0 U1548E 27°30.4829′N 111°41.2922′W 1729.93 110.0 0.0 110.0 115.2 104.8 12 12 0 0 0 0 0 0 0 0 0 0 0 0 0 0 0 0 0	U1547E	27°30.3598′N	111°40.7756′W	1732.09	191.2	61.8	129.4	44.9	34.7	23	0	0	0	23
U1548B 27°30.2540′N 111°40.8601′W 1738.94 95.1 0.0 95.1 87.7 92.2 12 9 0 3 0			Site l	J1547 totals:	894.5	224.4	670.1	395.4	59.0	128	21	22	34	51
U1548C Z7°30.2698'N 111°40.8476'W 1737.03 69.8 0.0 69.8 71.0 101.7 10 7 0 3 0	U1548A	27°30.2466′N	111°40.8665′W	1739.94	103.4	0.0	103.4	114.0	110.2	20	14	0	6	0
U1548D 27°30.5316′N 111°41.3855′W 1729.33 110.0 0.0 110.0 120.5 109.6 13 12 1 0 0 0 0 0 0 0 0 0	U1548B	27°30.2540′N	111°40.8601′W	1738.94	95.1	0.0	95.1	87.7	92.2	12	9	0	3	0
U1548E 27°30.4829′N 111°41.2922′W 1729.93 110.0 0.0 110.0 115.2 104.8 12 12 0 0 0 0	U1548C	27°30.2698′N	111°40.8476′W	1737.03	69.8	0.0	69.8	71.0	101.7	10	7	0	3	0
Site U1548 totals: 488.3 0.0 488.3 508.5 104.1 67 54 1 12 0 U1549A 27°28.3317′N 111°28.7844′W 1840.07 168.0 0.0 168.0 166.9 99.3 18 18 0 0 0 0 U1549B 27°28.3383′N 111°28.7927′W 1841.17 166.9 0.0 166.9 164.4 98.5 18 18 0 0 0 0 U1550A 27°15.1602′N 111°30.4163′W 2000.81 207.0 0.0 207.0 190.9 92.2 32 12 7 13 0 U1550B 27°15.1704′N 111°30.4451′W 2001.21 174.2 0.0 174.2 160.8 92.3 23 12 5 6 0 U1551A 27°12.3887′N 111°13.1943′W 1844.11 120.3 0.0 120.3 122.1 101.5 19 15 4 0 0 U1551B 27°12.3832′N 111°13.1841′W 1843.90 48.5 0.0 48.5 50.0 103.1 6 6 0 0 0 U1552A 27°33.2906′N 111°32.9665′W 1841.59 107.5 0.0 107.5 73.9 68.7 12 12 0 0 0 U1552C 27°33.2181′N 111°32.8557′W 1844.29 99.3 0.0 99.3 78.3 78.8 11 11 0 0 0 0 Site U1552 totals: 261.8 0.0 261.8 192.2 73.4 29 29 0 0 0	U1548D	27°30.5316′N	111°41.3855′W	1729.33	110.0	0.0	110.0	120.5	109.6	13	12	1	0	0
U1549A 27°28.3317'N 111°28.7844'W 1840.07 168.0 0.0 168.0 166.9 99.3 18 18 0 0 0 0 0 15498 27°28.3383'N 111°28.7927'W 1841.17 166.9 0.0 166.9 164.4 98.5 18 18 0 0 0 0 0 0 0 0 0 0 0 0 0 0 0 0 0	U1548E	27°30.4829′N	111°41.2922′W	1729.93	110.0	0.0	110.0	115.2	104.8	12	12	0	0	0
U1549B 27°28.3383′N 111°28.7927′W 1841.17 166.9 0.0 166.9 164.4 98.5 18 18 0 0 0 0 0 0 0 0 0 0 0 0 0 0 0 0 0			Site l	488.3	0.0	488.3	508.5	104.1	67	54	1	12	0	
Site U1549 totals: 334.9 0.0 334.9 331.3 98.9 36 36 0 0 0 0 0 U1550A 27°15.1602′N 111°30.4163′W 2000.81 207.0 0.0 207.0 190.9 92.2 32 12 7 13 0 U1550B 27°15.1704′N 111°30.4451′W 2001.21 174.2 0.0 174.2 160.8 92.3 23 12 5 6 0 0 Site U1550 totals: 381.2 0.0 381.2 351.7 92.3 55 24 12 19 0 U1551A 27°12.3887′N 111°13.1943′W 1844.11 120.3 0.0 120.3 122.1 101.5 19 15 4 0 0 U1551B 27°12.3832′N 111°13.1841′W 1843.90 48.5 0.0 48.5 50.0 103.1 6 6 0 0 0 0 Site U1551 totals: 168.8 0.0 168.8 172.1 102.0 25 21 4 0 0 U1552A 27°33.2906′N 111°32.9665′W 1841.59 107.5 0.0 107.5 73.9 68.7 12 12 0 0 0 U1552B 27°33.2885′N 111°32.9640′W 1841.09 55.0 0.0 55.0 40.0 72.6 6 6 6 0 0 0 0 U1552B 27°33.2181′N 111°32.8557′W 1844.29 99.3 0.0 99.3 78.3 78.8 11 11 0 0 0 0 0 Site U1552 totals: 261.8 0.0 261.8 192.2 73.4 29 29 0 0 0	U1549A	27°28.3317′N	111°28.7844′W	1840.07	168.0	0.0	168.0	166.9	99.3	18	18	0	0	0
U1550A 27°15.1602′N 111°30.4163′W 2000.81 207.0 0.0 207.0 190.9 92.2 32 12 7 13 0 U1550B 27°15.1704′N 111°30.4451′W 2001.21 174.2 0.0 174.2 160.8 92.3 23 12 5 6 0 Site U1550 totals: 381.2 0.0 381.2 351.7 92.3 55 24 12 19 0 U1551A 27°12.3887′N 111°13.1943′W 1844.11 120.3 0.0 120.3 122.1 101.5 19 15 4 0 0 U1551B 27°12.3832′N 111°13.1841′W 1843.90 48.5 0.0 48.5 50.0 103.1 6 6 0 0 0 Site U1551 totals: 168.8 0.0 168.8 172.1 102.0 25 21 4 0 0 U1552A 27°33.2906′N 111°32.9665′W 1841.59 107.5 0.0 107.5 73.9 68.7 12 12 0 0 0 U1552B 27°33.2885′N 111°32.9640′W 1841.09 55.0 0.0 55.0 40.0 72.6 6 6 6 0 0 0 U1552C 27°33.2181′N 111°32.8557′W 1844.29 99.3 0.0 99.3 78.3 78.8 11 11 0 0 0 0 Site U1552 totals: 261.8 0.0 261.8 192.2 73.4 29 29 0 0 0	U1549B	27°28.3383′N	111°28.7927′W	1841.17	166.9	0.0	166.9	164.4	98.5	18	18	0	0	0
U1550B 27°15.1704′N 111°30.4451′W 2001.21 174.2 0.0 174.2 160.8 92.3 23 12 5 6 0 Site U1550 totals: 381.2 0.0 381.2 351.7 92.3 55 24 12 19 0 U1551A 27°12.3887′N 111°13.1943′W 1844.11 120.3 0.0 120.3 122.1 101.5 19 15 4 0 0 U1551B 27°12.3832′N 111°13.1841′W 1843.90 48.5 0.0 48.5 50.0 103.1 6 6 0 0 0 0 Site U1551 totals: 168.8 0.0 168.8 172.1 102.0 25 21 4 0 0 U1552A 27°33.2906′N 111°32.9665′W 1841.59 107.5 0.0 107.5 73.9 68.7 12 12 0 0 0 0 U1552B 27°33.2885′N 111°32.9640′W 1841.09 55.0 0.0 55.0 40.0 72.6 6 6 6 0 0 0 U1552C 27°33.2181′N 111°32.8557′W 1844.29 99.3 0.0 99.3 78.3 78.8 11 11 0 0 0 0 Site U1552 totals: 261.8 0.0 261.8 192.2 73.4 29 29 0 0 0			Site l	J1549 totals:	334.9	0.0	334.9	331.3	98.9	36	36	0	0	0
Site U1550 totals: 381.2 0.0 381.2 351.7 92.3 55 24 12 19 0 U1551A 27°12.3887'N 111°13.1943'W 1844.11 120.3 0.0 120.3 122.1 101.5 19 15 4 0 0 U1551B 27°12.3832'N 111°13.1841'W 1843.90 48.5 0.0 48.5 50.0 103.1 6 6 6 0 0 0 Site U1551 totals: 168.8 0.0 168.8 172.1 102.0 25 21 4 0 0 U1552A 27°33.2906'N 111°32.9665'W 1841.59 107.5 0.0 107.5 73.9 68.7 12 12 0 0 0 U1552B 27°33.2885'N 111°32.9640'W 1841.09 55.0 0.0 55.0 40.0 72.6 6 6 0 0 0 U1552C 27°33.2181'N 111°32.8557'W 1844.29 99.3 0.0 99.3 78.3 78.8 11 11 0 0 0 Site U1552 totals: 261.8 0.0 261.8 192.2 73.4 29 29 0 0 0	U1550A	27°15.1602′N	111°30.4163′W	2000.81	207.0	0.0	207.0	190.9	92.2	32	12	7	13	0
U1551A 27°12.3887'N 111°13.1943'W 1844.11 120.3 0.0 120.3 122.1 101.5 19 15 4 0 0 U1551B 27°12.3832'N 111°13.1841'W 1843.90 48.5 0.0 48.5 50.0 103.1 6 6 0 0 0 Site U1551 totals: 168.8 0.0 168.8 172.1 102.0 25 21 4 0 0 U1552A 27°33.2906'N 111°32.9665'W 1841.59 107.5 0.0 107.5 73.9 68.7 12 12 0 0 0 U1552B 27°33.2885'N 111°32.9640'W 1841.09 55.0 0.0 55.0 40.0 72.6 6 6 0 0 0 0 U1552C 27°33.2181'N 111°32.855'W 1844.29 99.3 0.0 99.3 78.3 78.8 11 11 0 0 0 Site U1552 totals: 261.8 0.0 261.8 192.2 73.4 29 29 0 0 0	U1550B	27°15.1704′N	111°30.4451′W	2001.21	174.2	0.0	174.2	160.8	92.3	23	12	5	6	0
U1551B 27°12.3832′N 111°13.1841′W 1843.90 48.5 0.0 48.5 50.0 103.1 6 6 0 0 0 0 0 0 0 0 0 0 0 0 0 0 0 0 0			Site I	J1550 totals:	381.2	0.0	381.2	351.7	92.3	55	24	12	19	0
Site U1551 totals: 168.8 0.0 168.8 172.1 102.0 25 21 4 0 0 U1552A 27°33.2906′N 111°32.9665′W 1841.59 107.5 0.0 107.5 73.9 68.7 12 12 0 0 0 0 U1552B 27°33.2885′N 111°32.9640′W 1841.09 55.0 0.0 55.0 40.0 72.6 6 6 6 0 0 0 U1552C 27°33.2181′N 111°32.8557′W 1844.29 99.3 0.0 99.3 78.3 78.8 11 11 0 0 0 0 Site U1552 totals: 261.8 0.0 261.8 192.2 73.4 29 29 0 0 0	U1551A	27°12.3887′N	111°13.1943′W	1844.11		0.0	120.3	122.1	101.5	19	15	4	0	0
U1552A 27°33.2906′N 111°32.9665′W 1841.59 107.5 0.0 107.5 73.9 68.7 12 12 0 0 0 0 U1552B 27°33.2885′N 111°32.9640′W 1841.09 55.0 0.0 55.0 40.0 72.6 6 6 0 0 0 0 U1552C 27°33.2181′N 111°32.8557′W 1844.29 99.3 0.0 99.3 78.3 78.8 11 11 0 0 0 0 0 Site U1552 totals: 261.8 0.0 261.8 192.2 73.4 29 29 0 0 0 0	U1551B	27°12.3832′N	111°13.1841′W	1843.90	48.5	0.0	48.5	50.0	103.1	6		0	0	0
U1552B 27°33.2885′N 111°32.9640′W 1841.09 55.0 0.0 55.0 40.0 72.6 6 6 0 0 0 0 U1552C 27°33.2181′N 111°32.8557′W 1844.29 99.3 0.0 99.3 78.3 78.8 11 11 0 0 0 0 0 Site U1552 totals: 261.8 0.0 261.8 192.2 73.4 29 29 0 0 0			Site I	J1551 totals:	168.8	0.0	168.8	172.1	102.0	25	21	4	0	0
U1552C 27°33.2181′N 111°32.8557′W 1844.29 99.3 0.0 99.3 78.3 78.8 11 11 0 0 0 0 0 Site U1552 totals: 261.8 0.0 261.8 192.2 73.4 29 29 0 0 0		27°33.2906′N	111°32.9665′W	1841.59		0.0	107.5	73.9	68.7	12	12	0	0	0
Site U1552 totals: 261.8 0.0 261.8 192.2 73.4 29 29 0 0 0	U1552B	27°33.2885′N	111°32.9640′W	1841.09	55.0	0.0	55.0	40.0	72.6	6	6	0	0	0
	U1552C	27°33.2181′N	111°32.8557′W	1844.29	99.3	0.0	99.3	78.3	78.8	11	11	0	0	0
Expedition 385 totals: 5284.4 532.6 4751.8 4176.2 87.9 755 305 212 146 92			Site I	J1552 totals:	261.8	0.0	261.8	192.2	73.4					
			Expedition	on 385 totals:	5284.4	532.6	4751.8	4176.2	87.9	755	305	212	146	92

to anoxic throughout the middle to late Pleistocene. Igneous rocks of subvolcanic texture and basaltic composition were encountered as an intrusive sheet in the sedimentary section near the bottom of Hole U1545A.

4.1.3.2. Igneous petrology and alteration

In Hole U1545A, we penetrated a mafic sill intrusion hosted by siliceous claystone and recovered a total core length of 86 cm from a top depth of 482.17 mbsf. This thin hypabyssal rock layer is identified as part of Subunit ID. It is dominantly composed of aphyric basalt. A ~3 cm thick baked layer of carbonate metasedimentary rock forms the upper contact with the sill. The dark gray aphyric basalt has an aphanitic texture with a micro to cryptocrystalline inequigranular igneous mineral assemblage consisting of plagioclase, pyroxene, and accessory Fe-Ti oxides. Moderate to sparse vesicularity overall decreases with depth. Plagioclase phenocrysts are rarely present (<1 vol%). The entire cored length of the basaltic rock layer is texturally and mineralogically homogeneous except for a 1 cm thick, carbonate-rich vesicular interval in the middle of the section that has an overall coarser grain size and no microphenocrysts. The entire recovered section shows moderate alteration that is consistent with hydrothermal fluid-rock interaction. Plagioclase grains are slightly altered to sericite, whereas pyroxenes remain only as pseudomorphs that are totally replaced by secondary magnetite and clay minerals. Vesicles are mostly filled with secondary minerals. These precipitates are dominantly carbonates (e.g., calcite and dolomite) and clay minerals (e.g., smectite) with minor magnetite and pyrite. Observed veins are predominantly filled with carbonates, pyrite, and zeolites, giving them a white color with black and golden patches.

Table T1 (continued).

Hole	Start date	Start time UTC (h)	End date	End time UTC (h)	Time on hole (h)	Time on site (days)	Comment
U1545A	26 Sep 2019	2045	1 Oct 2019	0925	108.7	4.53	
U1545B	1 Oct 2019	0925	4 Oct 2019	1645	79.4	3.31	
U1545C	30 Oct 2019	0730	1 Nov 2019	0325	43.9	1.83	
Site U1545 totals:	26 Sep 2019	2045	1 Nov 2019	0325	232.1	9.67	26 days between operations in Holes U1545B and U1545C
U1546A	4 Oct 2019	1745	7 Oct 2019	0620	60.5	2.52	
U1546B	7 Oct 2019	0620	9 Oct 2019	1315	55.0	2.29	
U1546C	10 Oct 2019	0115	15 Oct 2019	0122	120.0	5.00	
U1546D	1 Nov 2019	0325	2 Nov 2019	1445	35.3	1.47	
Site U1546 totals:	4 Oct 2019	1745	2 Nov 2019	1445	270.7	11.3	17 days between operations in Holes U1546C and U1546D
U1547A	15 Oct 2019	0530	16 Oct 2019	2125	41.8	1.74	
U1547B	16 Oct 2019	2125	20 Oct 2019	0500	79.7	3.32	
U1547C	22 Oct 2019	0300	23 Oct 2019	0230	23.5	0.98	
U1547D	23 Oct 2019	0230	24 Oct 2019	2215	43.7	1.82	
U1547E	4 Nov 2019	0830	6 Nov 2019	0645	46.3	1.93	
Site U1547 totals:	15 Oct 2019	0530	6 Nov 2019	0645	235.0	9.79	11 days between operations in Holes U1547D and U1547E
U1548A	20 Oct 2019	0700	21 Oct 2019	0440	21.7	0.90	
U1548B	21 Oct 2019	0440	22 Oct 2019	0300	22.3	0.93	
U1548C	6 Nov 2019	2245	8 Nov 2019	0010	25.4	1.06	
U1548D	8 Nov 2019	0010	8 Nov 2019	1250	12.7	0.53	
U1548E	8 Nov 2019	1250	9 Nov 2019	0115	12.5	0.52	
Site U1548 totals:	20 Oct 2019	0700	9 Nov 2019	0115	94.6	3.94	15 days between operations in Holes U1548B and U1548C
U1549A	25 Oct 2019	0030	25 Oct 2019	2215	21.8	0.91	
U1549B	25 Oct 2019	2215	27 Oct 2019	0330	29.3	1.22	
Site U1549 totals:	25 Oct 2019	0030	27 Oct 2019	0330	51.1	2.13	
U1550A	27 Oct 2019	0530	28 Oct 2019	2020	38.8	1.62	
U1550B	28 Oct 2019	2020	30 Oct 2019	0530	33.2	1.38	
Site U1550 totals:	27 Oct 2019	0530	30 Oct 2019	0530	72.0	3.00	
U1551A	2 Nov 2019	1915	3 Nov 2019	1830	23.3	0.97	
U1551B	3 Nov 2019	1830	4 Nov 2019	0530	11.0	0.46	
Site U1551 totals:	2 Nov 2019	1915	4 Nov 2019	0530	34.3	1.43	
U1552A	9 Nov 2019	1000	9 Nov 2019	2345	13.7	0.57	
U1552B	9 Nov 2019	2345	10 Nov 2019	0400	4.3	0.18	
U1552C	10 Nov 2019	0400	10 Nov 2019	1845	14.6	0.61	
Site U1552 totals:	9 Nov 2019	1000	10 Nov 2019	1845	32.6	1.36	
Expedition 385 totals:	26 Sep 2019	2045	10 Nov 2019	1845	1022.4	42.6	

4.1.3.3. Structural geology

Tilted sedimentary beds and deformation structures are found in some depth intervals in Lithostratigraphic Subunits IA–ID. The folds and tilted beds observed in two depth intervals above 109 mbsf are attributed to two slump events that caused soft-sediment deformation. At greater depth, some preexisting brittle fractures are found. Some of the layers in Subunit IC exhibit fractures with

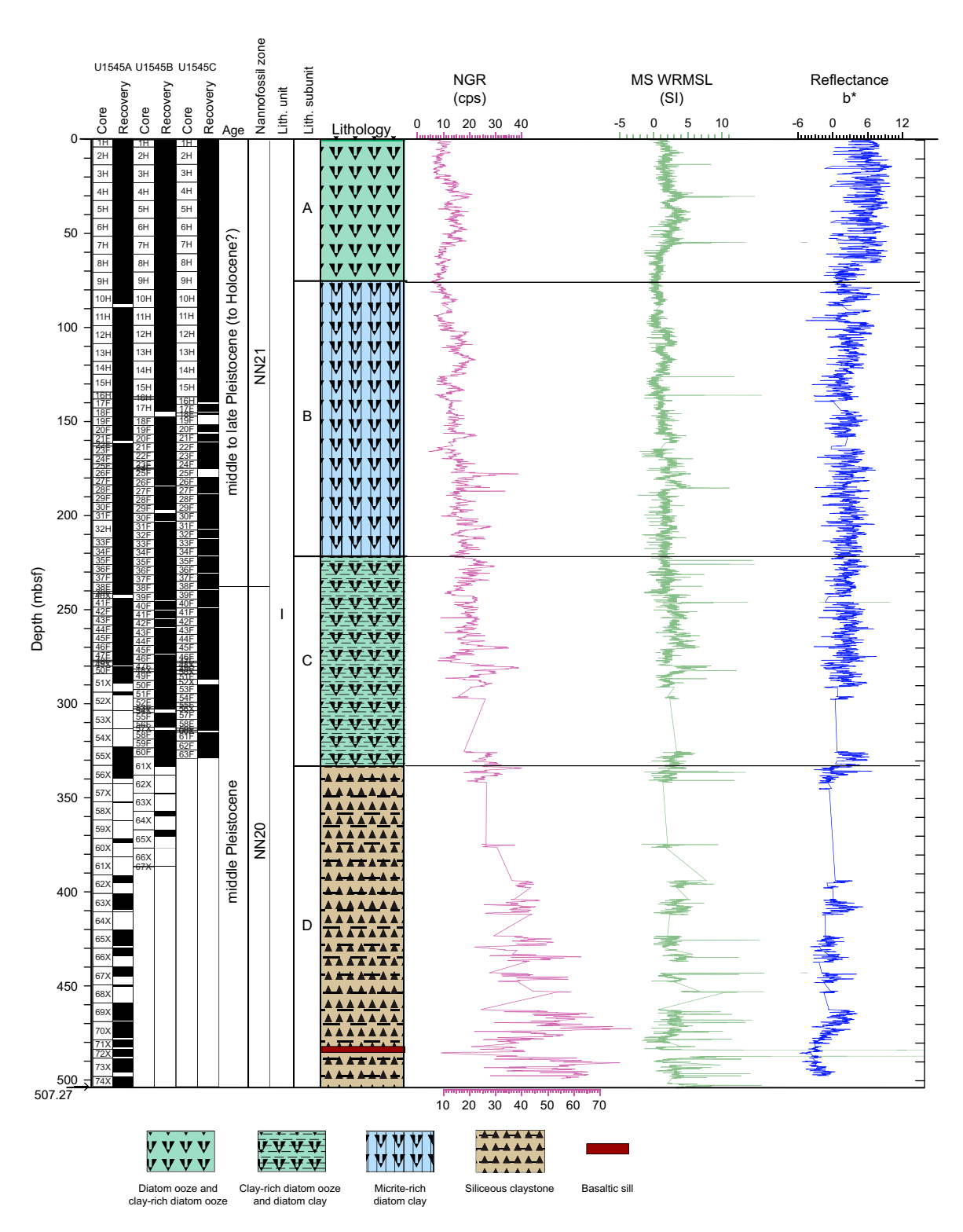


Figure F5. Lithostratigraphic column, Site U1545. NGR = natural gamma radiation, cps = counts per second, MS = magnetic susceptibility, WRMSL = Whole-Round Multisensor Logger. All data on display obtained from Hole U1545A, including the lithostratigraphic information.

apparent dips of 60° relative to the core axis. The mafic sill (Subunit ID) has mineralized fractures that are subvertical in orientation.

4.1.3.4. Biostratigraphy

At Site U1545, preservation of calcareous nannofossils is good/moderate to poor throughout the entire sedimentary sequence. In general, preservation is good/moderate in samples with abundant or common nannofossils and poor in those with frequent or rare nannofossils. Preservation is better in samples taken from intervals above the core catcher than in core catcher samples. Overall, marine diatoms were observed to be dominant/abundant with good/moderate preservation to ~300 mbsf and barren to the bottom of Holes U1545A and U1545B as a result of silica diagenesis. One biostratigraphic datum was recognized, and two additional stratigraphically underlying datums were estimated based on the absence of the zonal markers in the generally continuous succession from the late to middle Pleistocene. The lowermost occurrence (i.e., first occurrence datum) of *Emiliania huxleyi* dates the upper part of the sediment sequence to (Holocene–)late–middle Pleistocene (younger than 0.29 Ma; Hole U1545A = 0–248.6 mbsf; Hole U1545B = 0–249.6 mbsf), whereas the absence of *Pseudoemiliania lacunosa* (calcareous nannofossil) and *Fragilariopsis reinholdii* (marine diatom) in samples examined from the underlying interval indicates a middle Pleistocene age (younger than 0.44 Ma) for the bottom of both holes. Hole U1545C was not sampled. The estimated average sedimentation rate is 863 m/My (86.3 cm/ky).

4.1.3.5. Paleomagnetism

Alternating field (AF) demagnetization up to 20 mT was conducted with the superconducting rock magnetometer (SRM) on all archive-half sections from Hole U1545A. The drilling-induced overprint was successfully removed from APC and HLAPC cores (from the seafloor to ~280 mbsf) upon demagnetization. Inclination values after demagnetization at 20 mT cluster around 46°, which is similar to the expected geocentric axial dipole (GAD) inclination at the latitude of the site (46.3°). This is supported by a detailed analysis of the remanence of discrete samples. The drillinginduced overprint is removed by 10 mT, and the characteristic remanent magnetization (ChRM) is consistent with the SRM measurements. Unfortunately, XCB cores were overprinted and too disturbed to yield reliable paleomagnetic data, and no discrete samples could be collected. Cores 385-U1545A-1H through 50F (to ~280 mbsf) were assigned to the normal Brunhes Chron C1n (younger than 0.78 Ma). The natural remanent magnetization (NRM) of archive-half sections decreases from ~50 to 80 mbsf in a depth interval that corresponds to the sulfate-methane transition zone (SMTZ). The magnetic mineral assemblage becomes coarser, and low-coercivity minerals, likely (titano)magnetite, are dominant. In addition, AF demagnetization up to 20 mT was carried out on archive-half sections from Hole U1545B (Cores 46F-60F) to increase the depth interval of paleomagnetic measurements on HLAPC cores. This enabled us to make a tentative correlation between Holes U1545A and U1545B based on the NRM and point magnetic susceptibility that gives a possible offset of about 3 m between holes. Anisotropy of magnetic susceptibility (AMS) shows a mixture of prolate and oblate behavior in the sediments. No paleomagnetic measurements were carried out in Hole U1545C.

4.1.3.6. Inorganic geochemistry

A total of 80 interstitial water (IW) samples were collected from the sedimentary successions in Holes U1545A–U1545C. Sulfate concentration decreases to almost zero and methane concentration sharply increases around 50 mbsf at the SMTZ. Biogeochemical processes from the seafloor to 50 mbsf, including organoclastic sulfate reduction and anaerobic oxidation of methane, led to the accumulation of by-products such as sulfide, ammonium, and phosphate; a corresponding sharp increase in alkalinity; and a continuous increase in bromide. The downward increase in ammonium concentration to a maximum of >30 mM around 250 mbsf indicates ongoing microbial remineralization of organic matter. The significant decrease in calcium concentration toward the top of Subunit IB near 70–80 mbsf may correspond to the precipitation of authigenic carbonates. The drop in alkalinity and magnesium at ~70–80 mbsf could indicate the precipitation of authigenic dolomite, whereas the increase in calcium concentration could reflect the dissolution of carbonate phases other than dolomite. Chloride, silica, strontium, lithium, boron, and barium contents also continuously increase as a result of the dissolution of minerals such as silicates. Calcium, silica, strontium, lithium, boron, and barium concentrations continuously increase between 220 and 320 mbsf. The maximum concentration of dissolved silica is seen at ~290 mbsf, below

which depth the profile starts to reverse. Around the same depth, bromide, lithium, boron, strontium, barium, and sodium sharply increase and potassium sharply decreases. Below ~ 320 mbsf, a number of significant variations (increase or decrease) are observed for many dissolved elements (K⁺, B, Sr²⁺, Li⁺, etc.) and are possibly related to a combination of diagenetic processes (opal diagenesis, smectite to illite transformation, or the dissolution/precipitation of other minerals) as well as thermal alteration during and after sill intrusion. Alternatively, data variability and some excursions may reflect erratic contamination of sediment derived from drilling-induced generation of core fragments that mix with drilling mud during XCB coring.

4.1.3.7. Organic geochemistry

At Site U1545, we performed analyses of gas and solid-phase samples. For Hole U1545A, one headspace gas sample was analyzed per 9.5 m of core for routine hydrocarbon safety monitoring. The carbon, nitrogen, and sulfur content of particulate sediment was characterized, and source rock analysis was performed on selected solid-phase samples. For Hole U1545B, hydrocarbons were analyzed for both headspace gas and void gas; the amount of void space was quantified; H_2 and CO contents were measured; the carbon, nitrogen, and sulfur contents of sediment were characterized; and a comprehensive suite of gas and sediment samples was taken for postexpedition analyses. The SMTZ is at approximately 40–50 mbsf in the three holes, and C_2 – C_6 hydrocarbons are detectable below 100 mbsf. In Hole U1545A, low C_1/C_2 values below the thin basaltic rock layer necessitated the termination of drilling. From elemental and source rock analysis, we infer that the primary source of organic matter is marine in origin and the thermal maturity of organic matter varies based on the proximity of the sill. In Holes U1545B and U1545C, H_2 and CO are present in low concentrations, which suggests that biological cycling is the dominant control on these gases.

4.1.3.8. Microbiology

Sediment cores from below 480 mbsf in Hole U1545A and throughout Holes U1545B and U1545C span the temperature range from the cold seafloor to hot (~89°C) subsurface sediments that is potentially populated by psychrophilic, mesophilic, and thermophilic microorganisms. Thus, these cores were extensively sampled for microbiology and biogeochemistry, and those samples captured the entire spatial and thermal gradient in the penetrated sediment column at Site U1545. Syringe samples for cell counts, 3-D structural imaging, and RNA analyses were taken on the core receiving platform, preserved or frozen, and stored for further analyses. Whole-round samples were either stored in a -80°C freezer or temporarily stored in a 4°-8°C cold room and processed further for shore-based analyses. Here and at all other Expedition 385 sites, whole-round sample processing was conducted either inside a Coy Laboratory Products anaerobic chamber equipped with Table KOACH air purification unit or on the bench with a KOACH open clean zone system to maintain conditions that were as sterile as possible. Samples for PFT measurements were taken by syringe at 11 distinct sediment horizons on the core receiving platform. Shipboard cell counts showed that abundance gradually decreases with depth from 5.8 × 108 cells/cm3 at the seawatersediment interface to 8.2×10^5 cells/cm³ at approximately 150 mbsf. Except for a local spike at 290 mbsf (Section 385-U1545B-50F-3) with a cell abundance of 3×10^5 cells/cm³, cell numbers farther downhole drop below the detection limit of the protocol that we used for the shipboard cell counting program.

4.1.3.9. Petrophysics

Physical properties of whole-round and split cores were measured in the laboratory, and in situ measurements were made using downhole logging tools. Measurements on whole-round and working-half sections from Holes U1545A–U1545C were compared with each other and with downhole measurements from Hole U1545A for lithostratigraphic characterization and integration of core description, borehole data, and seismic profiles. These measurements included whole-round bulk density estimated from gamma ray attenuation (GRA) bulk density, magnetic susceptibility (MS), natural gamma radiation (NGR) (sensitive to the abundance of minerals containing radioisotopes of K, U, and Th), *P*-wave velocity, and discrete measurements of moisture and density (MAD) (to estimate porosity), thermal conductivity, three-component *P*-wave velocity, and rheological properties (shear and compressional strength). Two types of changes were observed in the GRA bulk density. The first type is observed in the uppermost 100 m of sediment and the second type to ~280 mbsf. Density generally increases by 0.11 g/cm³ every 100 m. A

steeper increase in density (0.14 g/cm³ every 100 m) was observed from ~280 mbsf to the final curated depth of Hole U1545A at 507.7 mbsf. This density increase is particularly well correlated with NGR values and corresponds to a change in lithology from diatom clay to siliceous claystone. MS values show peaks at 60, 170, and 482–483 mbsf that are also seen in the bulk density and NGR data. Two downhole logging tool strings were run in Hole U1545A: the triple combo (NGR, porosity, and density, including MS, resistivity, caliper, and logging head temperature) and FMS-sonic (resistivity images, caliper, acoustic velocity, and NGR) tool strings. Because of a malfunctioning caliper on the upward pass, only one pass was possible with the triple combo. In general, downhole measurements are consistent with results obtained from the whole-round and working-half cores. In addition to the logging tools, nine in situ formation temperature measurements were conducted with the APCT-3 and SET2 tools, indicating that temperature increases with depth along a linear geothermal gradient of 225°C/km that corresponds to a calculated heat flow of 161 mW/m².

4.2. Site U1546

4.2.1. Background and objectives

Site U1546 (proposed Site GUAYM-02B) is located just 1.1 km away from Site U1545 and ~51 km northwest of the axial graben of the northern Guaymas Basin spreading segment (Figures F1, F4). The primary objective was to compare these two adjacent sites that have shared sedimentation history but very different degrees of alteration resulting from intruding sills. Preexpedition seismic survey data at Site U1546 revealed a bright reflector at ~2.6 s TWT that was interpreted to be the contact with a sill intrusion. Disruption of the sedimentary strata above the interpreted sill (~2.3–2.6 s TWT) was supposed to have formed as a response to the sill emplacement. This feature abruptly terminates laterally toward Site U1545, coincident with the termination of the underlying sill. This same sedimentary sequence appears undisrupted at Site U1545 to ~2.8 s TWT, where another sill was observed in the seismic data. The shared objective for Sites U1545 and U1546 was to compare the composition, physical properties, geochemical gradients, and microbial communities at these sites. Thus, the major objective for Site U1546 was to provide a postintrusion sedimentary succession for comparison with the reference Site U1545; this comparison will provide direct measurements of changes in response to sill intrusion.

4.2.2. Operations

We cored four holes at Site U1546. Hole U1546A is located at 27°37.8851'N, 111°52.7939'W in a water depth of 1586.1 m. In Hole U1546A, we used the APC, HLAPC, and XCB systems to advance from the seafloor to a final depth of 361.2 mbsf with a recovery of 365.7 m (101%). We performed formation temperature measurements at several depths using the APCT-3 and SET2 tools. In Hole U1546B, located at 27°37.8840'N, 111°52.7809'W in a water depth of 1585.6 m, we deployed the APC, HLAPC, and XCB systems. Cores penetrated from the seafloor to a final depth of 333.8 mbsf and recovered 351.2 m (105%). In Hole U1546C, located at 27°37.8724'N, 111°52.7568'W in a water depth of 1596.6 m, we first drilled without core recovery from the seafloor to 308.2 mbsf. Then, the rotary core barrel (RCB) system was deployed to advance from 308.2 mbsf to a final depth of 540.2 mbsf with a recovery of 139.7 m (60%). Coring was terminated when the safety monitoring for hydrocarbon gases obtained an anomalously low C_1/C_2 value. We then conducted downhole wireline logging in Hole U1546C with the triple combo and FMS-sonic logging tool strings. In Hole U1546D, located at 27°37.8943'N, 111°52.7812'W in a water depth of 1585.9 m, we deployed the APC, HLAPC, and XCB systems to advance from the seafloor to a final depth of 300.1 mbsf with a recovery of 314.7 m (105%). Holes U1546B and U1546D were dedicated to extensive microbial and biogeochemical sampling that required the deployment of PFTs downhole on all cores to monitor drilling fluid (seawater) contamination. The pace of coring in Holes U1546B and U1546D was at times adjusted to accommodate the complex microbial sampling program conducted on the core receiving platform. A total of 270.7 h, or 11.3 days, were spent at Site U1546. Cores, penetration depths, core recovery, and operations schedule for all holes of Site U1546 are listed in Table T1.

4.2.3. Principal results

4.2.3.1. Lithostratigraphy

Of the four holes cored at Site U1546, the most complete and deepest record of soft and indurated sediments as well as igneous rocks is represented by the combination of results from Holes U1546A and U1546C. The sediments recovered are middle to late Pleistocene in age, mostly laminated to homogeneous diatom ooze to diatom clay forming a single lithostratigraphic unit (Unit I) (Figure F6). Subordinate lithologic components include nannofossils, silt-sized siliciclastic particles, and authigenic minerals such as pyrite and clay- to silt-sized carbonate (micrite). The latter is mainly dolomitic in composition and occurs as scattered crystals in the sediment. Carbonate also occurs as discrete concretions and ultimately as indurated limestone/dolomite intervals at depth. The distribution of authigenic carbonates as well as the biogenic (opal-A) to authigenic (opal-CT, quartz) silica phase transformations produce subtle yet distinct lithologic changes supporting the division of Unit I into four subunits (IA-ID). The transitions between the subunits are generally gradual, occurring over more than 10 m thick intervals, and can be difficult to define in low recovery or heavily sampled zones. The clay-rich diatom ooze of Subunit IA becomes more micritic in Subunit IB, which in turn is underlain by the less calcareous, largely micrite-free Subunit IC. The Subunit IC-ID transition is marked by diatom (opal-A) dissolution, the appearance of opal-CT, and ultimately authigenic quartz that heralds the formation of siliceous claystone in Subunit ID. Although the subunit divisions are similar to those at Site U1545, Subunit IB is thicker and shallower at Site U1546. There are also distinct zones of altered sediment above and below the thick mafic sill interval in Subunit ID that was fully penetrated in Hole U1546C. The mixed biogenic and siliciclastic sediments and their characteristic lamination are consistent with a middle to late Pleistocene, hemipelagic and suboxic to anoxic depositional environment.

4.2.3.2. Igneous petrology and alteration

Mafic sill material was encountered in Holes U1546A and U1546C at 354.6 and 348.2 mbsf, respectively. In Hole U1546A, the massive hypabyssal sill was penetrated over an interval of 6.0 m, whereas Hole U1546C was cored through the lower sill/sediment contact, resulting in a total sill thickness of 82.2 m based on drilling and ~75 m according to downhole logging data. The sill is made up of highly altered basaltic rock at the top followed by doleritic and gabbroic intervals. A doleritic texture resumes below the gabbroic interval and is followed by a short basaltic interval at the bottom contact. The upper- and lowermost basaltic rock intervals have chilled margin contacts with the adjacent sediments, being highly altered and vesicular with rounded to subrounded calcite amygdules. The cryptocrystalline groundmass hosts plagioclase phenocrysts. The doleritic intervals close to the basaltic layers are sparsely vesicular and gradually turn into nonvesicular doleritic rock toward the center of the sill. A ~12 m thick gabbroic interval is intercalated between the doleritic layers. The contacts between gabbroic and doleritic lithologies are both sharp and gradational. Plagioclase phenocrysts are present throughout the doleritic intervals, whereas pyroxene pseudomorphs occur as a minor phenocryst phase in the bottom doleritic layer, below the gabbroic interval. No pyroxene phenocrysts were observed in the upper doleritic part of the sill intrusion. This sill shows a subalkaline, tholeiltic mafic rock chemistry that corresponds to an enriched mid-ocean-ridge basalt (MORB) composition.

4.2.3.3. Structural geology

A few intervals of tilted beds were seen in the sedimentary section of Lithostratigraphic Unit I. Hole U1546A has tilted bedding in the uppermost two subunits (IA and IB) from 98 to 117 mbsf. Also, tilted bedding occurs in Subunit IB from 115 to 124 mbsf in Hole U1546B and from 112 to 120 mbsf and from 145 to 156 mbsf in Hole U1546D. Brittle fractures and faults were found in sedimentary cores below 200 mbsf in Hole U1546D and below 166 mbsf in Hole U1546B. They have intermediate apparent dips $(30^{\circ}-60^{\circ})$. Where displacements could be measured, they were ≤ 5 cm. Six vertical veins were measured in sedimentary rocks at 433 mbsf in Hole U1546C. In the recovered igneous rocks, fractures and veins were measured for true dip from whole-round cores before they were split. A total of 49 such structures were identified in Hole U1546C. No veins were seen in the igneous rocks at the bottom of Hole U1546A.

4.2.3.4. Biostratigraphy

At Site U1546, preservation of calcareous nannofossils is good/moderate to poor throughout the entire sedimentary sequence. In general, nannofossils are abundant and well preserved in the upper ~ 100 m of the sequence. Below ~ 100 mbsf, intervals with barren/few and common/abundant nannofossils alternate. Preservation is good/moderate in samples with common/abundant

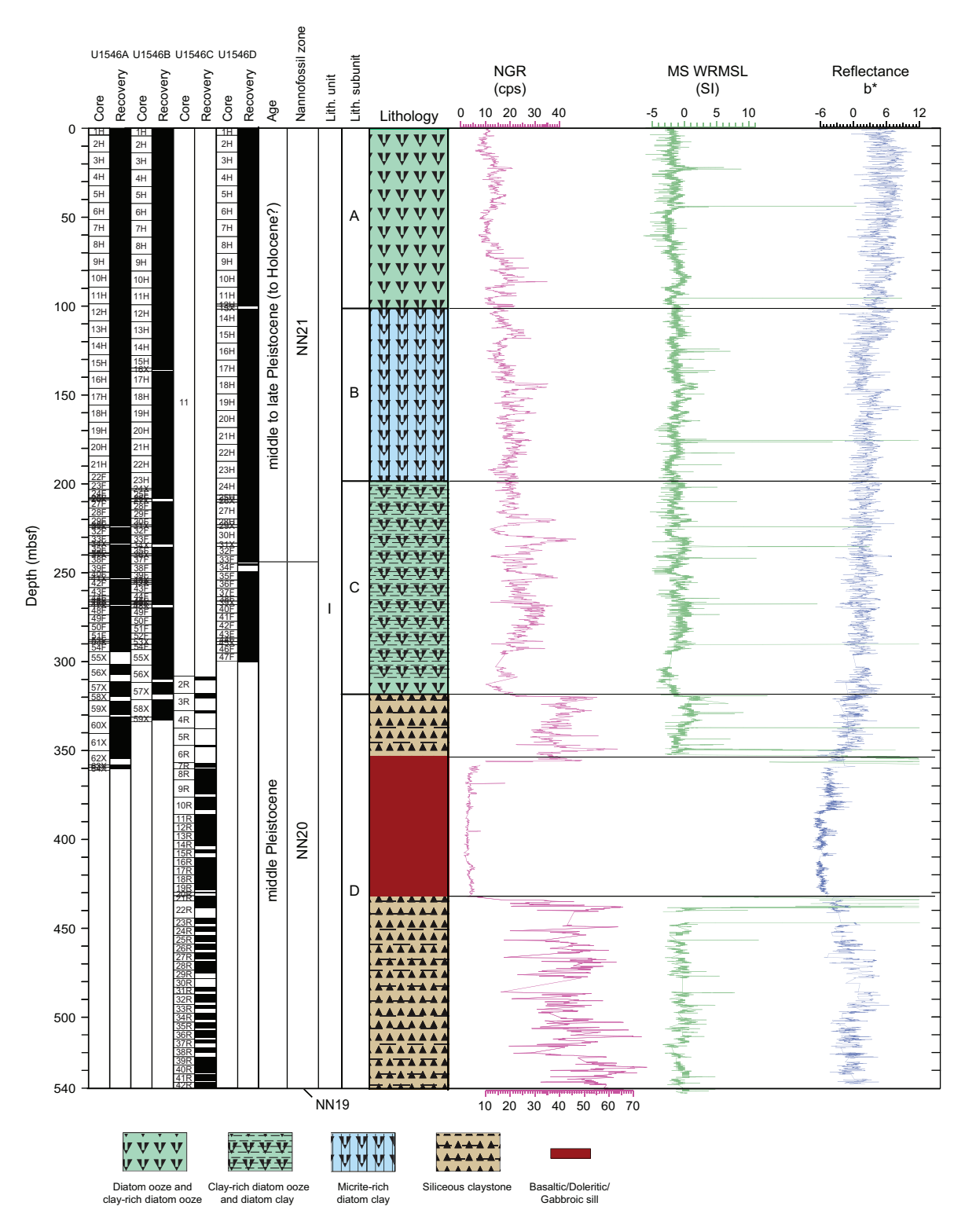


Figure F6. Lithostratigraphic column, Site U1546. NGR = natural gamma radiation, cps = counts per second, MS = magnetic susceptibility, WRMSL = Whole-Round Multisensor Logger. All data on display obtained from Holes U1546A and U1546C, including the lithostratigraphic information.

nannofossils and poor in those with few/rare abundances. In general, marine diatoms are dominant/abundant with good/moderate preservation to ~312 mbsf and barren to the bottom of Holes U1546A and U1546C. The lowermost appearance (first appearance datum) of the calcareous nannofossil *E. huxleyi* dates the upper part of the sediment sequence to (Holocene–)late–middle Pleistocene (younger than 0.29 Ma; 0–249.28 mbsf in Hole U1546A). In contrast, the absence of calcareous nannofossil *P. lacunosa* and marine diatom *F. reinholdii* in the underlying interval indicates a middle Pleistocene age (0.29–0.44 Ma) for the lower part of Hole U1546A. *P. lacunosa* was observed in the basal core catcher sample from Hole U1546C (539.84 mbsf), suggesting an age older than the uppermost appearance (last appearance datum [LAD]) of *P. lacunosa* at 0.44 Ma. The estimated average sedimentation rate is 1020 m/My (102 cm/ky) at this site.

4.2.3.5. Paleomagnetism

AF demagnetization was implemented with the SRM on archive-half sections up to 20 mT on all cores from Holes U1546A and U1546C. The drilling-induced overprint was successfully removed from all APC and HLAPC cores (from the seafloor to ~270 mbsf) upon demagnetization. In Hole U1546A, inclination values after demagnetization at 20 mT cluster around 43°, which is slightly lower than the expected GAD inclination at the latitude of the site (46.3°). A detailed analysis of the remanence of discrete samples from Hole U1546A showed that the drilling-induced overprint is removed by 10 mT and the ChRM agrees with the SRM measurements. Unfortunately, the XCB and RCB cores were irreversibly overprinted. The NRM of archive-half sections decreases at ~80-100 mbsf (Hole U1546A), a depth interval that corresponds to the SMTZ zone. The magnetic mineral assemblage becomes coarser, and low-coercivity minerals such as (titano)magnetite are dominant. The AF demagnetization protocol was not effective for the igneous rock sections from Hole U1546C. Therefore, we focused on thermal demagnetization of discrete samples. Two groups of samples distributed in the sill intrusion were identified: a first group in the upper 18 m of the sill contains fine-grained magnetite, and a second group is dominated by coarse-grained titanomagnetite in the bottom 57 m. AMS shows a mixture of prolate and oblate behavior above the sill and a dominant prolate behavior below it. All cores in Holes U1546A and U1546C were assigned to the normal Brunhes Chron C1n (younger than 0.78 Ma). No paleomagnetic measurements were conducted in Holes U1546B and U1546D.

4.2.3.6. Inorganic geochemistry

A total of 94 IW samples were collected from the sedimentary succession at Site U1546 (Holes U1546A-U1546D). Based on the sulfate and methane profiles, the SMTZ is estimated to be at ~110 mbsf, approximately twice as deep compared to Site U1545. Around this depth, sulfide, alkalinity, and phosphate reach their maximum values and barium concentration starts to increase. However, the depth of maximum concentrations of alkalinity and phosphate is slightly offset from the SMTZ. Ammonium gradually increases downhole until an alteration zone above the sediment/sill contact records a drop between 300 and 330 mbsf; its maximal concentration of 12-14 mM, compared to over 30 mM at Site U1545, indicates decreased biomineralization of organic matter. Biogeochemical processes observed from the seafloor to 120 mbsf are mainly related to anaerobic degradation of organic matter and sulfate-dependent anaerobic oxidation of methane. Just above and below the sill, a number of significant variations were observed for many IW dissolved elements (such as K+, B, Mg2+, Sr2+, Li+, and Ba2+), which could be related to changes in mineralogic composition derived from sill-induced alteration. Between the SMTZ and the sill intrusion, the IW chemical properties are likely to be influenced by combined biogeochemical processes and sediment-water interaction associated with the sill intrusion and by precipitation/dissolution processes including opal-A dissolution and authigenic carbonate precipitation.

4.2.3.7. Organic geochemistry

At Site U1546, we sampled and analyzed gas and solid-phase samples. In Holes U1546A–U1546D, one headspace gas sample was analyzed per 9.5 m advance for routine hydrocarbon safety monitoring. The carbon, nitrogen, and sulfur contents of particulate sediment were characterized, and source rock analysis was performed on selected solid-phase samples. For the sediments recovered in Holes U1546B and U1546C, both headspace and void gas were analyzed for their hydrocarbon contents, the amount of void space was quantified, $\rm H_2$ and CO contents were measured, and the carbon, nitrogen, and sulfur contents of sediment were characterized. During igneous rock recovery in Hole U1546C, whole-round core pieces of rock were incubated in sealed trilaminated foil

barrier bags to examine degassing of hydrocarbons from freshly recovered whole-round sill cores. In general, methane increases with depth in each hole with 1–2 local maxima. C_2 – C_6 hydrocarbons are detectable below ~90 mbsf, and they all increase with depth. In Hole U1546C, low C_1/C_2 values eventually necessitated the termination of coring. From elemental and source rock analysis we infer that the primary source of organic matter is marine in origin and the thermal maturity of organic matter varies based on the proximity of the sill. In Holes U1546B and U1546C, H_2 and CO are present in nanomolar concentrations.

4.2.3.8. Microbiology

Sediment cores for microbiological studies were obtained from APC, HLAPC, and XCB cores in Holes U1546B and U1546D. After drilling to 308 mbsf without core recovery, Hole U1546C was also sampled along its deeper, hydrothermally heated sediment column above and below the penetrated sill. These Hole U1546C samples represent important horizons that will further our understanding of the impact sill emplacement has on geochemistry and extant microbial communities within the hyperthermophilic zone. Syringe samples for cell counts, 3-D structural imaging, and RNA analyses were taken on the catwalk, fixed or frozen, and stored for further analyses. Whole-round samples were either stored in a -80° C freezer or temporarily stored in a cold room (4° -8° C) and then processed for shore-based analyses, as described for Site U1545. Samples for PFT measurements were taken on the core receiving platform by syringe at 17 horizons. Cell abundance for selected samples was determined by direct counting with an epifluorescence microscope. Cell abundance in seafloor sediment (1.0 × 10^9 cells/cm³) was roughly 1000 times higher than the bottom seawater (1.1 × 10^6 cells/cm³) and gradually decreased to 4.3×10^6 /cm³ at approximately 132 mbsf. In deeper intervals, cell abundance generally dropped below the detection limit of the protocol used for the shipboard cell counting program.

4.2.3.9. Petrophysics

Physical properties of the recovered cores were measured on whole-round and working-half sections. Downhole wireline logging was used to measure host formation physical properties. Measurements on whole-round and working-half sections from Holes U1546A-U1546D were compared with each other and with downhole measurements obtained from Hole U1546C for lithostratigraphic characterization and correlation between core description, logging data, and preexpedition seismic survey profiles. Our analysis identified the same two large-scale major petrophysical variations found at Site U1545 and a transition at ~280 mbsf. All physical properties highlight the presence of a ~74 m thick sill at ~355 mbsf. Twelve in situ formation temperature measurements were conducted using the APCT-3 and SET2 tools. Measured values indicate that temperatures increase with depth along a linear geothermal gradient of 221°C/km that corresponds to a calculated heat flow of 160 mW/m². Thermal conductivity varies between ~0.66 and ~1.00 W/(m·K) in the first ~345 mbsf, which marks the upper sill/sediment contact. Sixteen hard rock thermal conductivity measurements were made on sill samples from ~348 to ~432 mbsf, yielding a mean thermal conductivity of 1.72 ± 0.14 W/(m·K). Downhole logging caliper measurements clearly identify the sill-sediment transitions. Bulk density for sediments generally ranges from ~ 1.2 to ~ 1.5 g/cm³ and shows variations in trends at ~ 270 and ~ 310 mbsf. The average sill density of ~2.8 g/cm³ is typical for doleritic rock. Porosity shows a linear decrease from 90% at the seafloor to 73%-82% at ~309 mbsf. A significant decrease in sediment porosity was observed at the top and bottom contacts with the sill. Porosity inside the sill is relatively low (~3%) with some high values in the upper part of the sill. Compressive strength increases by 1.1 kPa/m, and shear strength increases by 0.6 kPa/m. NGR values increase from ~10 to 25 counts/s to 270 mbsf in the host sediments; these values then drop inside the sill. Downhole NGR measurements inside the sill are consistent with whole-round core laboratory measurements. Resistivity measurements reveal large relative variations of 0.4 to \sim 200 Ω m that typically correlate with variations in density and porosity. Core-based MS values are mainly constant to ~355 mbsf. P-wave velocity generally increases with depth and shows typical higher values for the sill.

4.3. Sites U1547 and U1548

4.3.1. Background and objectives

Sites U1547 and U1548 (proposed Sites GUAYM-12A and GUAYM-03B, respectively) are located ~27 km northwest of the axial graben of the northern Guaymas Basin (Figure F1). Site U1547 lies within a circular, bowl-shaped hydrothermal mound called Ringvent that rises ~20 m above the seafloor and has a maximum diameter of ~800 m. Three holes at Site U1548 (U1548A-U1548C) lie at the periphery of Ringvent's southeastern edge, and two holes (U1548D and U1548E) are situated ~600 m west-northwest of Ringvent (Figure F7). Seismic profiles across Ringvent show a prominent subseafloor mound feature at ~0.06 s TWT that is characterized by brightly reflective strata within the central bowl-shaped region. A bright reflector underlying the base of the bowl (at ~0.18 s TWT) is interpreted to be a sill intrusion. It is hypothesized that this and previous similar intrusions provided the heat that formed Ringvent and keep it active today. Ringvent is the bestcharacterized active, sill-associated hydrothermal system at an off-axis site in Guaymas Basin, and the temperature of its vent fluids varies between 20° and 75°C (Teske et al., 2019). Site survey data suggest that the central portion of Ringvent may thus function as a hydrothermal recharge zone. Therefore, Sites U1547 and U1548 were intended to core sediments and sills to explore patterns of hydrothermal circulation at Ringvent, which were suspected to be different within (Site U1547) and outside (Holes U1548A-U1548C) of the ring structure. The comparatively hot sill intrusion setting at Ringvent represents a shallow-emplacement end-member. The primary objectives for Sites U1547 and U1548 were thus to characterize the physical, chemical, and biological processes driven and affected by this end-member type of sill-sediment system, with a particular focus on the response of microbial communities to the expected steep temperature gradients at these sites. Moreover, two additional holes (U1548D and U1548E) in an area near Ringvent were added to Site U1548 during the expedition, with the joint objective of characterizing the geochemical signature of the abrupt lateral change in seismic character observed in sediment strata between ~2.39 and 2.42 s TWT, which may be related to a diagenetic change caused by the proximity to the igneous intrusions at Ringvent.

4.3.2. Operations

Sites U1547 and U1548 established a total of ten holes within or adjacent to the Ringvent structure to characterize this hydrothermal mound and its immediate surroundings.

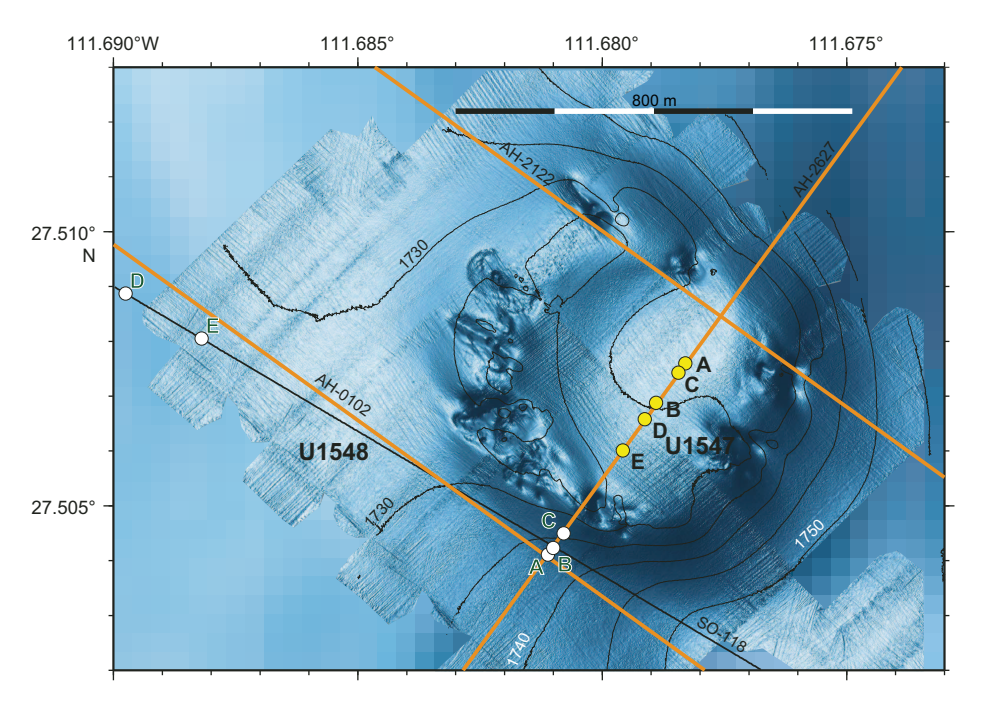


Figure F7. Bathymetric map showing all holes drilled inside and outside the circular hydrothermal mound structure called Ringvent, Sites U1547 and U1548. Locations of seismic crossing lines are also indicated. Contour lines = 5 m.

We cored five holes at Site U1547. Hole U1547A is located at 27°30.4561 N, 111°40.6980 W in a water depth of 1733.7 m. In Hole U1547A, we used the APC, HLAPC, and XCB systems to advance from the seafloor to a final depth of 141.3 mbsf with a recovery of 145.3 m (103%). We made formation temperature measurements at several depths using the APCT-3 and SET2 tools. In Hole U1547B, located at 27°30.4128'N, 111°40.7341'W in a water depth of 1732.2 m, we deployed the APC, HLAPC, and XCB systems. Cores penetrated from the seafloor to a final depth of 209.8 mbsf and recovered 161.3 m (77%). Formation temperature measurements were made at several depths using the APCT-3 and SET2 tools. Next, we deployed the Kuster FTS to successfully recover two borehole fluid samples, one each from 109.7 and 135.7 mbsf. We then conducted downhole wireline logging in Hole U1547B with the triple combo and FMS-sonic tool strings. In Hole U1547C, located at 27°30.4455'N, 111°40.7064'W in a water depth of 1732.2 m, we first drilled without core recovery from the seafloor to 81.3 mbsf. We then used the RCB system to advance from 81.3 mbsf to a final depth of 159.2 mbsf with a recovery of 9.0 m (12%). In Hole U1547D, located at 27°30.3947'N, 111°40.7483'W in a water depth of 1732.2 m, we first drilled without core recovery from the seafloor to 81.3 mbsf. We then used the RCB system to advance from 81.3 mbsf to a final depth of 193.0 mbsf with a recovery of 34.9 m (31%). The Elevated Temperature Borehole Sensor (ETBS) was deployed to make a temperature measurement at the bottom of the hole. In Hole U1547E, located at 27°30.3598'N, 111°40.7756'W in a water depth of 1732.1 m, we first drilled without core recovery from the seafloor to 61.8 mbsf. We then used the RCB system to advance from 61.8 mbsf to a final depth of 191.2 mbsf with a recovery of 44.9 m (35%). Holes U1547B-U1547D were dedicated to extensive microbial and biogeochemical sampling that required the deployment of PFTs downhole for all cores to monitor drilling fluid (seawater) contamination. A total of 235.0 h, or 9.8 days, were spent at Site U1547. Table T1 displays cores, penetration depths, core recovery, and operations schedule for all holes of Site U1547.

Five holes were cored at Site U1548. Hole U1548A is located at 27°30.2466'N, 111°40.8665'W in a water depth of 1739.9 m. In Hole U1548A, we deployed the APC and XCB systems. Cores advanced from the seafloor to a final depth of 103.4 mbsf and recovered 114.0 m (110%). We made formation temperature measurements at several depths using the APCT-3 tool. In Hole U1548B, located at 27°30.2540 N, 111°40.8601 W in a water depth of 1738.9 m, we deployed the APC and XCB systems to advance from the seafloor to a final depth of 95.1 mbsf with a recovery of 87.7 m (92%). We made formation temperature measurements at several depths with the APCT-3 and SET2 tools. We then deployed the Kuster FTS to successfully recover a borehole fluid sample from 70.0 mbsf. In Hole U1548C, located at 27°30.2698'N, 111°40.8476'W in a water depth of 1737.0 m, we deployed the APC and XCB systems to advance from the seafloor to a final depth of 69.8 mbsf with a recovery of 71.0 m (102%). We made formation temperature measurements at several depths with the APCT-3 and SET2 tools. In Hole U1548D, located at 27°30.5316'N, 111°41.3855′W in a water depth of 1729.3 m, we deployed the APC and HLAPC systems. Cores penetrated from the seafloor to a final depth of 110.0 mbsf and recovered 120.5 m (110%). Formation temperature measurements were made at several depths using the APCT-3 tool. In Hole U1548E, located at 27°30.4829'N, 111°41.2922'W in a water depth of 1729.9 m, we deployed the APC system. Cores penetrated from the seafloor to a final depth of 110.0 mbsf and recovered 115.2 m (105%). We conducted formation temperature measurements at several depths using the APCT-3 tool. Holes U1548B and U1548C were dedicated to extensive microbial and biogeochemical sampling that required the deployment of PFTs downhole for all cores to monitor drilling fluid (seawater) contamination. A total of 94.6 h, or 3.9 days, were spent at Site U1548. Table T1 displays cores, penetration depths, core recovery, and operations schedule for all holes of Site U1548.

4.3.3. Principal results

4.3.3.1. Lithostratigraphy

This lithostratigraphic summary characterizes both Site U1547 and Site U1548, which are located only a few hundred meters from each other (maximum distance between holes = \sim 800 m). Site U1547 and Holes U1548A–U1548C were drilled inside or adjacent to the Ringvent structure, and Holes U1548D and U1548E were drilled \sim 600 m west-northwest of Ringvent. The sediments recovered at Sites U1547 and U1548 are middle to late Pleistocene in age and mostly biogenic (mainly diatom ooze), although the proportion of siliciclastic components is more significant

compared to Sites U1545 and U1546 in northwest Guaymas Basin (Figures F8, F9, F10). The sequence recovered at Sites U1547 and U1548 shows downhole changes in the lithologic characteristics of the sediment that are related to changes in (1) the abundance ratio between diatom ooze and clay minerals, (2) the abundance of carbonate precipitates, and (3) to a lesser extent, the diagenetic changes of biogenic silica. Downhole changes in lithology at Sites U1547 and U1548 are not significant enough to require division into more than one lithostratigraphic unit but are sufficient to warrant the division of Unit I into four subunits at Site U1547 and three subunits at Site U1548 (Figures F8, F9, F10). The uppermost subunit (IA) is made up of a similar lithology at both sites, mainly consisting of more or less laminated diatom ooze mixed with different amounts of clay minerals. The boundary between Subunits IA and IB is located at ~40 mbsf in holes at both sites except in Hole U1548C, where it occurs at ~27 mbsf. Subunit IB is mainly composed of varying proportions of diatoms and clay with the addition of significant (>5%) micrite (euhedral to subhedral, micrometer-sized, authigenic carbonate particles). Gray silty beds, often showing erosional bottom contacts, are also frequent, and some of these beds attain thicknesses of up to 1.2 m. The top of Subunit IC (only observed in Hole U1548C) is very thin and coincides with a significant drop in micrite content in the sediment, although limestone/dolostone intervals still persist. The main lithologies are diatom clay and clay-rich diatom ooze. Sandy and silty intervals are also common, and some intervals display evidence of syndepositional deformation. Subunit ID was only recovered at Site U1547, where it is a dusky yellowish brown siliceous claystone. Diatoms are absent, and X-ray diffraction mineralogy indicates the onset of silica phase transition from opal-A to opal-CT. Basalt occurs at shallow depths at Sites U1547 (130.5-150 mbsf) and U1548 (90-100 mbsf). However, poor recovery provides only limited observations of contact zones with the adjacent sediment.

4.3.3.2. Igneous petrology and alteration

Mafic rocks from sill intrusions underlying the Ringvent structure were recovered in Holes U1547A–U1547E within the circular Ringvent mound and Holes U1548A–U1548C outside of the Ringvent mound at its periphery. The sill bodies were encountered at different depths and were

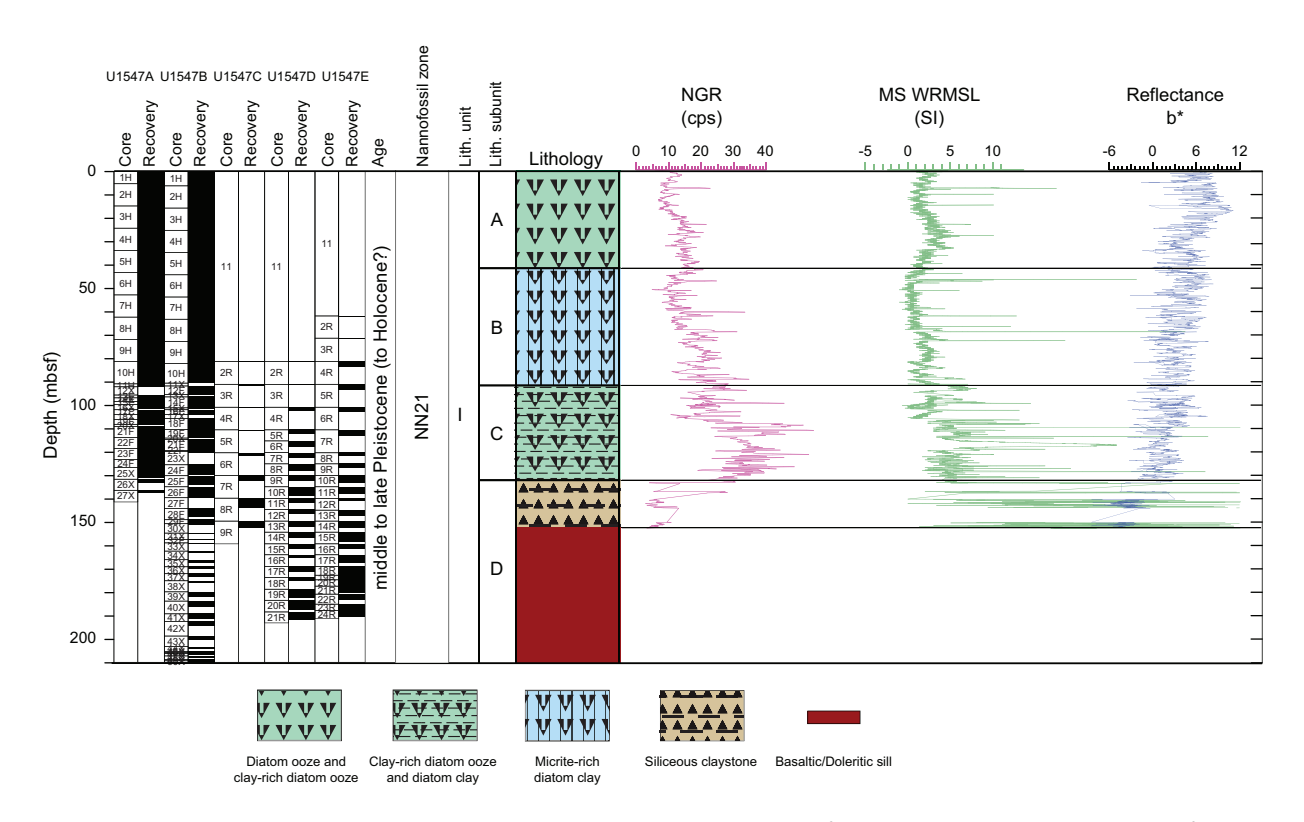


Figure F8. Lithostratigraphic column, Site U1547. Lithologic column represents Hole U1547B. Data are from Hole U1547A except ~130–150 mbsf, where data are from Hole U1547C (magnetic susceptibility [MS] peaks are out of scale and not entirely plotted). The MS plot shows no data between ~150 and 210 mbsf because this interval corresponds to the igneous sill where Fe-rich igneous rocks yield MS values two orders of magnitude higher than adjacent sediments. NGR = natural gamma radiation, cps = counts per second, WRMSL = Whole-Round Multisensor Logger.

recovered at varying rates. Sills recovered at Site U1547 are mostly composed of aphyric to clinopyroxene-plagioclase phyric basalt. A ~20 m thick doleritic section was recovered from the bottom part of Hole U1547E (to 191 mbsf) and includes plagioclase and pyroxene phenocrysts 2–5 mm in size. The basaltic material is slightly to moderately vesicular, whereas doleritic intervals are nonvesicular to slightly vesicular. The subangular to subrounded vesicles range from 1 to 25 mm in diameter. Vesicles are either empty or partially/fully filled with carbonate that is often associated with pyrite (<0.5 mm). Empty vesicles are often coated with secondary bluish gray silicate material. The recovered basalts show variable degrees of alteration. Monomineralic carbonate veins are often surrounded by thin halos of pyrite. Occasionally, the latter also occurs as subordinate vein-filling material. In terms of modal composition, basalts recovered at Site U1548 resemble those from Site U1547, but they are darker in color and usually nonvesicular. Other common features observed in igneous rock cores from Holes U1547A–U1547E and U1548A–U1548C are injected sedimentary veins, contacts between sedimentary breccia and basalt, sediment-magma mingling (peperite facies), and glassy chilled margins. The presence of glassy chilled margins suggests direct contact of the magma with very wet sediment. Chemical data obtained from Site

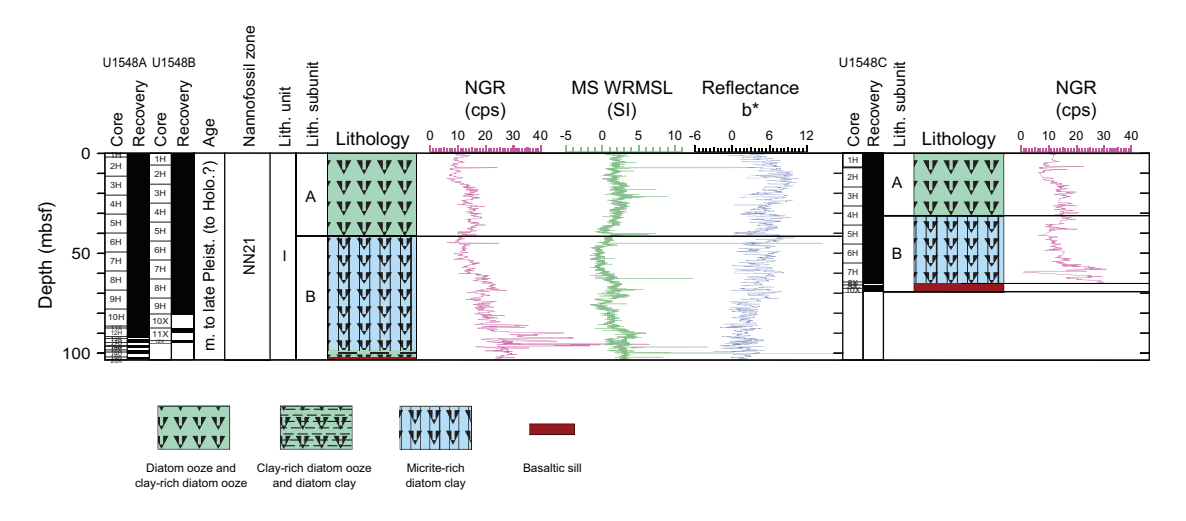


Figure F9. Lithostratigraphic column, Holes U1548A–U1548C. Data are from Hole U1548A. Lithostratigraphy and natural gamma radiation (NGR) are plotted separately for Hole U1548C. cps = counts per second, MS = magnetic susceptibility, WRMSL = Whole-Round Multisensor Logger.

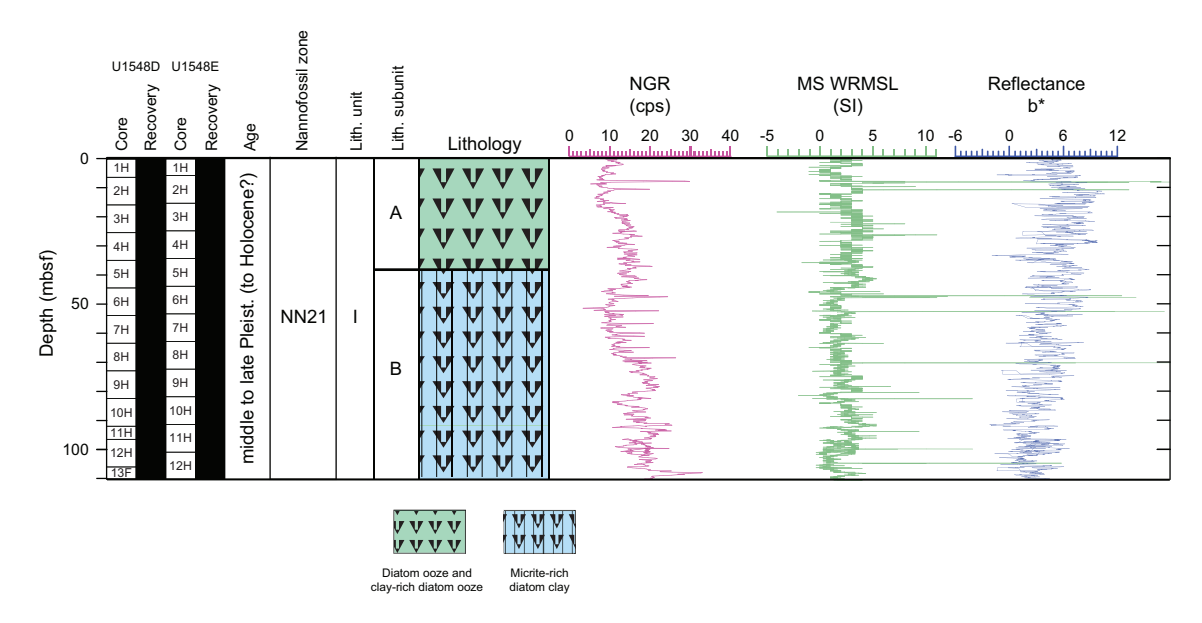


Figure F10. Lithostratigraphic column, Holes U1548D and U1548E. Data are from Hole U1548D. NGR = natural gamma radiation, cps = counts per second, MS = magnetic susceptibility, WRMSL = Whole-Round Multisensor Logger.

U1547 sill intervals overall reveal a subalkaline, tholeiitic mafic rock chemistry, with few samples from Holes U1547D and U1547E showing a calc-alkaline character. Based on their Ti-V pattern, all rock samples point to an enriched MORB composition.

4.3.3.3. Structural geology

We made structural observations in all ten holes within (Site U1547) or near (Site U1548) the Ringvent structure. Structural information was sought from sedimentary units in four of the five holes at Site U1547 and all five holes at Site U1548. Hole U1547A was lithologically the most complete hole for examining the sedimentary succession. Bedding and lamination in sediments show no significant folds and few brittle fractures and faults, although in some cases fractures are seen much more easily in the X-ray images than on the cut surfaces of the cores. Additional structural information came from the basaltic rocks in Subunit ID, which were cored in eight of the holes. Holes U1547B, U1547D, and U1547E recovered the most mafic hypabyssal rock. Structural features observed in the basaltic rocks include preexisting fractures and faults, mineralized veins, glassy margins, sediment-filled veins, and fragments of columnar joints. Where possible, these features were measured for true dip and await possible reorientation using shore-based paleomagnetic results. Networks of veins with irregular branching patterns were not measured as planar features. No macroscopic shortening or folding of the veins was evident.

4.3.3.4. Biostratigraphy

Calcareous nannofossils are abundant to common above 43.51 mbsf at Site U1547 and in Holes U1548A-U1548C. This interval is followed by an alternation between intervals with few or barren occurrences of nannofossils and intervals with abundant/common populations from 43.73 to 151.93 mbsf at both sites. Nannofossil preservation varies from good to poor throughout the entire sedimentary sequence and is generally good and moderate in samples with abundant and common abundances and poor in those with few and barren abundances. In general, marine diatoms are dominant and abundant with good to moderate preservation above 131.21 mbsf in Hole U1547A, above 101.15 mbsf in Hole U1547B, above 81.6 mbsf in Hole U1547C, and above 91.25 mbsf in Hole U1547D. The barren intervals at the bottom of Site U1547 and in Holes U1548A-U1548C might be due to diagenetic alteration. In Hole U1548A, marine diatoms are mostly abundant with moderate preservation above 84.1 mbsf, whereas they are abundant to few and poorly preserved in the bottom interval (90.9-99.0 mbsf). In Holes U1548D and U1548E, calcareous nannofossils are common to abundant with moderate and poor preservation in most samples examined, except for those from three sampled depths (31, 92.29, and 101.58 mbsf) in Hole U1548D. Marine diatoms are dominant and abundant with good and moderate preservation throughout Holes U1548D and U1548E. The occurrence of calcareous nannofossil species E. huxleyi to the bottom of all holes dates the entire sediment sequence to (Holocene-)late-middle Pleistocene, or younger than 0.29 Ma (Hole U1547A = 0-137 mbsf, Hole U1547B = 0-151.93 mbsf, Hole U1547C = 0-121.13 mbsf, Hole U1547D = 0-101.33 mbsf, Hole U1548A = 0-99 mbsf, Hole U1548D = 0-110.24 mbsf, and Hole U1548E = 0-91.81 mbsf). This age assignment is consistent with the absence of calcareous nannofossil species P. lacunosa (LAD = 0.44 Ma) and F. reinholdii (LAD = 0.62 Ma) in all examined samples. The estimated average sedimentation rate is >524 m/My (>52.4 cm/ky).

4.3.3.5. Paleomagnetism

AF demagnetization up to 20 mT was conducted with the SRM on all sediment archive-half sections from Holes U1547A, U1548A, and U1548C–U1548E (APC, HLAPC, and XCB cores). The drilling-induced overprint was successfully removed from all cores upon demagnetization. Mean inclination values after demagnetization at 20 mT cluster around 46° at Site U1547 (Hole U1547A) and vary between ~40° and 47° at Site U1548, values that are comparable to the expected GAD inclination at the latitude of the sites (46.2°). A detailed analysis of the remanence of discrete samples from Sites U1547 and U1548 shows that the drilling-induced overprint is removed by 10 mT and the ChRM is in accordance with the SRM measurements. The NRM of archive-half sections decreases at ~30–35 mbsf in Holes U1547A and U1548A and at ~65–70 mbsf in Holes U1548D and U1548E. The magnetic mineral assemblage becomes coarser, and low-coercivity minerals, likely (titano)magnetite, are dominant. The AMS of sediments in Holes U1547A, U1548A, and U1548C–U1548E shows a mixture of prolate, oblate, and triaxial behavior in the vast majority of sampled depths. The igneous rock archive-half sections from Holes U1547B–U1547E, U1548A,

and U1548C were measured for their NRM only because the AF demagnetization protocol was not effective for the igneous sections. All cores at Sites U1547 and U1548 were assigned to the normal Brunhes Chron C1n (younger than 0.78 Ma).

4.3.3.6. Inorganic geochemistry

A total of 32 IW samples were collected from the sediment columns in Holes U1547A and U1547B, and 68 were collected from the sedimentary successions in Holes U1548A-U1548E. In addition, 27 and 20 IW samples from sediments in Hole U1547A and Hole U1548A, respectively, were collected using Rhizon samplers. The holes at Sites U1547 and U1548 are divided into three groups: holes inside (U1547A-U1547E), peripheral to (U1548A-U1548C), and nearby (U1548D and U1548E) Ringvent. Above the encountered sills at Ringvent, the IW profiles show similar trends in all Site U1547 holes and in Holes U1548A-U1548C, with slight differences mainly in sulfate, alkalinity, phosphate, and sulfide concentrations. Alkalinity (~13-18 mM) and ammonia concentration maxima (~4-9 mM) in these holes are consistently the lowest of this expedition, indicating reduced biomineralization in sediments above the Ringvent sill. Abrupt changes were observed for many elements in the contact interval with the sill, suggesting that the sill acts as a source or sink: sulfate sharply decreases to depletion over a few meters coincident with increases in Li+, Ba2+, B, Sr2+, Ca2+, and Na+ and decreases in Mg2+, K+, and H4SiO4. Similar excursions were observed at Sites U1545 and U1546 above the sills. The IW chemical properties are likely influenced by sediment-fluid interaction associated with the sill intrusion, and by precipitation/dissolution processes associated with sediment diagenesis, including opal-A dissolution and to a lesser extent by combined biogeochemical processes. Northwest of Ringvent, the IW profiles in Holes U1548D and U1548E behave differently compared to the holes located inside Ringvent. In general, concentrations of alkalinity, ΣH₂S, NH₄+, and PO₄³⁻ produced by organic matter mineralization are higher in Holes U1548D and U1548E than in Ringvent Holes U1548A-U1548C. The SMTZ in Holes U1548D and U1548E is well defined around 76 mbsf by a concave downward decrease in sulfate and a concomitant increase in alkalinity, HS^- , NH_4^+ , and PO_4^{3-} . Compared to the Ringvent holes, the lower concentrations of dissolved H₄SiO₄ in Holes U1548D and U1548E may reflect less alteration of silicate minerals or diatom tests due to the lower thermal gradient.

4.3.3.7. Organic geochemistry

At Sites U1547 and U1548, organic geochemists sampled and analyzed gas and solid-phase samples. For all holes, one headspace gas sample was analyzed per 9.5 m of advancement for routine hydrocarbon safety monitoring. Void spaces were measured on the core receiving platform, and void gases were characterized for their hydrocarbon content. The carbon, nitrogen, and sulfur contents of particulate sediment were characterized, and source rock analysis was performed on selected solid-phase samples. When sampling was focused on microbiology and biogeochemistry objectives, H₂ and CO contents were measured and gas and solid-phase materials were sampled for shore-based analyses. Headspace analyses of sediment and rock samples for methane and hydrocarbons yielded high concentrations that increased from the sediment column toward sill interfaces. CH₄ concentrations reached a maximum of 125 mM at the sill interface in Hole U1547B and often exceeded 10 mM when small pieces of sill rock were used for headspace incubations during igneous rock recovery. To further examine these results, pieces of rock from wholeround cores were incubated in sealed trilaminated foil barrier bags to examine degassing of hydrocarbons. Methane and higher hydrocarbons were found in high concentrations throughout Sites U1547 and U1548. Concentrations in sill rock depend strongly on rock density and porespace assumptions; with an average density of 2.7 g/ml and 14% porespace, methane concentrations would range approximately from 30 to 140 mM at Site U1547 (Holes U1547B-U1547E) and up to 35 mM at Site U1548 (Holes U1548A-U1548C). Using the same assumptions, hydrogen concentrations in sills would range mostly between 2 and 20 µM with occasionally higher values. Elemental analysis revealed that organic matter at these sites originates primarily from marine sources, although some intervals may be influenced by terrestrial inputs. Source rock analysis indicated that thermal maturity of organic matter varies based on sill proximity. In sediment pore water profiles, H₂ and CO show nanomolar concentrations and exhibit varying trends with depth.

4.3.3.8. Microbiology

The Ringvent sites present an opportunity to investigate the microbial consequences of elevated heat flow and hydrothermal circulation at Guaymas Basin off-axis sites. Previous sequencing stud-

ies of shallow piston-cored sediments from Ringvent revealed decreased microbial diversity and remnant populations of past methane seepage (Teske et al., 2019; Ramírez et al., 2020). Sediment cores for microbiological studies were obtained from Holes U1547B, U1548B, and U1548C using the APC and XCB systems. In addition, samples of igneous rock with indications of fluid-rock interaction, such as veins, sediment injections, and vesicularity with amygdules, were taken for microbiological studies from Holes U1547C-U1547E, U1548A, and U1548B. Syringe samples for cell counts, 3-D structural imaging, and RNA analyses were taken on the core receiving platform, preserved or frozen, and stored for further analyses. Whole-round core samples were either stored in a -80°C freezer or temporarily stored in a 4°-8°C cold room and processed further for shorebased analyses, as described for Site U1545. Samples for PFT measurements were taken on the core receiving platform by syringe from eight Hole U1547B cores and four Hole U1548B cores. Cell abundance was 1.0×10^9 cells/cm³ in seafloor sediment within the perimeter of Ringvent (Hole U1547B) and 5.4×10^8 cells/cm³ just outside of Ringvent (Hole U1548B). Cell abundance quickly decreased downhole at both Site U1547 (1.4×10^6 cells/cm³ at approximately 66 mbsf) and Site U1548 (1.3×10^6 cells/cm³ at approximately 57.7 mbsf in Holes U1548A–U1548C). Except for a few localized spikes, cells were not detected in deeper samples. These shallow depth limits for cell detection at Ringvent contrast with considerably deeper cell detection depths at Sites U1545 and U1546.

4.3.3.9. Petrophysics

Physical properties measured on whole-round and split core sections from Holes U1547A—U1547E and U1548A—U1548E were compared with each other and with downhole logging measurements from Hole U1547B for lithostratigraphic characterization and correlation between core description, logging data, and preexpedition seismic survey profiles. At Sites U1547 and U1548, a total of 31 in situ formation temperature measurements were taken with the APCT-3 and SET2 tools. The resulting geothermal gradient of ~511° to almost 960°C/km as well as thermal conductivity measurements were used to calculate a heat flow that varies between ~520 and ~930 mW/m², depending on the vicinity to the Ringvent mound. Conductivity measurements at Site U1548 show values in the sediment layers that are similar to those at Site U1547. Sites U1547 and U1548 show similar profiles for density, porosity, strength, NGR, MS, and *P*-wave velocity in the upper 90 m of sediment. Petrophysical variations highlight the main lithostratigraphic changes at Site U1548 through correlated variations in density and NGR values. Mafic sill material recovered from Site U1547 shows thick continuous intrusion sheets across the transect of its boreholes, and no bottom contact to the underlying sediment was encountered.

4.4. Site U1549

4.4.1. Background and objectives

Site U1549 (proposed Site GUAYM-16A) is located ~9.5 km northwest of the northern axial graben of Guaymas Basin (Figure F1) and ~780 m northwest of a mound-shaped seafloor feature (Figure F11) where active cold-seep communities were documented by preexpedition site surveys (Teske et al., 2021). In addition, seismic data at this location were interpreted to show an underlying sill at ~450 mbsf and indicate gas movement along and around a pipe structure (Figure F11). This association of a relatively deep sill, active gas venting, and seafloor communities connects multiple components of the carbon budget of a sill-driven vent/seep system. The sedimentary setting at Site U1549 is intermediate between the biogenic-dominated sedimentation observed at Sites U1545 and U1546 and the dominantly terrigenous deposition documented southeast of the northern axial graben (Site U1551). The primary objectives for Site U1549 are thus to characterize the physical, chemical, and microbial properties of this sedimentologically intermediate setting and to assess the influence of the underlying sill and associated altered sediments on carbon cycling in the subseafloor.

4.4.2. Operations

Two holes were cored at Site U1549. Hole U1549A is located at 27°28.3317′N, 111°28.7844′W in a water depth of 1840.1 m. In Hole U1549A, we used the APC system to advance from the seafloor to a final depth of 168.0 mbsf with a recovery of 166.9 m (99%). We made formation temperature measurements at several depths using the APCT-3 tool. In Hole U1549B, located at 27°28.3383 N,

111°28.7927′W in a water depth of 1841.2 m, we deployed the APC system. Cores penetrated from the seafloor to a final depth of 166.9 mbsf and recovered 164.4 m (99%). Hole U1549B was dedicated to extensive microbial and biogeochemical sampling that required the deployment of PFTs downhole for all cores to monitor drilling fluid (seawater) contamination. The pace of coring in Hole U1549B was adjusted to accommodate the complex microbial sampling program conducted on the core receiving platform. A total of 51.1 h, or 2.1 days, were spent at Site U1549. An overview of cores, penetration depths, core recovery, and operations schedule for Site U1549 is given in Table T1.

4.4.3. Principal results

4.4.3.1. Lithostratigraphy

The sediments recovered at Site U1549 are late to middle Pleistocene in age and are mostly biogenic (mainly diatom ooze) with a significant (\sim 10%) proportion of sand- to silt-sized siliciclastic components that occur either mixed with the biogenic component or concentrated in discrete laminae and beds (Figure F12). No major diagenetic changes were observed, probably because of the relatively shallow subseafloor depth reached at this site, leading to the characterization of a single lithostratigraphic unit (Unit I). The most common lithology observed is olive-gray, clay-to silt-rich diatom ooze. Unlike what was observed in the northwestern (Sites U1545 and U1546) and Ringvent (Sites U1547 and U1548) sediment successions, the diatom ooze is primarily nonlaminated. The terrigenous-dominated depositional layers that are intercalated with diatom ooze range from a few centimeters to a meter thick with sharp bases that are locally marked by a coarser basal lamina of silt- to sand-sized bioclasts (foraminifers and small bivalves). The thickest beds occasionally have a base of laminated, bioclastic sand with a few coarse siliciclastic particles. Other coarse siliciclastic (silt- to sand-sized) depositional layers were also recognized, and they range from laminae of a few millimeters thick to beds as thick as ~6 m. The thickest of these beds are normally graded and associated with basal sand to silty sand that shows scouring at the base. Four exceptionally thick, normally graded terrigenous depositional layers were noted in the lithologic succession. Three of these beds were clearly correlated between Holes U1549A and U1549B and

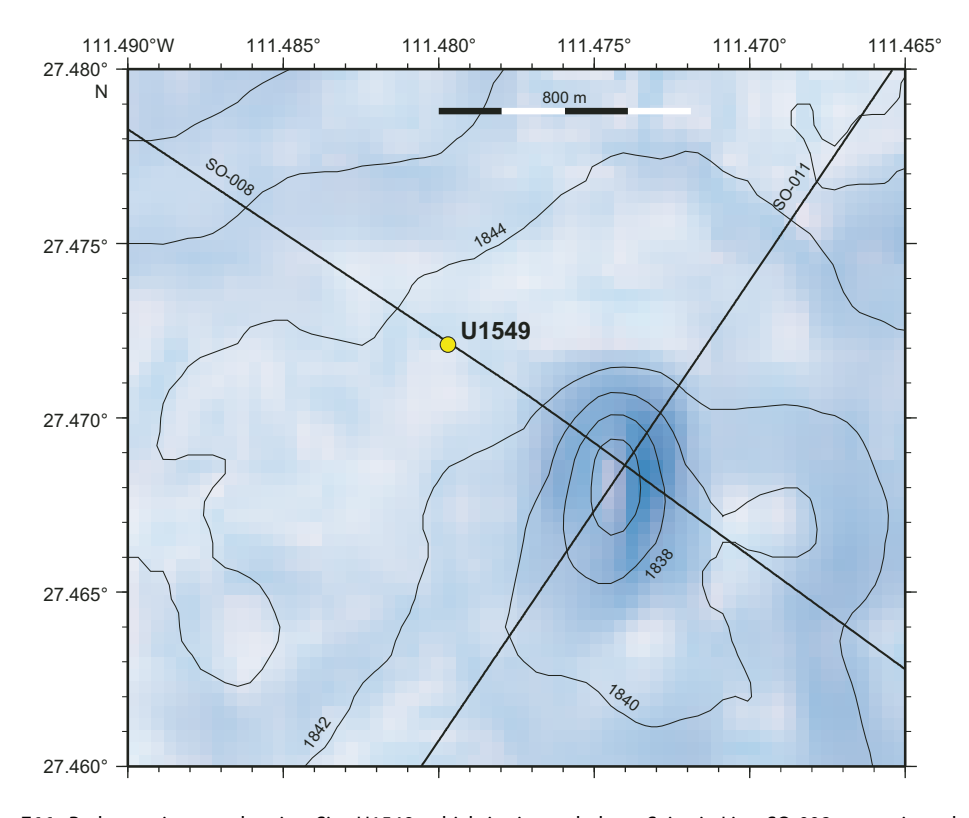


Figure F11. Bathymetric map showing Site U1549, which is situated along Seismic Line SO-008 approximately 700 m northwest of a seafloor mound where cold-seep fauna exists. The locations of drilled holes are not distinguishable at the given scale. Contour lines = 2 m.

show a characteristic increase in NGR, MS, and color parameter b*. The depositional layers composed of homogeneous biogenic and siliciclastic components are interpreted to be the products of slope instability and mass-gravity deposition, including hybrid flows.

4.4.3.2. Structural geology

Structural information was obtained from sedimentary sequences at Site U1549. None of the samples were sufficiently lithified to be measured independently as whole-round pieces. Tilted laminae seen in Cores 385-U1549A-2H and 3H suggest small-scale slump folds, but the rest of Holes U1549A and U1549B mostly have laminae that are roughly perpendicular to the axis of the hole. One chevron fold with a horizontal fold axis was found in interval 385-U1549A-3H-1, 42–47 cm (\sim 16.4–16.5 mbsf). Tilted bedding was noted starting in Section 16H-1 (139.5 mbsf) and continues to deeper levels in Cores 17H and 18H with values typically from 10° to 15°. A few brittle faults were seen at different depths in the section, but overall there is much less faulting in this sedimentary section than at Ringvent Sites U1547 and U1548, northern rift Site U1550, and northwestern Guaymas Basin Sites U1545 and U1546.

4.4.3.3. Biostratigraphy

Calcareous nannofossils are abundant to common with good/moderate preservation throughout the entire sampled sequence at Site U1549, and the barren interval seen at Sites U1545–U1548 is not present at this site. Reworked nannofossils include a significant component of Miocene taxa with a greatly reduced contribution of reworked Cretaceous specimens. In general, marine diatoms are dominant to abundant with good/moderate preservation throughout Hole U1549A, except at 63.62 and 71.23 mbsf, where diatoms have a common abundance. Freshwater diatoms in Hole U1549A are much more frequent than at the northwestern and Ringvent sites, particularly at similar depths. This suggests strong influence of terrestrial input. No evidence of diagenetic alteration of diatoms is present in Hole U1549A. The occurrence of *E. huxleyi* from the top to the bottom of the hole dates the entire sediment sequence to (Holocene–)late–middle Pleistocene, or younger than 0.29 Ma (Hole U1549A = 0–168.35 mbsf). This age assignment is consistent with the absence of *P. lacunosa* (LAD = 0.44 Ma) and *F. reinholdii* (LAD = 0.62 Ma) in all examined samples. The estimated average sedimentation rate is >580 m/My (>58.0 cm/ky).

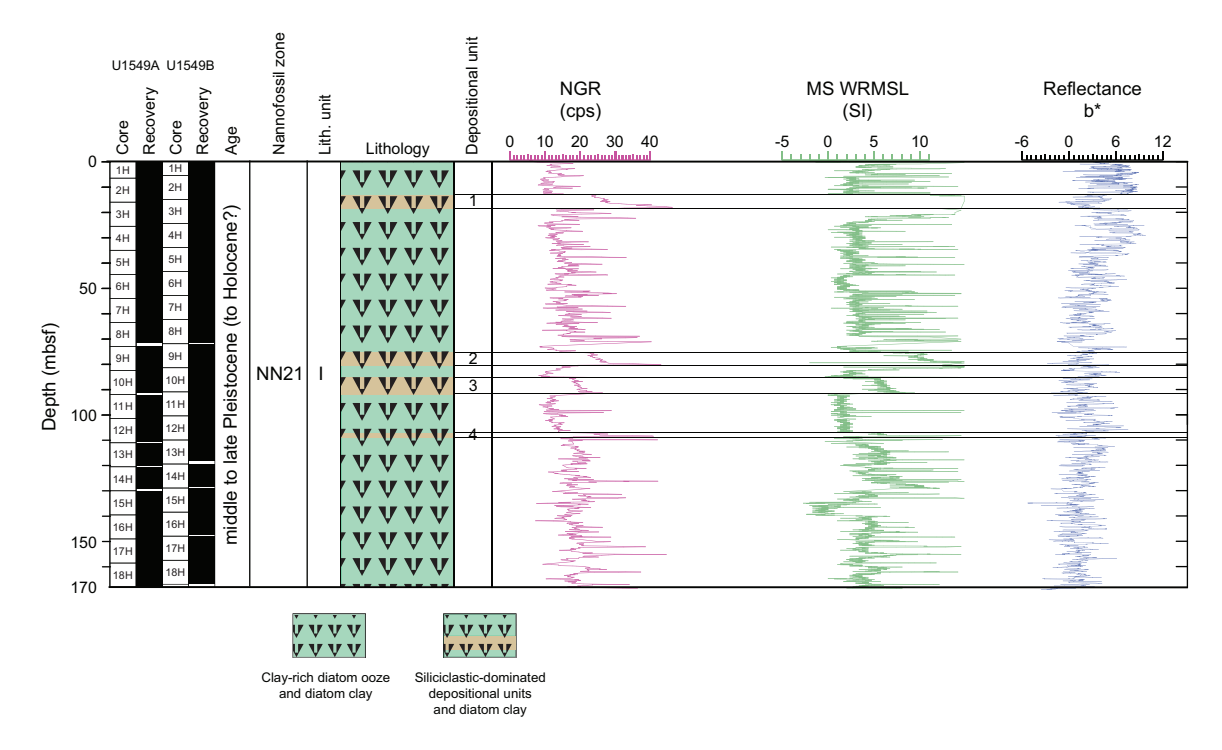


Figure F12. Lithostratigraphic column, Site U1549. The natural gamma radiation (NGR), magnetic susceptibility (MS), and color reflectance b* (all from Hole U1549A) support a single-unit interpretation but highlight the characteristics of the four thick terrigenous units (1–4). cps = counts per second, WRMSL = Whole-Round Multisensor Logger.

4.4.3.4. Paleomagnetism

AF demagnetization up to 20 mT was performed on archive-half sections with the SRM on all APC sediment cores from Hole U1549A. The drilling-induced overprint was successfully removed from all cores (from the seafloor to \sim 168 mbsf) upon demagnetization. Inclination values after demagnetization at 20 mT cluster around 46°, which corresponds to the expected GAD inclination at the latitude of the site (46.1°). A detailed analysis of the remanence of discrete samples from Hole U1549A shows that the drilling-induced overprint is removed by 10 mT and the ChRM is in accordance with the SRM measurements. The NRM of archive-half sections is higher at \sim 16–19, \sim 69.5–70, and 79.5–80 mbsf. These intervals correspond to sandy layers that contain more detrital material. Hole U1549A cores were assigned to the normal Brunhes Chron C1n (younger than 0.78 Ma). The AMS obtained from Hole U1549A sediments is characterized by a mixture of prolate and oblate behavior. No paleomagnetic measurements were carried out in Hole U1549B.

4.4.3.5. Inorganic geochemistry

To examine biogeochemical profiles associated with microbial diagenesis in greater resolution, the total of 65 IW samples that were collected by hydraulic pressing of sedimentary whole-round core samples (35 from the seafloor to 160 mbsf) were supplemented by Rhizon sampling of freshly recovered core sections spaced at approximately 1 m intervals (30 from the seafloor to 30 mbsf in Hole U1549A). Based on the sulfate profiles, the SMTZ is estimated at 30 mbsf in Hole U1549A and 25 mbsf in Hole U1549B, considerably shallower compared to Sites U1545 and U1546. Below the SMTZ around 100 mbsf, alkalinity reaches a high maximum value of 85 mM and ammonium reaches maximum concentrations near 15 mM. Mg²+ has a higher concentration than seawater (53.5 mM), and its maximum value reaches 65 mM below the SMTZ. In addition, downhole concentration profiles of Li+, B, and H₄SiO₄ generally display an increasing trend with higher values than those of seawater. The IW chemical signatures at Site U1549 may be predominantly influenced by organic matter degradation related to microbial processes and by sediment-water interactions and mineral precipitation/dissolution processes.

4.4.3.6. Organic geochemistry

At Site U1549, organic geochemists performed sampling and analysis of gas and solid-phase samples. In Hole U1549A, one headspace gas sample was analyzed per 9.5 m advance for routine hydrocarbon safety monitoring, void gases were quantified and sampled for hydrocarbon content, and the carbon, nitrogen, and sulfur contents of particulate sediment were characterized. In Hole U1549B, hydrocarbon analyses were performed on headspace gas; H_2 and CO contents were measured; sediment carbon, nitrogen, and sulfur contents were characterized; and a comprehensive suite of gas and sediment samples was taken for postexpedition analyses. Methane appears below ~25 mbsf, and C_2 – C_6 hydrocarbons are all detectable at depths below 60 mbsf. No anomalous C_1/C_2 values were observed. From elemental analysis, we inferred that the primary source of organic matter is marine in origin. In Hole U1549B, H_2 and CO are present in low concentrations, which suggests that biological cycling is the dominant control on these gases.

4.4.3.7. Microbiology

Hole U1549B samples represent horizons that inform our understanding of the cycle of carbon driven by fluid flow in the Guaymas Basin subseafloor. Site U1549 is effectively a cold-seep site characterized by mass-gravity flows. Thus, the site has a relatively high proportion of terrigenous material and an attenuated thermal gradient that indicates relatively moderate hydrothermal warming. As such, it provides an opportunity for microbiologists to examine the influence of these gravity flows on in situ microbial diversity and on activities within a hydrothermal setting distal to the immediate influences of emplaced sills and/or extremely hot hydrothermal fluids. Syringe samples for cell counts, 3-D structural imaging, and RNA analyses were taken on the core receiving platform, preserved or frozen, and stored for further analyses. Whole-round core samples were either stored in a -80° C freezer or temporarily stored in a $4^{\circ}-8^{\circ}$ C cold room and processed further for shore-based analyses, as described for Site U1545. Samples for PFT measurements were taken on the core receiving platform using a syringe at six distinct horizons. Cell abundance for selected samples was determined by direct counting with an epifluorescence microscope. Cell abundance was 0.94×10^{6} cells/cm³ in bottom seawater and 6.3×10^{8} cells/cm³ in seafloor sediments. Cell abundance gradually decreased to below the detection limit of the protocol used for

shipboard measurements at approximately 124 mbsf, twice as deep as at Ringvent (Holes U1547B, U1548A, and U1548C).

4.4.3.8. Petrophysics

Physical properties measured on whole-round and working-half sections from Holes U1549A and U1549B were compared for lithostratigraphic characterization and correlation of visual core description with physical properties. Four in situ formation temperature measurements were taken with the APCT-3 tool to calculate the geothermal gradient (194°C/km) and heat flow (144 mW/m²). Conductivity measurements show a similar trend with depth in Holes U1549A and U1549B. We have identified one main interval that correlates with Lithostratigraphic Unit I. NGR and MS peaks at ~70–100 mbsf correlate with four depositional subunits. These physical properties along with density and P-wave velocity values have a negative correlation with porosity values. Thus, porosity values derived from MAD measurements show a general decrease with depth. In contrast, shear strength measurements show a linear increase due to the presence of indurated sediments at depth.

4.5. Site U1550

4.5.1. Background and objectives

Site U1550 (proposed Site GUAYM-06B) is located within the axial graben of the northern Guaymas Basin spreading segment (Figures F1, F13). This site was established very close to DSDP Site 481 to take advantage of the known presence, depth, and characteristics of sills and indurated sediments at Site 481 (Shipboard Scientific Party, 1982), and to clarify its stratigraphy by redrilling it with improved coring tools and sampling approaches. Substantially improved recovery was expected relative to Site 481, leading to increased sampling resolution of downhole changes and enabling the use of modern microbiological approaches. The fault-bounded setting of Site U1550 provides the potential for high-flux fluid circulation in response to sill intrusion, leading to swift cooling and potentially enhanced alteration due to the rapid removal of dissolved phases and gases. The primary objectives for Site U1550 are to characterize the physical, chemical, and microbial responses to sill intrusion into sediments at a high-flux end-member location.

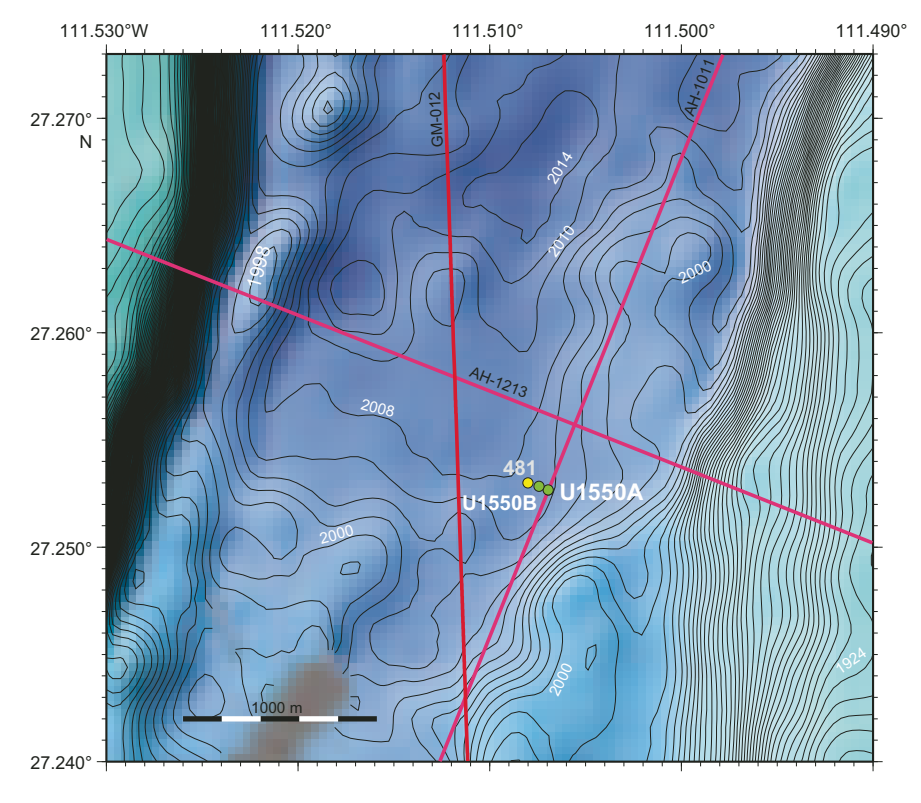


Figure F13. Bathymetric map, Site U1550. DSDP Site 481 is also shown. Contour lines = 2 m.

4.5.2. Operations

We cored two holes at Site U1550. Hole U1550A is located at 27°15.1602N, 111°30.4163′W in a water depth of 2000.8 m. In Hole U1550A, we used the APC, HLAPC, and XCB systems to advance from the seafloor to a final depth of 207.0 mbsf with a recovery of 190.9 m (92%). We made formation temperature measurements at several depths with the APCT-3 and SET2 tools. In Hole U1550B, located at 27°15.1704′N, 111°30.4451′W in a water depth of 2001.2 m, we deployed the APC, HLAPC, and XCB systems. Cores penetrated from the seafloor to a final depth of 174.2 mbsf and recovered 160.8 m (92%). Hole U1550B was dedicated to extensive microbial and biogeochemical sampling that required the deployment of PFTs downhole on all cores to monitor drilling fluid (seawater) contamination. The pace of coring in Hole U1550B was adjusted to accommodate the complex microbial sampling program conducted on the core receiving platform. A total of 72.0 h, or 3.0 days, were spent at Site U1550. Table T1 provides an overview of cores, penetration depths, core recovery, and operations schedule for Site U1550.

4.5.3. Principal results

4.5.3.1. Lithostratigraphy

At Site U1550, a succession of sediments, sedimentary rocks, and igneous rocks was recovered (Figure F14). The sedimentary material recovered can mainly be ascribed to two lithologic types: (1) a biogenic-dominated type, in which more or less laminated olive-gray diatom clays occur mixed with various proportions of nannofossils and silt-sized siliciclastic particles, or (2) a siliciclastic-dominated type in which coarse-grained siliciclastic components (sand and silt), clay minerals, and subordinate diatoms occur either mixed in homogeneous layers or segregated in depositional layers often characterized by graded beds and scoured bases. Most of the thickest graded terrigenous layers identified are traced between holes. Vertical changes in the character of the dominant lithology, the style of bedding and/or deformation, and the diagenetic boundaries prompted the subdivision of Unit I into three subunits. Subunit IA includes three thick terrigenous beds and displays evidence of soft-sediment deformation. The lower part of the subunit in both holes is marked by a lithologically complex but correlative interval that includes a large con-

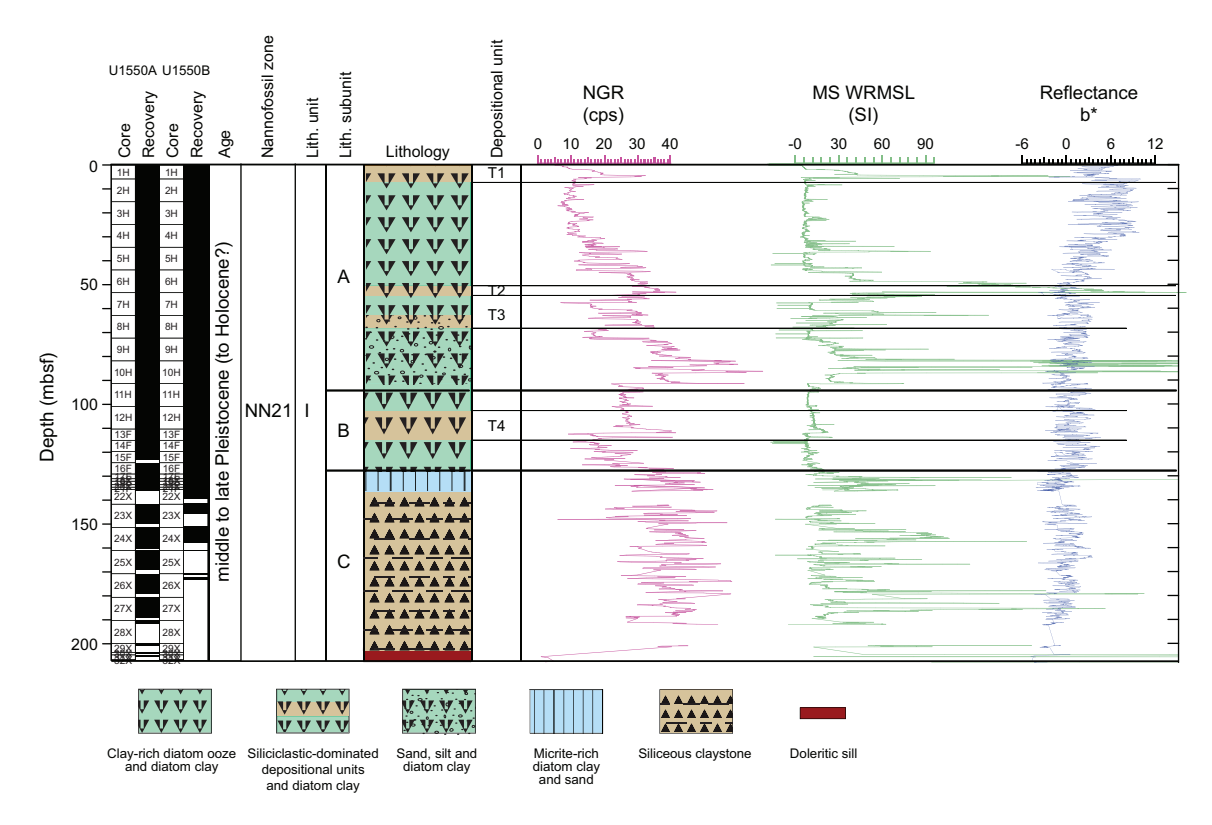


Figure F14. Lithostratigraphic column, Site U1550. Lithostratigraphic and physical property data are derived from Hole U1550A. NGR = natural gamma radiation, cps = counts per second, MS = magnetic susceptibility, WRMSL = Whole-Round Multisensor Logger.

centration of silt- to granule-sized scoria fragments. Subunit IB is mainly composed of varying proportions of diatoms, clay, and silt, with sand occurring as a minor component. The upper part of the subunit contains a very distinctive, ~18 m thick, homogeneous interval composed of olivegreen diatom clay. There are pronounced differences in Subunit IC between holes. In Hole U1550A, the top of this subunit corresponds to the first appearance of carbonates (micrite/nodules). The latter occur scattered in diatom clay or as cementing crystals in coarser grained (sand to silt) lithologies. Folding and tilting are common as well as the presence of coarser grained beds, including a fourth thick terrigenous bed (Figure F14). Low diatom abundance and preservation support the XRD analysis interpretation that the sediments have undergone silica diagenesis and the transition from opal-A to opal-CT. In Hole U1550B, Subunit IC was identified in only three cores that are mainly composed of organic-rich, yellowish brown homogeneous diatom clay with evidence of soft-sediment deformation. The sediments recovered at Site U1550 display a variety of sedimentary features, including graded beds with scoured bases ranging from a few centimeters to several meters thick, tilted and/or folded beds or laminae, and chaotic fabric. Taken together, these features are direct evidence that deposition at this site occurred mainly by means of mass-gravity flow events.

4.5.3.2. Igneous petrology and alteration

The dominant hypabyssal igneous lithology recovered from the bottom of both Hole U1550A (upper contact at ~204 mbsf with ~1.2 m recovered) and Hole U1550B (upper contact at ~170 mbsf with ~1.6 m recovered) is mafic rock with a largely doleritic texture. Minor basaltic rock intervals with a sparsely to highly plagioclase-phyric texture occasionally occur. Notably, there is a gradual change in grain size transitioning from basaltic to doleritic texture within a distance of a few centimeters, indicating slow magma solidification. Nevertheless, there are also angular fragments of doleritic material entrapped in basaltic rock intervals in Hole U1550B. The slightly to moderately altered igneous rocks are nonvesicular to sparsely vesicular and contain multiple, slightly dipping calcite veinlets running parallel to each other. Samples obtained from this sill show a subalkaline, tholeiitic mafic rock chemistry that corresponds to an enriched MORB composition. These rocks appear to represent somewhat more evolved melts based on their lower Mg# compared to the sill material recovered from nearby DSDP Site 481.

4.5.3.3. Structural geology

Both Holes U1550A and U1550B exhibit folding and tilted bedding starting at 15 mbsf and continuing intermittently below. These displacements are attributed to soft-sediment deformation and slumping because they are variable on a small spatial scale. Significant faults are seen in both holes at about 130–140 mbsf, where sets of parallel faults with apparent dips of about 60° displace the sediment. These faults have a spacing of 0.2–1 m in the cores, but the amount and direction of displacement is unknown. The faults indicate an episode of deformation that occurred prior to the time of deposition of sediments that are now found at about 130 mbsf.

4.5.3.4. Biostratigraphy

Calcareous nannofossils are abundant and common to 123.08 mbsf, rare/barren from 131.06 to 135.6 mbsf, and resume abundant and common occurrences from 142.02 to 187.66 mbsf. Nannofossil preservation is good/moderate throughout the entire sedimentary sequence. Marine diatoms are dominant to abundant with good/moderate preservation in the upper interval of Hole U1550A (0–72.51 mbsf). They alternate between abundant, common, and few with moderate to poor preservation at an intermediate depth range (81.02–123.08 mbsf), and range from few to rare and barren with poor preservation in the lowermost interval (131.06–200.55 mbsf). Apparent diagenetic alteration of diatoms is present in samples with rare diatoms at the bottom of Hole U1550A. The diatom assemblages are obviously different from Sites U1545, U1546, U1547, and U1548, possibly suggesting strong disturbance of sedimentation sequences by underwater massflow events. The occurrence of calcareous nannofossil *E. huxleyi* from the top to the bottom of both holes dates the entire sediment sequence to (Holocene–)late–middle Pleistocene, or younger than 0.29 Ma (Hole U1550A = 0–200.55 mbsf). This age assignment is consistent with the absence of *P. lacunosa* (LAD = 0.44 Ma) and *F. reinholdii* (LAD = 0.62 Ma) in all samples examined. The estimated average sedimentation rate is >692 m/My (>69.2 cm/ky).

4.5.3.5. Paleomagnetism

AF demagnetization up to 20 mT was carried out with the SRM on archive-half sections on all sediment cores from Hole U1550A (Cores 1H–29X). The drilling-induced overprint was successfully removed from APC and HLAPC cores (from the seafloor to ~130 mbsf) upon demagnetization. Inclination values after demagnetization at 20 mT cluster around 46°, which is comparable to the expected GAD inclination at the latitude of the site (45.9°). A detailed analysis of the remanence of discrete samples from Hole U1550A shows that the drilling-induced overprint was removed by 10 mT, and the ChRM agrees with the SRM measurements. Unfortunately, XCB cores were overprinted and too disturbed to yield reliable paleomagnetic data. Nevertheless, three discrete samples were collected in XCB cores and their inclination values are consistent with what is expected. Thus, Hole U1550A cores were assigned to the normal Brunhes Chron C1n (younger than 0.78 Ma). Discrete sedimentary samples taken in Hole U1550A predominantly show prolate behavior throughout the hole with the $K_{\rm max}$ principal axis of AMS distributed in the horizontal plane. The archive-half sections containing igneous rocks (Cores 385-U1550A-30X through 32X and Cores 385-U1550B-22X through 23X) were only measured for their NRM because AF demagnetization treatment was not effective.

4.5.3.6. Inorganic geochemistry

A total of 42 IW samples were collected from the sedimentary succession at Site U1550. The SMTZ at this site is located at ~10 mbsf, one of the shallowest SMTZs encountered during this expedition. The IW chemical properties show spatial and vertical heterogeneities, exhibiting differences between Holes U1550A and U1550B (e.g., alkalinity, ammonium, Mg^{2+} , Li^+ , and B) and changing significantly between the upper and lower parts of the sediment succession throughout both holes. In the upper part of Site U1550 (0–40 mbsf), alkalinity reaches very high values up to 90 mM, and Mg^{2+} accumulates to values higher than seawater concentration, whereas Ca^{2+} shows a decreasing trend due to authigenic carbonate precipitation. Ammonium shows local peaks at 25 mbsf and around 100 mbsf, with the upper peak stronger in Hole U1550A and the deeper one stronger in Hole U1550B. Below 100 mbsf, alkalinity and Mg^{2+} decrease with depth, and Ca^{2+} , Li^+ , Sr^{2+} , and H_4SiO_4 concentrations increase with depth. These elements show remarkable excursions above the sill. Thus, the IW chemical properties in this interval are likely to be influenced by the sill, as previously evidenced at DSDP Site 481 (Shipboard Scientific Party, 1982).

4.5.3.7. Organic geochemistry

At Site U1550, organic geochemists performed sampling and analysis of gas and solid-phase samples and examined them for features that might distinguish this axial setting. In Hole U1550A, one headspace gas sample was analyzed per 9.5 m advance for routine hydrocarbon safety monitoring; void gases were quantified and sampled for hydrocarbon, H_2 , and CO contents; and the carbon, nitrogen, and sulfur contents of particulate sediment were characterized. In Hole U1550B, hydrocarbon, H_2 , and CO analyses were performed on headspace and void gas samples. Carbon, nitrogen, and sulfur contents of sediment were characterized, and a comprehensive suite of gas and sediment samples for postexpedition analyses were taken. Methane and C_2 – C_6 hydrocarbons are detectable at depths below ~7 mbsf. Low C_1/C_2 values that displayed an anomalous relationship with temperature were observed in both Holes U1550A and U1550B. The lowest ratios occurred between ~100 and ~130 mbsf, but the concentrations of higher hydrocarbon were low and C_1/C_2 values returned to normal farther downhole. From elemental analysis, we infer that the primary source of organic matter is marine in origin, although some samples indicate terrestrial organic matter input, and others are ambiguous because of the influence of mineral-associated nitrogen. In Hole U1550B, H_2 and CO are present at nanomolar concentrations.

4.5.3.8. Microbiology

Hole U1550B is located \sim 50 m southeast of DSDP Site 481 where past studies included enrichments for hydrogenotrophic methanogens and detected living methanogens in shallow cores (Oremland et al., 1982). Consistent with previously measured moderate temperatures at Site 481 (Shipboard Scientific Party, 1982), this hole presents an opportunity for microbiologists to examine the microbial abundance and community structure in sediments with a lower temperature gradient compared to the other sites of Expedition 385. Syringe samples for cell counts, 3-D structural imaging, and RNA analyses were taken on the core receiving platform, preserved or frozen, and stored for further analyses. Whole-round core samples were either stored in a -80° C freezer or

temporarily stored in a cold room of 4°–8°C and processed further for shore-based analyses, as described for Site U1545. Samples for PFT measurements were taken on the core receiving platform by syringe at nine distinct horizons. Cell abundance for selected samples was determined by direct counting with an epifluorescence microscope. Cell abundance was 3.1×10^6 cells/cm³ in bottom seawater, whereas seafloor sediments showed 1.1×10^9 cells/cm³. Below the seafloor, cell abundance gradually decreased to 1.3×10^6 cells/cm³ at 94.5 mbsf and decreased below the detection limit of the protocol used for shipboard measurements at approximately 122 mbsf, which was nearly twice as deep as at Ringvent (Holes U1547B, U1548B, and U1548C).

4.5.3.9. Petrophysics

Measurements of physical properties made on whole-round and working-half core sections were compared between Holes U1550A and U1550B for lithostratigraphic characterization and correlation of visual core description with physical properties. Four in situ formation temperature measurements were conducted using the APCT-3 and SET2 tools to calculate the geothermal gradient (135°C/km) and heat flow (110 mW/m²). Conductivity measurements between Holes U1550A and U1550B show a similar increasing trend with depth. Three main depth intervals are characterized by notable petrophysical strength variations between the seafloor and 43 mbsf, from 43 to 86.5 mbsf, and below 96.5 mbsf, showing significant increases in shear strength. These features are embedded in a rheology trend of generally increasing shear strength downhole whereas porosity strongly decreases because of the presence of a sill at the bottom of both holes. Strength and porosity measurements correlate positively with three lithologic subunits (IA-IC) and negatively with the rest of the physical properties (e.g., bulk density). Physical properties in Holes U1550A and U1550B show good correlation with depth except at ~80-90 mbsf where the peaks of NGR, MS, and P-wave velocity show an offset of 10 m between the two holes (at ~80 mbsf in Hole U1550A and ~90 mbsf in Hole U1550B). Also, these physical properties reveal the presence of a sill in both holes (top contact at \sim 204 mbsf in Hole U1550A and \sim 170 mbsf in Hole U1550B).

4.6. Site U1551

4.6.1. Background and objectives

Site U1551 (proposed Site GUAYM-15A) is located ~29 km southeast of the axial graben of the northern Guaymas Basin spreading segment (Figures F1, F15). The type of sediment, the depositional environment, and the type, size, and, presumably, age of sill intrusions were all proposed to differ in the southeastern side of the spreading segment relative to the northwestern side (Teske et al., 2018). The sediment at Site U1551 was predicted to be predominantly terrigenous and deposited as gravity-driven flows ranging from landslides to turbidites, with the underlying sills appearing to be larger and more saucer-shaped than those in the northwest. It was hypothesized that the physical and chemical properties of sediments may impact alteration in response to sill intrusion, and this may have consequences for carbon cycling. Moreover, the physical properties of the sediments may influence the size and shape of the sills beneath Site U1551. In turn, permeability might evolve toward enhanced induration, ultimately affecting the efficiency of alteration. Terrestrial organic carbon and metals are predicted to be more abundant in these sediments relative to the northwestern part of the basin, and this may also affect sediment alteration and its products. The primary scientific objective at Site U1551 was to constrain the influence of sediment type, an important factor controlling alteration and carbon cycling, on sill morphology by studying the response of predominantly terrigenous sediments to sill intrusion.

4.6.2. Operations

Two holes were cored at Site U1551. Hole U1551A is located at 27°12.3887′N, 111°13.1943′W in a water depth of 1844.1 m. In Hole U1551A, we used the APC and HLAPC systems to advance from the seafloor to a final depth of 120.3 mbsf with a recovery of 122.1 m (102%). We made formation temperature measurements at several depths using the APCT-3 tool. Coring was terminated because unconsolidated sand layers prevented us from reaching the deeper drilling objectives. In Hole U1551B, located at 27°12.3832′N, 111°13.1841′W in a water depth of 1843.9 m, we deployed the APC system. Cores penetrated from the seafloor to a final depth of 48.5 mbsf and recovered 50.0 m (103%). Hole U1551B was dedicated to extensive microbial and biogeochemical sampling that required the deployment of PFTs downhole on all cores to monitor drilling fluid (seawater)

contamination. The pace of coring in Hole U1551B was at times adjusted to accommodate the complex microbial sampling program conducted on the core receiving platform. A total of 34.3 h, or 1.4 days, were spent at Site U1551. Its cores, penetration depths, core recovery, and operations schedule are displayed in Table **T1**.

4.6.3. Principal results

4.6.3.1. Lithostratigraphy

The sediments recovered at Site U1551 are assigned to Lithostratigraphic Unit I. They represent a combination of biogenic (diatom ooze to diatom clay) and terrigenous (sand/silt/clay grade) components with the highest overall proportion of silty to sandy intervals (~60%) cored during Expedition 385 (Figure F16). Macroscopic core description and microscopic smear slide analysis show that two main types of lithologic components are clustered in four different stratigraphic intervals. These lithologic patterns are reflected in the NGR, MS, and color reflectance data, forming the basis of the division of Unit I into four subunits, with Subunits IA and IC dominated by biogenic sedimentation and Subunits IB and ID appearing more siliciclastic in character. Lithologies in which the content of diatoms is very high (>85%) are mainly found in Subunit IA. The underlying Subunit IB includes authigenic carbonates that occur in small patches of micrite, partly cemented sandstone intervals, or carbonate concretions. This subunit also contains thick sand beds, and overall, it is dominated by coarser grained siliciclastic sediments that correspond to higher MS and NGR values. Subunit IC is composed of silt-rich diatom clay and clay-rich, mainly homogeneous, diatom ooze alternating with beds of gray sand and silty sand. Subunit ID is mainly composed of medium-grained sand, which is partially interpreted to represent coring-induced flow-in rather than in situ deposition. Although Site U1551 and Site U1549 share many lithostratigraphic similarities, the former contains larger proportions of siliciclastic material. The predominance of siliciclastic components over biogenic ones and the presence of coarse-grained mass-gravity flow deposits suggest that the deposition at this site was more influenced by terrigenous sources than at

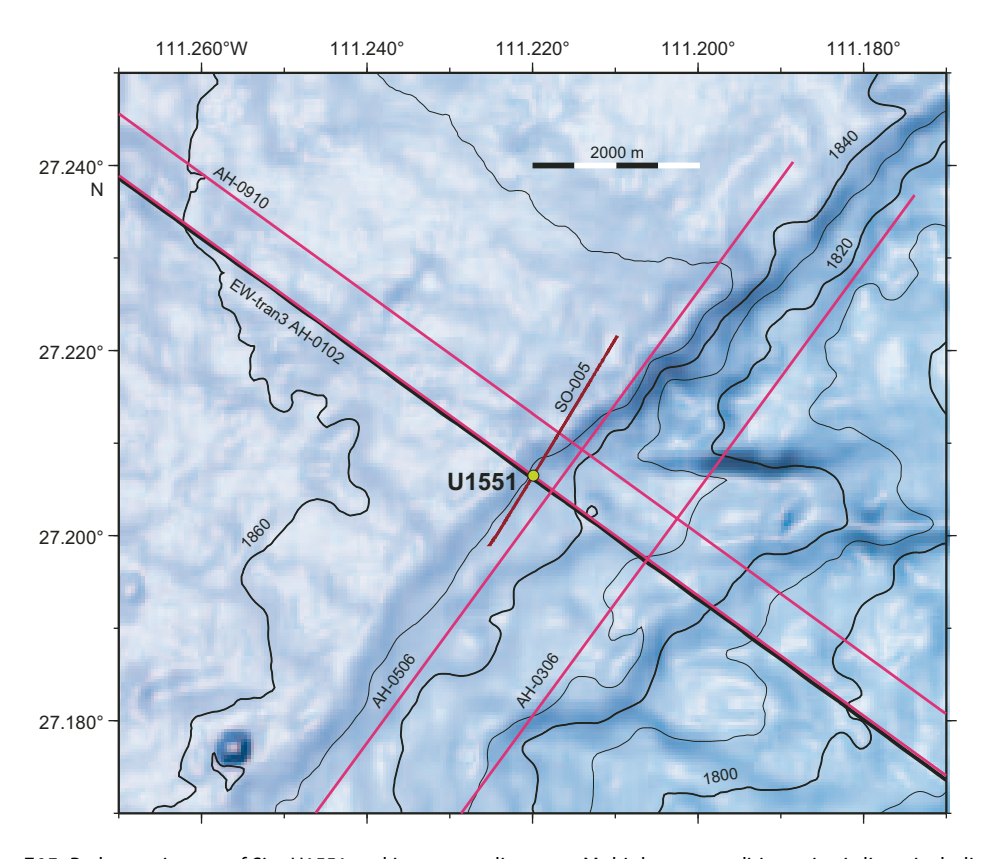


Figure F15. Bathymetric map of Site U1551 and its surrounding area. Multiple preexpedition seismic lines, including EW-tran3, are also shown. The seafloor bathymetry reflects the mode of predominant mass-gravity sediment deposition. Site U1551 is sited at the edge of a large slide deposit that is imaged in the seismic data. The locations of drilled holes are not distinguishable at the given scale. Contour lines = 10 m.

the other sites drilled in Guaymas Basin during Expedition 385. This may be related to the more proximal location of Site U1551 to the Yaqui River delta.

4.6.3.2. Structural geology

At Site U1551, Holes U1551A and U1551B penetrated Lithostratigraphic Unit I, recovering a sedimentary sequence of diatom ooze, diatom clay, sand, and silt. Bedding and lamination in the sedimentary succession are similar to those described for Sites U1545–U1550. However, Site U1551 has intervals of massive sand layers in which the lack of stratification prevented any deformation structures from being identified. Folds are seen in Subunit IB in both holes, where contortion and soft-sediment deformation produced steep to overturned bedding below ~ 15 mbsf. The folded strata are cut by a single set of faults with subparallel orientations and apparent dips of 45° – 70° . Faults were found in some deeper intervals. The differences in depths characterizing the folded strata in Holes U1551A and U1551B may have been partly caused by faulting prior to the deposition of Subunit IA. No faulting is inferred in Subunit IA at Site U1551, based on the stratigraphic similarity between the two drill holes.

4.6.3.3. Biostratigraphy

In Hole U1551A, calcareous nannofossils are abundant to rare to 96.8 mbsf with two barren intervals around 24.8 and 25.1 mbsf. Farther downhole, nannofossils are barren in the interval 102.14-116.19 mbsf and abundant in the bottom sample from 119.01 mbsf. Nannofossil preservation is good and moderate throughout the entire sedimentary sequence except for two samples with poor preservation at 22.0 and 25.8 mbsf. The barren intervals correspond to recovered sections of predominantly sandy lithology. Marine diatoms are abundant with good preservation only in the uppermost part of Site U1551. Then, they decrease in abundance with moderate to poor preservation from the seafloor to 36.9 mbsf, followed by an interval without diatoms from 36.9 to 61.22 mbsf. Diatoms vary from common to rare with moderate to poor preservation from 71 to 108.28 mbsf, and they are barren at the bottom of Hole U1551A. Diatoms are abundant but poorly preserved in a spot sample from 119.0 mbsf at the bottom of Hole U1551A. The occurrence of E. huxleyi from the seafloor to the bottom of Hole U1551A dates the entire sediment sequence to (Holocene-)late-middle Pleistocene, or younger than 0.29 Ma (Hole U1551A = 0-119.01 mbsf). This age assignment is consistent with the absence of *P. lacunosa* (LAD = 0.44 Ma) and *F. reinhol*dii (LAD = 0.62 Ma) in all examined samples. The estimated average sedimentation rate is >410.4 m/My (>41.04 cm/ky).

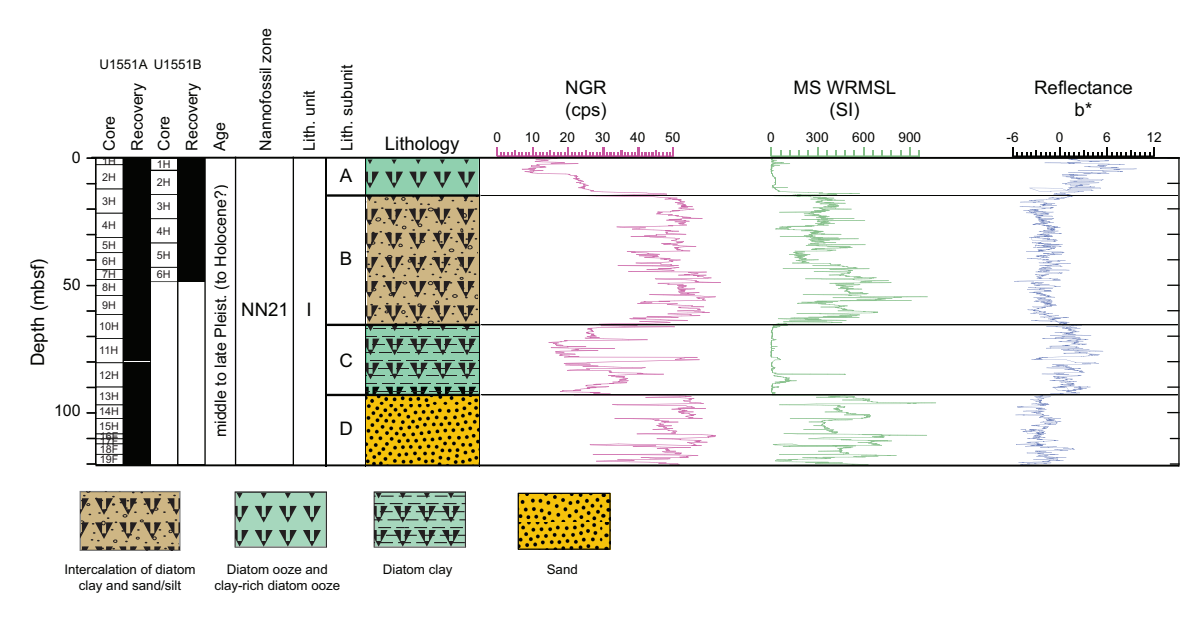


Figure F16. Lithostratigraphic column, Site U1551. NGR = natural gamma radiation, cps = counts per second, MS = magnetic susceptibility, WRMSL = Whole-Round Multisensor Logger.

4.6.3.4. Paleomagnetism

AF demagnetization up to 20 mT was carried out with the SRM on all sediment archive-half core sections from Hole U1551A (Cores 1H–19F). The drilling-induced overprint was successfully removed from APC and HLAPC cores (from the seafloor to ~120 mbsf) upon demagnetization. Inclination values after demagnetization at 20 mT cluster around 47°, which is comparable to the expected GAD inclination at the latitude of the site (45.8°). A detailed analysis of the remanence of discrete samples from Hole U1551A shows that the drilling-induced overprint is removed by 10 mT, and the ChRM is in accordance with the SRM measurements. Thus, Hole U1551A cores were assigned to the normal Brunhes Chron C1n (younger than 0.78 Ma). Sedimentary discrete samples taken in Hole U1551A predominantly show prolate behavior throughout the hole, with the $K_{\rm max}$ principal axis of AMS distributed in the horizontal plane. No paleomagnetic measurements were implemented in Hole U1551B.

4.6.3.5. Inorganic geochemistry

In Holes U1551A and U1551B, a total of 18 IW samples were taken from all sediment lithologies except for unconsolidated sands. It has been challenging to decipher the IW properties because of the limited number of collected IW samples as a consequence of the abundance of sand. However, as demonstrated by the nearly complete sulfate depletion that coincides with a concentration peak for dissolved sulfide, the SMTZ is located at $\sim\!25$ mbsf. Concentration maxima for alkalinity (around 32 mM) at the SMTZ and for ammonium (6 mM) below the SMTZ around 35–40 mbsf are the lowest found during this expedition with the exception of those within Ringvent. These low concentrations suggest decreased microbal organic matter remineralization in terrestrially impacted sediments. Authigenic carbonate precipitation was observed visually, and the precipitation depth coincides with a sharp decrease in Ca²+ concentrations.

4.6.3.6. Organic geochemistry

At Site U1551, organic geochemists sampled and analyzed gas and solid-phase samples to examine whether the terrigenous influence at this site generates specific organic geochemical signatures. In Hole U1551A, one headspace gas sample was analyzed per 9.5 m advance for routine hydrocarbon safety monitoring, and the carbon, nitrogen, and sulfur contents of particulate sediment were characterized. In Hole U1551B, hydrocarbon analyses on headspace gas were performed at high resolution (two per 9.5 m of core), H_2 and CO contents were measured, and carbon, nitrogen, and sulfur contents of sediment were characterized. Hydrocarbon gases are detectable below ~30 mbsf and are primarily composed of methane and ethane. C_3 – C_6 hydrocarbons were detected in only a few intervals at very low concentrations. Gas concentration with depth is strongly influenced by the presence of sand. From elemental analysis, we infer that the primary source of organic matter in organic-rich intervals is marine in origin. The presence of mineral nitrogen in the organic-poor levels prevents interpreting the C/N values in terms of organic source. H_2 and CO are present at nanomolar concentration levels and exhibit no trend with depth.

4.6.3.7. Microbiology

Site U1551 is located on the southeastern flanking region of Guaymas Basin in an area of low heat flow and is influenced by terrigenous sedimentation derived from the Yaqui River, which drains the Sierra Madre Occidental and coastal Sonora. Consequently, this site presents an opportunity for microbiologists to examine microbial abundance and community structure in terrestrial organic carbon-enriched sediments with more moderate temperature gradients compared to the other sites drilled during Expedition 385. Syringe samples for cell counts, 3-D structural imaging, and RNA analyses were taken on the core receiving platform, preserved or frozen, and stored for further analyses. Whole-round core samples were either stored in a -80°C freezer or temporarily stored in a 4°-8°C cold room and processed further for shore-based analyses, as described for Site U1545. Samples for PFT measurements were taken on the core receiving platform by syringe at five distinct horizons. Cell abundance for selected samples was determined by direct counting with an epifluorescence microscope. Cell abundance was 1.1×10^6 cells/cm³ in bottom seawater and 0.9 × 10° cells/cm³ in seafloor sediments. Below the seafloor, cell abundance gradually decreased to 6.9×10^6 cells/cm³ at approximately 39 mbsf but remained above the detection limit of the protocol that we used for shipboard measurements at this deepest sampling depth in Hole U1551B.

4.6.3.8. Petrophysics

Physical properties at Site U1551 were measured on whole-round and working-half sections. Two holes were cored: Hole U1551A to \sim 120 mbsf and Hole U1551B to \sim 49 mbsf. The acquired data were compared between holes for lithostratigraphic characterization and correlation of core description information with the physical properties data. Four in situ formation temperature measurements were made with the APCT-3 tool to calculate geothermal gradient (\sim 100°C/km) and heat flow (\sim 108 mW/m²). All petrophysical parameters consistently identify four distinct depth intervals that correspond to alternation of diatom ooze and silty sand-dominated lithology: from the seafloor to 15 mbsf, between \sim 15 and \sim 65 mbsf, from \sim 67 to 92 mbsf, and below 92 mbsf. Shear strength consistently increases with depth, coinciding with higher values in compressive strength. Porosity and density values derived from MAD measurements show a strong negative correlation at all depths. The other measured physical properties (density, NGR, MS, and *P*-wave velocity) show a positive correlation with depth that is in accordance with the corresponding presence of diatom ooze, clay, and sand beds.

4.7. Site U1552

4.7.1. Background and objectives

Site U1552 (proposed Site GUAYM-10B) is located ~20 km northwest of the northern axial graben in Guaymas Basin (Figure F17), proximal to the Sonora margin (Figure F1). The site is adjacent to a mostly buried mound that sits atop a pipe-like, acoustically blanked zone that was observed in Seismic Line SO-112 (Figure F17), extending toward the edge of an interpreted sill intrusion at ~700 mbsf. Cold-seep seafloor communities are known to exist in the area above the edges of the interpreted deep sill. The mound structure is similar to the surficial mound near Site U1549, where gas hydrate is present at the seafloor, and it was thus expected that massive gas hydrate would be sampled in Hole U1552A, which is situated directly adjacent to the mostly buried mound. Like Site U1549, the association of a relatively deep sill, gas hydrates, and nearby seafloor

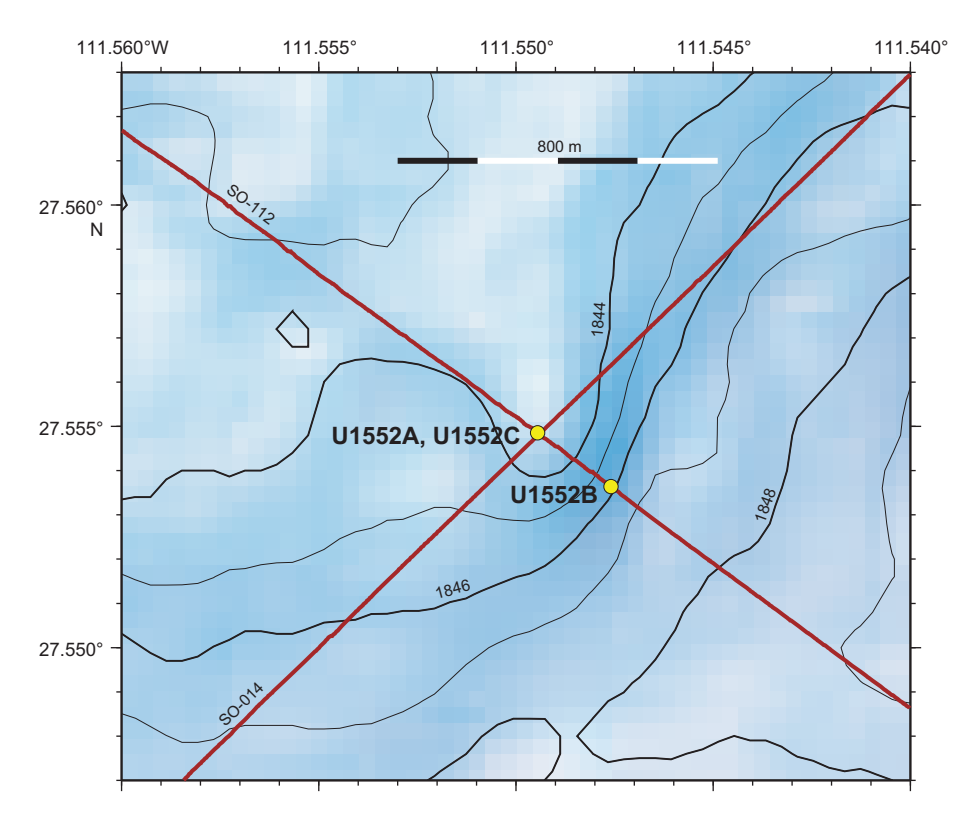


Figure F17. Bathymetric map showing Holes U1552A–U1552C, which are situated along Seismic Line SO-112. Holes U1552A and U1552B were drilled just 5 m apart from each other, so their locations are not distinguishable at the given scale. Seafloor cold-seep communities are known to be present ~200 m north and ~800 m northwest of Hole U1552A near the closed contour of 1844 m water depth. Contour lines = 1 m.

communities connects multiple components of the carbon budget in a sediment deposition system influenced by a deep sill. Therefore, the primary objectives for Site U1552 were to characterize the physical, chemical, and microbial properties of this environment and to assess (1) the influence of the deep sill on IW chemistry and gas hydrate stability, (2) the role of gas hydrate as a carbon-storage buffer, (3) the utilization of permeable pathways between the sill and the seafloor for the transport of deep thermogenic gas, and (4) the impact of lateral gradients away from the pipe structure on microbial life.

4.7.2. Operations

We cored three holes at Site U1552. Hole U1552A is located at 27°33.2906′N, 111°32.9665′W in a water depth of 1841.6 m. In Hole U1552A, we used the APC system to advance from the seafloor to a final depth of 107.5 mbsf with a recovery of 73.9 m (69%). We made formation temperature measurements at several depths with the APCT-3 tool. In Hole U1552B, located at 27°33.2885′N, 111°32.9640′W in a water depth of 1841.1 m, APC coring penetrated from the seafloor to a final depth of 55.0 mbsf and recovered 40.0 m (73%). Hole U1552B was dedicated to extensive microbial and biogeochemical sampling that required the deployment of PFTs downhole on all cores to monitor drilling fluid (seawater) contamination. Few cores from Holes U1552A and U1552B recovered gas hydrates. In Hole U1552C, located at 27°33.2181′N, 111°32.8557′W in a water depth of 1844.3 m, we deployed the APC system. Cores penetrated from the seafloor to a final depth of 99.3 mbsf and recovered 78.3 m (79%). A total of 32.6 h, or 1.4 days, were spent at Site U1552. Cores, penetration depths, core recovery, and operations schedule for all holes of Site U1552 are provided in Table T1.

4.7.3. Principal results

4.7.3.1. Lithostratigraphy

The deepest hole (Hole U1552A) recovered a 105.2 m thick succession of sediments constituting Lithostratigraphic Unit I (Figure F18). The lithologies at this site are mainly diatom clay, silty clay, and sandy silt, alternating at vertical scales of meters. This alternation occurs throughout the recovered section without any specific trend or clustering of one lithology with respect to the others. Hence, only one lithostratigraphic unit was identified. Holes U1552A and U1552C have a high level of correlation observed at the scale of a single bed. The most traceable of these beds are dominated by coarse-grained siliciclastic deposits (sand and silt). The thickest beds (~5 m) exhibit scoured bases and normally graded sand that fines upward into clayey silt to silty clay. The main biogenic components in the sediment are siliceous diatoms with rare radiolarians and silico-

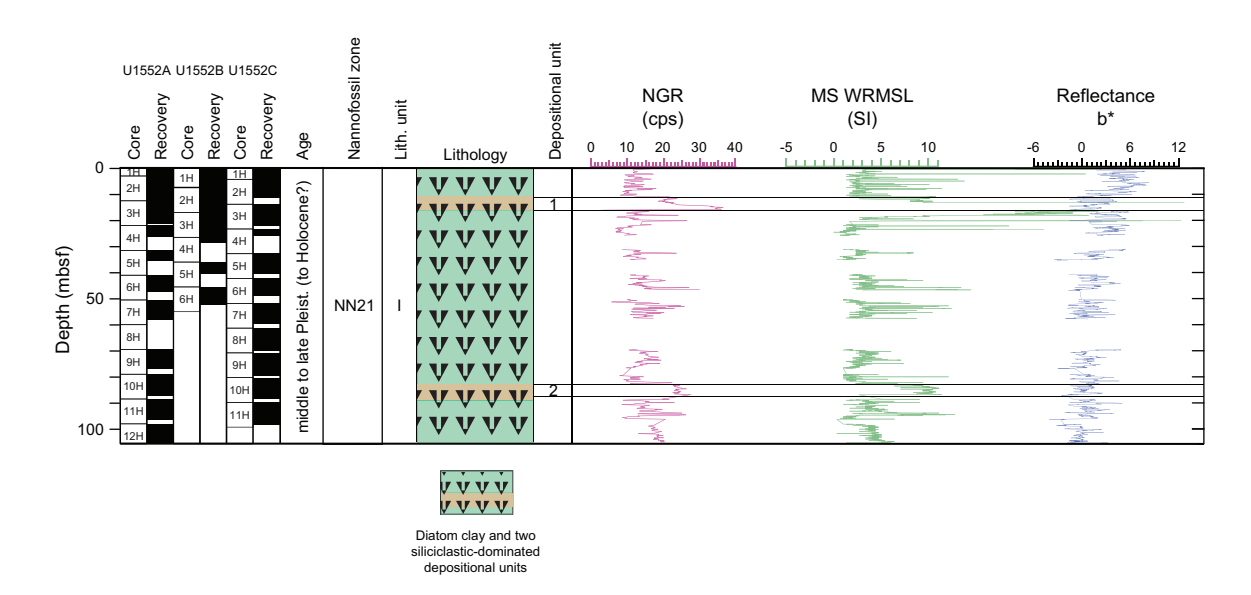


Figure F18. Lithostratigraphic column, Site U1552. Data on right are from Hole U1552A. Two distinct terrigenous beds are indicated (1 and 2), which can be correlated between Holes U1552A and U1552C. NGR = natural gamma radiation, cps = counts per second, MS = magnetic susceptibility, WRMSL = Whole-Round Multisensor Logger.

flagellates. The silt to sand fraction mainly consists of feldspar and lithic fragments with lesser quartz, micaceous, and dense minerals. Foraminifers also are a significant component in several beds. Overall, calcareous nannofossils and foraminifers are present throughout the recovered sediments, along with organic matter and plant debris. Authigenic carbonates occur only in the upper part of the site as disseminated micrite (micrometer-sized authigenic carbonate particles) or as cements in small, sandy concretions. Fossil bivalves, belonging to the Lucinidae family, were observed at the uppermost part of all three holes. Holes U1552A–U1552C recovered gas hydrates from \sim 22–32 mbsf that decomposed quickly after the cores arrived on deck. As a consequence of hydrate dissociation and gas expansion, the sediments were often disturbed. Thus, most cores displayed gas expansion cracks and voids. Complex structures were observed in Hole U1552C, including laminated diatom clay intervals that are crosscut by gray clayey silt at high angle contacts, and which locally extend down the core for as much as 1 m.

4.7.3.2. Structural geology

Coring at Site U1552 was intended to constrain differences in seismic reflection stratigraphy that were seen on either side of a seafloor mound. In the three holes cored, the sequence has beds that are generally horizontal, with no significant tilt domains or folded strata. However, gas hydrates that disturbed the sediments were found between ~22 and ~32 mbsf in all three holes at Site U1552. Overall, Hole U1552C revealed much more deformation than the other two holes, showing evidence for considerable injection and mobilization of sand along a high-angle conduit or clastic dike that continues through two sections of core. In some places, the clastic dike occupies a pre-existing fault plane. The remobilization of sand indicates that a substantial volume of sediment may have been lost from below. Other oblique faults and fractures were found in Hole U1552C at depths below the clastic dike, and we attribute these to mechanical instability caused by the presence of gas hydrates.

4.7.3.3. Biostratigraphy

At Site U1552, calcareous nannofossils are well preserved with abundant to common occurrence throughout the entire sedimentary sequence, and marine diatoms are dominant/abundant to common with good/moderate preservation. No biostratigraphic datum was defined in the succession from the (Holocene? to) late to middle Pleistocene. The occurrence of calcareous nannofossil *E. huxleyi* at the bottom of both holes dates the entire sediment sequence to (Holocene–)late–middle Pleistocene, or younger than 0.29 Ma. This age assignment is consistent with the absence of *P. lacunosa* (LAD = 0.44 Ma) and *F. reinholdii* (LAD = 0.62 Ma) in all examined samples. The estimated average sedimentation rate is >362.6 m/My (>36.26 cm/ky).

4.7.3.4. Paleomagnetism

AF demagnetization up to 20 mT was conducted with the SRM on all sediment archive-half core sections from Hole U1552A (Cores 1H–12H) and Hole U1552C (Cores 1H–11H). A small drilling-induced overprint was successfully removed following demagnetization. Inclination values after demagnetization at 20 mT cluster around 40° and 43° for Holes U1552A and U1552C, respectively, which is slightly lower than the expected GAD inclination at the latitude of the site (\sim 46.2°). Only the NRM of archive-half sections in Hole U1552B (Cores 1H–6H) was measured. A detailed analysis of the remanence of discrete samples from Holes U1552A and U1552C shows that the drilling-induced overprint was removed by 5 mT and the ChRM is in accordance with the SRM measurements. Thus, all Site U1552 cores were assigned to the normal Brunhes Chron C1n (younger than 0.78 Ma). The AMS of discrete sediment samples is characterized by a mixture of prolate and oblate behavior throughout Hole U1552A.

4.7.3.5. Inorganic geochemistry

A total of 31 IW samples were collected from the sedimentary succession at Site U1552. Based on the sulfate profile and a slight increase of methane, the SMTZ is estimated at 10 mbsf, one of the shallowest SMTZs encountered during this expedition. Concentrations of ammonium exceed 35 mM at 60 mbsf, and alkalinity remains around 150 mM below 30 mbsf and peaks at 175 mM; these values are the highest recorded at any of the Expedition 385 sites. Salinity and Cl⁻ concentrations were measured on gas hydrate—bound water from Hole U1552C. Salinity values of 2 mM and Cl⁻ values of 10.5 mM are both depleted compared to seawater (salinity = 35 mM; Cl⁻ = 559 mM). Thus, the dissociation of gas hydrate could cause anomalies in the retrieved IW as observed in the

~500 mM Cl^- concentration at 25 mbsf from Hole U1552C. Below the SMTZ, many cation concentrations (K+, Mg²⁺, Ca²⁺, etc.) increase, except the Cl⁻ concentration.

4.7.3.6. Organic geochemistry

At Site U1552, organic geochemists sampled and analyzed gas samples. In Hole U1552A, one to two headspace gas samples were analyzed per 9.5 m advance for routine hydrocarbon safety monitoring, and void gases were quantified and sampled for hydrocarbon content. In Hole U1552B, hydrocarbon analyses on headspace gas were performed, H2 and CO contents in headspace vials were measured, and void gases were quantified and sampled for hydrocarbons, H₂, and CO contents. In Hole U1552C, hydrocarbon analyses on headspace gas were performed and void gases were quantified and sampled for hydrocarbon, H₂, and CO contents as well as for shore-based analyses. Because time was running out at the conclusion of Expedition 385, no Site U1552 sediment samples were analyzed for carbon, nitrogen, or sulfur contents. This data set will be acquired via shore-based analysis and published as a separate data report. Site U1552 featured the presence of gas hydrates in the sediment column between 9 and 27 mbsf. Maximum methane concentrations in headspace gas were detected in this depth interval. C_2 – C_6 hydrocarbons were detectable at depths below ~25 mbsf without a clear trend downhole. The abundance of dissolved gas in the sediment was marked by an abundance of voids in the cores, which could represent more than 100% of the sediment recovery. Methane was dominant in these voids. H₂ and CO were detected in the void gases, but showed no clear trend downhole.

4.7.3.7. Microbiology

Site U1552 provided access to hydrate-rich sediments overlying cooler, deep sills on the northern flank of Guaymas Basin near the transition to the Sonora margin. This site presented an opportunity for microbiologists to examine microbial abundance and community structure changes throughout the gas hydrate stability zone in the sediment. Syringe samples for cell counts, 3-D structural imaging, and RNA analyses were taken on the core receiving platform, preserved or frozen, and stored for further analyses. Whole-round core samples were either stored in a -80° C freezer or temporarily stored in a $4^{\circ}-8^{\circ}$ C cold room and processed further for shore-based analyses, as described for Site U1545. Cell abundance for selected samples was determined by direct counting with an epifluorescence microscope. Cell abundance was 6.6×10^{6} cells/cm³ in bottom seawater and 1.2×10^{9} cells/cm³ in seafloor sediments. Below the seafloor, cell abundance gradually decreased to 8.1×10^{6} cells/cm³ at approximately 47 mbsf but remained above the detection limit of the protocol that we used for shipboard measurements at this deepest sample obtained from Hole U1552B.

4.7.3.8. Petrophysics

Physical properties were measured on whole-round and split core sections. The acquired data were compared between Holes U1552A and U1552C for lithostratigraphic characterization and correlation of core description information with physical properties data. Seven in situ formation temperature measurements were taken with the APCT-3 tool to calculate the geothermal gradient (262°C/km) and heat flow (222 mW/m²). Two different intervals were identified in all petrophysical parameters. From the seafloor to ~12 mbsf and at 18–87 mbsf, density, NGR, and MS are mainly constant. Peaks observed at ~18, ~58, and ~93 mbsf show increases in density, NGR, and MS values and decreases in porosity and strength values. Porosity measured on discrete MAD samples generally outlines a trend that mirrors the bulk density measurements. The shear strength regularly increases with depth. For *P*-wave velocity, values from 12 mbsf to the bottom of both Holes U1552A and U1552C predominantly show an erratic pattern typically related to voids and cracks in the cores.

5. Preliminary scientific assessment

5.1. Fundamental design of Expedition 385

Expedition 385 drilled sequences of marine sediments and mafic sills in Guaymas Basin to explore how carbon cycling within a young sedimentary rift basin is influenced by the interacting physical, chemical, and biological processes that accompany sill intrusion into organic-rich sediments.

Magmatic emplacement in Guaymas Basin is not limited to the spreading center, as at most mature mid-ocean-ridge (MOR) systems, but it extends tens of kilometers away from the divergent plate boundary, providing a diversity of sedimentary settings influenced by sill intrusion. Our drill sites followed a northwest-southeast transect across Guaymas Basin designed to capture some of this diversity, including contrasting sediment depositional regimes, sediment type, sill intrusion depth, and sill intrusion age. Sites U1545 and U1546, ~1 km from each other, share the same sequence of sediment and sedimentation history, but a ~70 m thick igneous sill has intruded the sediments beneath Site U1546, whereas Site U1545 is undisturbed, thus enabling, through comparison of cores from the two sites, direct inferences on the influence of sill intrusion on sedimentary carbon, poor water chemistry, microbial habitat, and other topics of interest to this expedition. Sites U1547 and U1548 targeted a shallow, "warm," active, and off-axis sill system within predominantly pelagic sediments. Sites U1549 and U1552 were aimed at cold-seep systems apparently driven by conduits inherited from older sills, now deeply buried by hemipelagic sediments. Site U1550 targeted sills emplaced within the northern axial graben that are subjected to a complex interaction of tectonics and hemipelagic sedimentation. The southernmost Site U1551 provided an opportunity to drill a very large, deeply buried bowl-shaped sill intruded into primarily terrigenous mass-gravity flow sediment deposits.

The drilling program at each site was designed to accommodate multidisciplinary drilling objectives by generally combining Hole A, which was dedicated to comprehensive core description, sedimentology, thermal measurements, and initial geochemistry, with Hole B, which was subjected to extensive microbiological and (bio)geochemical sampling. Whenever possible, APC or HLAPC coring was used, and we transitioned to XCB coring only when necessary to penetrate harder sediment formations and the sediment/sill contact zones. The RCB system was used for the sill intrusions to remarkable effect, providing a comparatively high core recovery through these igneous sections.

5.2. Site overview

5.2.1. Sites U1545 and U1546

The first sites drilled were Sites U1545 and U1546, ~52 km northwest of the axial graben of the northern trough. These two sites were high priority because their comparison provides an ideal opportunity to quantitatively assess the influence of sill intrusion on sediments. The two sites are separated by only ~1 km and thus contain nearly identical sedimentary strata, but they differ in that the upper ~480 m of these sediments at Site U1545 are undisturbed by sill intrusion, whereas at Site U1546, the same sedimentary sequence has been intruded by a large sill (~355-430 mbsf). The presumed paleosurface marking the intrusion event provides a reliable age of maximum ~100 ka, making the sill young enough to not have been affected by postemplacement tectonic processes but old enough to have completely cooled to the point where hydrothermalism is no longer present. These sites are also ideal for developing an age model and sedimentological framework for Guaymas Basin, owing to the near-continuous record of pelagic sediment accumulation to the total drilled depths (>500 mbsf) and to the lack of significant unconformities associated with tectonic or mass-wasting processes. Therefore, we drilled multiple holes at both sites and cored the complete sediment and sill sequence with high recovery using mainly APC or HLAPC coring within sediments and RCB coring within sills. We obtained high-quality cores well suited for (bio)geochemistry and microbiology sampling, including our best sediment record below a major sill recovered from Site U1546. We also made multiple temperature measurements at each site, enabling a very precise calculation of the thermal gradients. We reached the upper temperature limit of the available measurement tools (~80°C) at each site, demonstrating that geothermal gradients are high to a great distance from the plate boundary.

5.2.2. Sites U1547 and U1548

Sites U1547 and U1548 are situated inside and peripheral to the circular hydrothermal mound structure of Ringvent, respectively. The original intent was to recover sediments overlying a hydrothermally active, shallow sill and thereby explore the dynamics of hydrothermal circulation and the associated imprint on sediment diagenesis and microbiology. This plan was implemented but soon took a backseat to drilling into the underlying sill. The Ringvent sill at Site U1547 devel-

oped into a defining target of this expedition. Its unexpected dimensions and texturally highly variable basaltic lithology—with abundant vesicles, several generations of mineralized veins and brecciation associated with numerous sediment contacts—contrasts with the simpler and rather uniform structure of the singular massive basaltic-doleritic-gabbroic sill of Site U1546. The microbiology and organic geochemistry laboratories adapted their sediment-focused research programs and sampled the Ringvent sill for gas and solid-phase analyses, microbial cultivations, and gene and biomarker studies, whereas the petrophysics group examined the Ringvent sills' unusual morphologies and thermal properties. As a result, Ringvent Sites U1547 and U1548 catalyzed an integrated sediment-sill research program that pulled together science party members from all disciplines.

5.2.3. Sites U1549 and U1552

Site U1549 originally targeted a well-studied, active methane seep site associated with an underlying sill (Teske et al., 2021). To avoid drilling into shallow gas accumulations that surrounded the seep area, the site was moved and then served as a deep-basin off-axis reference site proximal to the Sonora margin that is unaffected by advective flux driven by a deeper sill. Site U1549 provides an instructive comparison to alternate Site U1552. Site U1552 is located proximal to the base of the Sonora margin and targeted the vicinity of a hydrate-rich methane seep situated directly above a seismically imaged conduit extending upward from a deep sill with an intrusion age likely much older than the sill at Site U1546. Both Sites U1549 and U1552 recovered a similar sedimentary sequence consisting of both marine sediments and sandy mass-gravity flow layers. Comparison of these sites provides several notable features. Massive gas hydrate was recovered in Site U1552 cores but not in Site U1549 cores, although disseminated hydrate may be present at Site U1549; hydrate recovery at Site U1552 may reflect greater proximity of the hole to the central methane conduit of this cold seep location. Interestingly, the thermal gradient at Site U1552 is substantially steeper than at Site U1549. The IW chemistry differs between the two sites, including notably higher Mg content in the IW of Site U1552 cores, which showed concentrations substantially greater than seawater. These observations suggest deeply buried sills can promote advective flux of heat and chemical compounds that are relevant to carbon cycling long after sill emplacement.

5.2.4. Site U1550

Site U1550, located in the northern axial trough of Guaymas Basin, was intended to be the "hydrothermal" representative along the transect, based on the unspoken assumption that an axial site should experience higher heat flow and higher in situ temperatures than off-axis sites. Site U1550 was drilled in the immediate vicinity of Site 481 from DSDP Leg 64, and it recovered short sill sections with veined structures and fractured morphology that resemble sill cores obtained at this location during Leg 64. Site 481 was also the only site where thermal measurements were available (Shipboard Scientific Party, 1982). However, because all Expedition 385 sites had larger thermal gradients than expected, this site turned out to be the coldest, demonstrating that an axial location is by no means an accurate predictor of hydrothermal heat flow. The recovered sedimentary column was dominated by event beds that demonstrate the influence of sediment slumping and mass-gravity flows on sedimentation within the axial trough.

5.2.5. Site U1551

Site U1551, located \sim 29 km southeast of the axial trough, targeted large, deeply buried, bowl-shaped sills intruded into dominantly terrigenous sediments deposited as mass-gravity flows. This end-member–sill-sediment system is important because it is representative of the sill systems emplaced during large igneous events and implicated in global scale catastrophes. It is also important because metals, which are more dominant in terrigenous sediments, are believed to facilitate pyrolysis and thus impact all aspects of carbon cycling driven by sill intrusion. However, thick layers of loose sands of these mass-flow sediments destabilized the holes and the site had to be abandoned prematurely after establishing two relatively shallow holes. Although the deep sills could not be reached, Site U1551, the first scientific drilling site in southeastern Guaymas Basin, yielded new insights into sediment flow and event-bed formation and highlighted the strong contrasts in sedimentary environments between northwestern and southeastern Guaymas Basin.

5.2.6. Summary

To summarize, a major scientific focus of this expedition will be the comparison of massively sedimented Sites U1545 and U1546 on the northwestern end of Guaymas Basin, both successfully drilled and recovered to depths exceeding 500 m, with Ringvent Sites U1547 and U1548, where drilling penetrated a massive sill of previously unseen proportions (potentially consisting of distinct intrusions sheets) and its shallow cover of biogenic and hemipelagic sediment with authigenic mineral precipitates. The two northwestern Sites U1545 and U1546 also provide an excellent opportunity to evaluate the consequences of a major sill intrusion into the same sedimentary sequence. The closely spaced holes of Ringvent Sites U1547 and U1548 amount to a finely resolved transect from the interior to the periphery of Ringvent, the only time in IODP history that a major sill and its impact on sediment lithology and geochemistry have been examined in such detail. In addition, results obtained from sites closer to the Sonora margin (Sites U1549 and U1552), in the northern axial trough (Site U1550), and on the southeastern flanking region (Site U1551) will explore the influence of terrigenous sedimentation, gas hydrate occurrence, and cooler formation temperatures in different combinations on the deportment of sedimentary carbon in such diverse depositional settings.

5.3. Comparison of DSDP Leg 64 and IODP Expedition 385

The scientific objectives of Expedition 385 were similar to those of Leg 64, although in the final analysis, the overlap in scientific outcomes turned out to be less than expected. Both expeditions focused on the interaction of sills with sediments and the geochemical consequences of sill emplacement, with actual overlap at axial Sites 481 and U1550. However, the contexts of the two expeditions were very different, and the overlap in site selection and scientific outcomes is actually limited. A key science objective of Leg 64 was understanding MOR magmatism in the presence of sediments. Leg 64 produced remarkable scientific results describing the influence of sill intrusion on sediments and organic compounds within the high-permeability axial trough environment. At that time, and until very recently, it was believed that all MOR magmatism was focused at the plate boundary, so there was no reason to imagine that a large variety of sill-sediment systems could actually be present in the off-axis environment of Guaymas Basin (Lizarralde et al., 2011), much less to explore how carbon cycling may vary among those settings. Whereas Leg 64 focused exclusively on (near-)axial trough sill-sediments systems, Expedition 385 expanded across the basin and provided excellent records of the sedimented slopes and rift basin floor. It explored the contrasts between different settings, including buried cool sills in thermal equilibrium with surrounding sediments (Site U1546), shallow hot sills that still function as a present-day heat source for hydrothermal fluid circulation and associated mineral precipitation and organic matter alteration (Sites U1547 and U1548), and relic systems that still promote advective flow and support cold-seep seafloor communities (Sites U1549 and U1552). Organic and inorganic geochemical profiles for Expedition 385 were generally more finely resolved, and once shore-based analyses are completed, they will include a wider spectrum of ions and hydrocarbons. Today, the greater sensitivity and wider range of stable ion analysis, coupled with high-powered analytical chemistry, provides a versatile toolbox to constrain transformations and origins of specific molecules. Leg 64 pioneered microbiological studies of the sedimentary subsurface with a cultivation survey of methanogens using hydrogen and CO₂ as substrates (Oremland et al., 1982). Cultivations, activity assays, metabolic rate measurements, DNA sequencing, genomics, and biomarker studies of the deep biosphere have taken over Expedition 385 to a large extent. Most of these techniques were not available or were in their infancy 40 y ago. However, these technical refinements do not change the fact that Leg 64 provided the fundamental outlines for understanding the Guaymas Basin subsurface, regardless of whether some of these outlines require adjustments in the near future.

5.4. Preliminary scientific assessment

Expedition results address research questions in several broad categories that are described in the expedition's *Scientific Prospectus* in the context of the major IODP scientific themes (Teske et al., 2018). At the risk of unduly simplifying this complex network of multidisciplinary research questions and hypotheses, we focus here on the central motivating question of this expedition: to what extent do sill emplacement and associated hydrothermal activity retain or mobilize subsurface

sedimentary carbon, and is this process modulated by microbial activity? The framing of this basic question was shaped on the one hand by current hypotheses that posit dramatic thermogenic carbon release from sediments in response to sill intrusion and, on the other hand, by the dominant influence of microbially mediated transformations on the fate of carbon within the upper $\sim\!200$ m of marine sediments. Expedition 385 results shed new light on aspects of both of these linked processes.

A key question related to the purely thermal impacts of sill intrusion on sedimentary carbon follows: does sill emplacement within successions of organic-rich sediments transform and mobilize buried organic matter within a broad thermal alteration zone surrounding the sill, with substantially reduced sedimentary total organic carbon (TOC) content near the sill and increased hydrocarbon concentrations above the sill? Based on shipboard data sets, the answer to this question is "less than expected" for the two types of sill/sediment settings studied at Sites U1546 and U1547. At those sites, decreasing TOC and increasing hydrocarbon concentrations are limited to a relatively narrow contact aureole, but dissolved inorganic carbon (DIC) precipitation begins as solid carbonates at the sill contact zone and extends far into the overlying sediment where abundant micrites are observed. Reduced sedimentary TOC concentrations were observed only in very close proximity to the sill/sediment contact. This contact is often marked by a solid layer of carbonates on top of the sills, suggesting either remineralization and precipitation of local sedimentary organic matter upon sill emplacement or authigenic precipitation of pore water alkalinity. Methane and volatile alkane concentrations increase substantially in close proximity to a sill and remain high within the porous rock throughout the sill, suggesting the possibility that the fairly narrow "hydrocarbon halo" that blurs into the surrounding sediment has a component that originates in the sill itself. The question whether the sill functions as a passive storage medium that returns previously adsorbed hydrocarbons, or acts as a hydrocarbon-generating net source, remains to be resolved.

More than hydrocarbons, small-scale authigenic carbonate particles (micrite) are disseminated over wide intervals in the sediment column. Sill intrusions could impact the formation of carbonates in several ways. They may make methane more available for microbially mediated increased alkalinity; they may provide cations needed to form carbonate, in particular Mg²⁺, which may explain the observed abundance of dolomite; and they create steeper thermal gradients that may accelerate the diagenetic and possibly microbially catalyzed reactions that contribute to micrite formation, pushing the micrite-forming zone upward in the sediment column.

Expedition 385 results of cored sills themselves suggest an entirely new and exciting hypothesis: sills are not just a passive medium for heat transfer to the surrounding sediment and concomitant thermal alteration of sedimentary organic matter; instead, the sill matrix itself plays a chemical role as a precipitation zone and storage medium for carbon. Consistent observations of calcite precipitation in vesicles and veins in host sills suggest that sills catalyze carbon precipitation and thus carbon sequestration within the sill itself. The carbon source remains to be identified; it may be sediment-bound pore water or seawater entrapped during sill emplacement or circulating through the porous sill, or perhaps it is of a more juvenile (magmatic) origin. Parallel observations of large amounts of methane in porous sill host rock indicate a major carbon reservoir and suggest that sills may act as a methane capacitor, with limited diffusion into adjacent sediment. The sources of the sill-hosted pore space methane—microbial production from DIC and H₂, methanogenic degradation of LMW organic compounds, or hydrothermal reactions without direct microbial participation—remain to be identified. Calcite and methane represent the opposite redox extremes of carbon, but the sill host rock also needs to be examined closely for chemically intermediate carbon forms, such as graphite, to complete the carbon inventory.

Carbon sources and transformation pathways in the subseafloor biosphere are often microbially mediated, which leads to specific microbiological research questions. How does the thermal impact of emplaced sills influence microbial diagenetic reactions, for example ammonia or alkalinity generation from organic matter decomposition or sulfate depletion by LMW-oxidizing sulfate-reducing microorganisms? Is there a connection between geothermal gradient and anaerobic metabolism? Metabolic acceleration could be a direct thermal response or indirectly triggered when warmer temperatures help to release LMW compounds from complex, buried organic

matter. On the other hand, heat stress could reduce microbial activity, as suggested by the much-reduced alkalinity and ammonia concentrations at the comparatively hot Ringvent sites, compared to higher concentrations at the cooler northwestern sites and cold seep sites. Sulfate depletion at the hot Ringvent sites could result from abiotic sulfate reduction at the hot sill—sediment interface, contrasting with microbial sulfate reduction and depletion at cooler sediment-hosted SMTZs at other sites. Interestingly, shipboard cell counts show that microbial cell numbers in the sediments are strongly affected by the local thermal gradient and decrease rapidly toward greater depths; the slope of declining cell numbers appears to be steeper at the hot Ringvent sites compared to other sites. Cell counts in the upper sediment column remain at least near or above cell counts for passive continental margins without hydrothermal activity. Thus, the expedition results place the general microbial questions that populated the proposal (thermal and chemical limits of life, limits of specific metabolic pathways, etc.) into a specific hypothesis-generating context that will stimulate and guide multidisciplinary postexpedition research.

The generally high quality and high degree of completeness of the acquired data sets open up opportunities for interdisciplinary and multidisciplinary collaborations on studies that will keep producing results and new insights far into the future. For example, it will be possible for the first time in scientific ocean drilling history to systematically explore correlations of cell abundance, community composition, and activity with geothermal gradients within the relevant thermal range (as high as ~80°-100°C) and over a wide range of lithologic and geochemical conditions using multiple sites and holes from the same region. Another area of highly promising data integration will be the combined lithology and geochemistry of the sediment-sill transition. Multiple examples were recovered during Expedition 385, where previously only a single transition (the top of the major sill in Hole 481A at ~170 m subbottom depth) was available in any reasonable degree of completeness. The mineralogy, geochemistry, and microbiology of the massive sills themselves are now within reach for individual studies as well as for collaborative ventures because the shipboard microbiology group readjusted their originally sediment-focused sampling program to cover the interior of sills as well. The hydrothermal influence on mineral dissolution, authigenic mineral precipitation, and mineral transformations can be assessed in multiple sediment columns where suitable thermal gradient information, high sediment recovery, and high-quality analysis of the sediment composition and mineral phases coincide.

References

- Aarnes, I., Planke, S., Trulsvik, M., and Svensen, H., 2015. Contact metamorphism and thermogenic gas generation in the Vøring and Møre Basins, offshore Norway, during the Paleocene–Eocene Thermal Maximum. *Journal of the Geological Society (London, UK)*, 172(5):588–598. https://doi.org/10.1144/jgs2014-098
- Aarnes, I., Svensen, H., Connolly, J.A.D., and Podladchikov, Y.Y., 2010. How contact metamorphism can trigger global climate changes: modeling gas generation around igneous sills in sedimentary basins. *Geochimica et Cosmochimica Acta*, 74(24):7179–7195. https://doi.org/10.1016/j.gca.2010.09.011
- Aarnes, I., Svensen, H., Polteau, S., and Planke, S., 2011. Contact metamorphic devolatilization of shales in the Karoo Basin, South Africa, and the effects of multiple sill intrusions. *Chemical Geology*, 281(3):181–194. https://doi.org/10.1016/j.chemgeo.2010.12.007
- Berndt, C., Hensen, C., Mortera-Gutierrez, C., Sarkar, S., Geilert, S., Schmidt, M., Liebetrau, V., et al., 2016. Rifting under steam—how rift magmatism triggers methane venting from sedimentary basins. *Geology*, 44(9):767–770. https://doi.org/10.1130/G38049.1
- Biddle, J.F., Cardman, Z., Mendlovitz, H., Albert, D.B., Lloyd, K.G., Boetius, A., and Teske, A., 2012. Anaerobic oxidation of methane at different temperature regimes in Guaymas Basin hydrothermal sediments. *The ISME Journal*, 6(5):1018–1031. https://doi.org/10.1038/ismej.2011.164
- Bralower, T.J., 2008. Volcanic cause of catastrophe. *Nature*, 454(7202):285–287. https://doi.org/10.1038/454285a Callaghan, A.V., Davidova, I.A., Savage-Ashlock, K., Parisi, V.A., Gieg, L.M., Suflita, J.M., Kukor, J.J., and Wawrik, B., 2010. Diversity of benzyl- and alkylsuccinate synthase genes in hydrocarbon-impacted environments and enrichment cultures. *Environmental Science & Technology*, 44(19):7287–7294. https://doi.org/10.1021/es1002023
- Calvert, S.E., 1966. Origin of diatom-rich, varved sediments from the Gulf of California. *The Journal of Geology*, 74(5):546–565. http://www.jstor.org/stable/30059298
- Curray, J.R., Moore, D., Aguayo, E., Aubry, M., Einsele, G., Fornari, D., Gieskes, J., Guerrero, J., Kastner, M., and Kelts, K., 1979. Leg 64 seeks evidence on development of basins. *Geotimes*, 24(7):18–20.
- Curray, J.R., Moore, D.G., et al., 1982. *Initial Reports of the Deep Sea Drilling Project*, 64: Washington, DC (US Government Printing Office). https://10.2973/dsdp.proc.64.1982
- Didyk, B.M., and Simoneit, B.R.T., 1989. Hydrothermal oil of Guaymas Basin and implications for petroleum formation mechanisms. *Nature*, 342(6245):65–69. https://doi.org/10.1038/342065a0

- Dombrowski, N., Teske, A.P., and Baker, B.J., 2018. Expansive microbial metabolic versatility and biodiversity in dynamic Guaymas Basin hydrothermal sediments. *Nature Communications*, 9(1):4999. https://doi.org/10.1038/s41467-018-07418-0
- Edgcomb, V.P., Molyneaux, S.J., Böer, S., Wirsen, C.O., Saito, M., Atkins, M.S., Lloyd, K., and Teske, A., 2007. Survival and growth of two heterotrophic hydrothermal vent archaea, *Pyrococcus* strain GB-D and *Thermococcus fumicolans*, under low pH and high sulfide concentrations in combination with high temperature and pressure regimes. *Extremophiles*, 11(2):329–342. https://doi.org/10.1007/s00792-006-0043-0
- Einsele, G., 1982. Mechanism of sill intrusion into soft sediment and expulsion of pore water. *In Curray, J.R., Moore, D.G., et al., Initial Reports of the Deep Sea Drilling Project,* 64: Washington, DC (US Government Printing Office), 1169–1176. https://doi.org/10.2973/dsdp.proc.64.156.1982
- Einsele, G., Gieskes, J.M., Curray, J., Moore, D.M., Aguayo, E., Aubry, M.-P., Fornari, D., et al., 1980. Intrusion of basaltic sills into highly porous sediments, and resulting hydrothermal activity. *Nature*, 283(5746):441–445. https://doi.org/10.1038/283441a0
- Elsgaard, L., Isaksen, M.F., Jørgensen, B.B., Alayse, A.-M., and Jannasch, H.W., 1994. Microbial sulfate reduction in deep-sea sediments at the Guaymas Basin hydrothermal vent area: influence of temperature and substrates. *Geochimica et Cosmochimica Acta*, 58(16):3335–3343. https://doi.org/10.1016/0016-7037(94)90089-2
- Fisher, A.T., and Narasimhan, T.N., 1991. Numerical simulations of hydrothermal circulation resulting from basalt intrusions in a buried spreading center. *Earth and Planetary Science Letters*, 103(1–4):100–115. https://doi.org/10.1016/0012-821X(91)90153-9
- Galerne, C.Y., and Hasenclever, J., 2019. Distinct degassing pulses during magma invasion in the stratified Karoo Basin—new insights from hydrothermal fluid flow modeling. *Geochemistry, Geophysics, Geosystems*, 20(6):2955–2984. https://doi.org/10.1029/2018GC008120
- Galimov, E.M., and Simoneit, B.R.T., 1982. Geochemistry of interstitial gases in sedimentary deposits of the Gulf of California, Deep Sea Drilling Project Leg 64. *In* Curray, J.R., Moore, D.G., et al., *Initial Reports of the Deep Sea Drilling Project*, 64: Washington, DC (US Government Printing Office), 781–787. https://doi.org/10.2973/dsdp.proc.64.124.1982
- Geilert, S., Hensen, C., Schmidt, M., Liebetrau, V., Scholz, F., Doll, M., Deng, L., et al., 2018. Transition from hydrothermal vents to cold seeps records timing of carbon release in the Guaymas Basin, Gulf of California. *Biogeosciences Discussion*. https://doi.org/10.5194/bg-2018-12
- Gieskes, J.M., Kastner, M., Einsele, G., Kelts, K., and Niemitz, J., 1982. Hydrothermal activity in the Guaymas Basin, Gulf of California: a synthesis. *In Curray, J.R., Moore, D.G., et al., Initial Reports of the Deep Sea Drilling Project, 64*: Washington, DC (US Government Printing Office), 1159–1167. https://doi.org/10.2973/dsdp.proc.64.155.1982
- Goetz, F.E., and Jannasch, H.W., 1993. Aromatic hydrocarbon-degrading bacteria in the petroleum-rich sediments of the Guaymas Basin hydrothermal vent site: preference for aromatic carboxylic acids. *Geomicrobiology Journal*, 11(1):1–18. https://doi.org/10.1080/01490459309377928
- González-Fernández, A., Dañobeitia, J.J., Delgado-Argote, L.A., Michaud, F., Córdoba, D., and Bartolomé, R., 2005. Mode of extension and rifting history of upper Tiburón and upper Delfín Basins, northern Gulf of California. *Journal of Geophysical Research: Solid Earth*, 110(B1):B01313. https://doi.org/10.1029/2003JB002941
- Gundersen, J.K., Jorgensen, B.B., Larsen, E., and Jannasch, H.W., 1992. Mats of giant sulphur bacteria on deep-sea sediments due to fluctuating hydrothermal flow. *Nature*, 360(6403):454–456. https://doi.org/10.1038/360454a0
- Gutierrez, T., Biddle, J.F., Teske, A., and Aitken, M.D., 2015. Cultivation-dependent and cultivation-independent characterization of hydrocarbon-degrading bacteria in Guaymas Basin sediments. Frontiers in Microbiology, 6:695. https://doi.org/10.3389/fmicb.2015.00695
- Higgins, J.A., and Schrag, D.P., 2006. Beyond methane: towards a theory for the Paleocene–Eocene Thermal Maximum. *Earth and Planetary Science Letters*, 245(3):523–537. https://doi.org/10.1016/j.epsl.2006.03.009
- Holler, T., Widdel, F., Knittel, K., Amann, R., Kellermann, M.Y., Hinrichs, K.-U., Teske, A., Boetius, A., and Wegener, G., 2011. Thermophilic anaerobic oxidation of methane by marine microbial consortia. *The ISME Journal*, 5(12):1946–1956. https://doi.org/10.1038/ismej.2011.77
- House, C.H., Cragg, B.A., Teske, A., and the Leg 201 Scientific Party, 2003. Drilling contamination tests during ODP Leg 201 using chemical and particulate tracers. In D'Hondt, S.L., Jørgensen, B.B., and Miller, D.J. (Eds.), Proceedings of the Ocean Drilling Program, Initial Reports, 201: College Station, TX (Ocean Drilling Program). https://doi.org/10.2973/odp.proc.ir.201.102.2003
- Iyer, K., Rüpke, L., and Galerne, C.Y., 2013. Modeling fluid flow in sedimentary basins with sill intrusions: implications for hydrothermal venting and climate change. *Geochemistry, Geophysics, Geosystems*, 14(12):5244–5262. https://doi.org/10.1002/2013GC005012
- Iyer, K., Schmid, D.W., Planke, S., and Millett, J., 2017. Modelling hydrothermal venting in volcanic sedimentary basins: impact on hydrocarbon maturation and paleoclimate. *Earth and Planetary Science Letters*, 467:30–42. https://doi.org/10.1016/j.epsl.2017.03.023
- Jørgensen, B.B., Isaksen, M.F., and Jannasch, H.W., 1992. Bacterial sulfate reduction above 100°C in deep-sea hydrothermal vent sediments. *Science*, 258(5089):1756–1757. https://doi.org/10.1126/science.258.5089.1756
- Jørgensen, B.B., Zawacki, L.X., and Jannasch, H.W., 1990. Thermophilic bacterial sulfate reduction in deep-sea sediments at the Guaymas Basin hydrothermal vent site (Gulf of California). Deep Sea Research, Part A: Oceanographic Research Papers, 37(4):695-710. https://doi.org/10.1016/0198-0149(90)90099-H
- Kastner, M., 1982. Evidence for two distinct hydrothermal systems in the Guaymas Basin. *In Curray, J.R., Moore, D.G.,* et al., *Initial Reports of the Deep Sea Drilling Project,* 64: Washington, DC (US Government Printing Office), 1143–1157. https://doi.org/10.2973/dsdp.proc.64.154.1982
- Kawka, O.E., and Simoneit, B.R.T., 1987. Survey of hydrothermally-generated petroleums from the Guaymas Basin spreading center. *Organic Geochemistry*, 11(4):311–328. https://doi.org/10.1016/0146-6380(87)90042-8

- Kelts, K., Curray, J.R., and Moore, D.G., 1982. Introduction and explanatory notes. *In* Curray, J.R., Moore, D.G., et al., *Initial Reports of the Deep Sea Drilling Project*, 64: Washington, DC (US Government Printing Office), 5–26. https://doi.org/10.2973/dsdp.proc.64.101.1982
- Kniemeyer, O., Musat, F., Sievert, S.M., Knittel, K., Wilkes, H., Blumenberg, M., Michaelis, W., et al., 2007. Anaerobic oxidation of short-chain hydrocarbons by marine sulphate-reducing bacteria. *Nature*, 449(7164):898–901. https://doi.org/10.1038/nature06200
- Krukenberg, V., Harding, K., Richter, M., Glöckner, F.O., Gruber-Vodicka, H.R., Adam, B., Berg, J.S., et al., 2016. Candidatus Desulfofervidus auxilii, a hydrogenotrophic sulfate-reducing bacterium involved in the thermophilic anaerobic oxidation of methane. Environmental Microbiology, 18(9):3073–3091. https://doi.org/10.1111/1462-2920.13283
- Kurr, M., Huber, R., König, H., Jannasch, H.W., Fricke, H., Trincone, A., Kristjansson, J.K., and Stetter, K.O., 1991.
 Methanopyrus kandleri, gen. and sp. nov. represents a novel group of hyperthermophilic methanogens, growing at 110°C. Archives of Microbiology, 156(4):239–247. https://doi.org/10.1007/BF00262992
- Laso-Pérez, R., Wegener, G., Knittel, K., Widdel, F., Harding, K.J., Krukenberg, V., Meier, D.V., et al., 2016. Thermophilic archaea activate butane via alkyl-coenzyme M formation. *Nature*, 539(7629):396–401. https://doi.org/10.1038/nature20152
- Lever, M.A., Alperin, M., Engelen, B., Inagaki, F., Nakagawa, S., Steinsbu, B.O., and Teske, A., 2006. Trends in basalt and sediment core contamination during IODP Expedition 301. *Geomicrobiology Journal*, 23(7):517–530. https://doi.org/10.1080/01490450600897245
- Lizarralde, D., Axen, G.J., Brown, H.E., Fletcher, J.M., González-Fernández, A., Harding, A.J., Holbrook, W.S., et al., 2007. Variation in styles of rifting in the Gulf of California. *Nature*, 448(7152):466–469. https://doi.org/10.1038/nature06035
- Lizarralde, D., Soule, S.A., Seewald, J.S., and Proskurowski, G., 2011. Carbon release by off-axis magmatism in a young sedimented spreading centre. *Nature Geoscience*, 4:50–54. https://doi.org/10.1038/ngeo1006
- Martens, C.S., 1990. Generation of short chain acid anions in hydrothermally altered sediments of the Guaymas Basin, Gulf of California. *Applied Geochemistry*, 5(1):71–76. https://doi.org/10.1016/0883-2927(90)90037-6
- McKay, L., Klokman, V.W., Mendlovitz, H.P., LaRowe, D.E., Hoer, D.R., Albert, D., Amend, J.P., and Teske, A., 2016. Thermal and geochemical influences on microbial biogeography in the hydrothermal sediments of Guaymas Basin, Gulf of California. *Environmental Microbiology Reports*, 8(1):150–161. https://doi.org/10.1111/1758-2229.12365
- McKay, L.J., MacGregor, B.J., Biddle, J.F., Albert, D.B., Mendlovitz, H.P., Hoer, D.R., Lipp, J.S., Lloyd, K.G., and Teske, A.P., 2012. Spatial heterogeneity and underlying geochemistry of phylogenetically diverse orange and white *Beggiatoa* mats in Guaymas Basin hydrothermal sediments. *Deep Sea Research, Part I: Oceanographic Research Papers*, 67:21–31. https://doi.org/10.1016/j.dsr.2012.04.011
- Merkel, A.Y., Huber, J.A., Chernyh, N.A., Bonch-Osmolovskaya, E.A., and Lebedinsky, A.V., 2013. Detection of putatively thermophilic anaerobic methanotrophs in diffuse hydrothermal vent fluids. Applied and Environmental Microbiology, 79(3):915–923. https://doi.org/10.1128/AEM.03034-12
- Miller, N.C., and Lizarralde, D., 2013. Thick evaporites and early rifting in the Guaymas Basin, Gulf of California. *Geology*, 41(2):283–286. https://doi.org/10.1130/G33747.1
- Núñez-Useche, F., Canet, C., Liebetrau, V., Puig, T.P., Ponciano, A.C., Alfonso, P., Berndt, C., Hensen, C., Mortera-Gutierrez, C., and Rodríguez-Díaz, A.A., 2018. Redox conditions and authigenic mineralization related to cold seeps in central Guaymas Basin, Gulf of California. *Marine and Petroleum Geology*, 95:1–15. https://doi.org/10.1016/j.marpetgeo.2018.04.010
- Oremland, R.S., Culbertson, C., and Simoneit, B.R.T., 1982. Methanogenic activity in sediment from Leg 64, Gulf of California. *In Curray*, J.R., Moore, D.G., et al., *Initial Reports of the Deep Sea Drilling Project*, 64: Washington, DC (US Government Printing Office), 759–762. https://doi.org/10.2973/dsdp.proc.64.122.1982
- Pearson, A., Seewald, J.S., and Eglinton, T.I., 2005. Bacterial incorporation of relict carbon in the hydrothermal environment of Guaymas Basin. *Geochimica et Cosmochimica Acta*, 69(23):5477–5486. https://doi.org/10.1016/j.gca.2005.07.007
- Persaud, P., Stock, J.M., Steckler, M.S., Martín-Barajas, A., Diebold, J.B., González-Fernández, A., and Mountain, G.S., 2003. Active deformation and shallow structure of the Wagner, Consag, and Delfín Basins, northern Gulf of California, Mexico. *Journal of Geophysical Research: Solid Earth*, 108(B7):2355. https://doi.org/10.1029/2002JB001937
- Peter, J.M., Peltonen, P., Scott, S.D., Simoneit, B.R.T., and Kawka, O.E., 1991. ¹⁴C ages of hydrothermal petroleum and carbonate in Guaymas Basin, Gulf of California: implications for oil generation, expulsion, and migration. *Geology*, 19(3):253–256. https://doi.org/10.1130/0091-7613(1991)019<0253:CAOHPA>2.3.CO;2
- Ramírez, G.A., McKay, L.J., Fields, M.W., Buckley, A., Mortera, C., Hensen, C., Ravelo, A.C., and Teske, A.P., 2020. The Guaymas Basin subseafloor sedimentary archaeome reflects complex environmental histories. *iScience*, 23(9):101459. https://doi.org/10.1016/j.isci.2020.101459
- Rueter, P., Rabus, R., Wilkest, H., Aeckersberg, F., Rainey, F.A., Jannasch, H.W., and Widdel, F., 1994. Anaerobic oxidation of hydrocarbons in crude oil by new types of sulphate-reducing bacteria. *Nature*, 372(6505):455–458. https://doi.org/10.1038/372455a0
- Saunders, A.D., Fornari, D.J., Joron, J.-L., Tarney, J., and Treuil, M., 1982. Geochemistry of basic igneous rocks, Gulf of California, Deep Sea Drilling Project Leg 64. *In* Curray, J.R., Moore, D.G., et al., *Initial Reports of the Deep Sea Drilling Project*, 64: Washington, DC (US Government Printing Office), 595–642. https://doi.org/10.2973/dsdp.proc.64.112.1982
- Saxby, J.D., and Stephenson, L.C., 1987. Effect of anigneous intrusion on oil shale at Rundle (Australia). *Chemical Geology*, 63(1):1–16. https://doi.org/10.1016/0009-2541(87)90068-4

- Seewald, J.S., Seyfried, W.E., and Thornton, E.C., 1990. Organic-rich sediment alteration: an experimental and theoretical study at elevated temperatures and pressures. *Applied Geochemistry*, 5(1):193–209. https://doi.org/10.1016/0883-2927(90)90048-A
- Seitz, K.W., Dombrowski, N., Eme, L., Spang, A., Lombard, J., Sieber, J.R., Teske, A.P., Ettema, T.J.G., and Baker, B.J., 2019. Asgard archaea capable of anaerobic hydrocarbon cycling. *Nature Communications*, 10(1):1822. https://doi.org/10.1038/s41467-019-09364-x
- Sell, B., Ovtcharova, M., Guex, J., Bartolini, A., Jourdan, F., Spangenberg, J.E., Vicente, J.-C., and Schaltegger, U., 2014. Evaluating the temporal link between the Karoo LIP and climatic-biologic events of the Toarcian stage with high-precision U-Pb geochronology. Earth and Planetary Science Letters, 408:48-56. https://doi.org/10.1016/j.epsl.2014.10.008
- Shipboard Scientific Party, 1982. Guaymas Basin; Sites 477, 478, and 481. In Curray, J.R., Moore, D.G., et al. (Ed.), Initial Reports of the Deep Sea Drilling Project, 64: Washington, DC (US Government Printing Office), 211–415. https://doi.org/10.2973/dsdp.proc.64.104.1982
- Simoneit, B.R.T., and Bode, G.R., 1982. Appendix II: carbon/carbonate and nitrogen analyses, Leg 64, Gulf of California. *In Curray, J.R., Moore, D.G., et al., Initial Reports of the Deep Sea Drilling Project,* 64: Washington, DC (US Government Printing Office), 1303–1305. https://doi.org/10.2973/dsdp.proc.64.app2.1982
- Simoneit, B.R.T., Brenner, S., Peters, K.E., and Kaplan, I.R., 1978. Thermal alteration of Cretaceous black shale by basaltic intrusions in the eastern Atlantic. *Nature*, 273(5663):501–504. https://doi.org/10.1038/273501a0
- Simoneit, B.R.T., Brenner, S., Peters, K.E., and Kaplan, I.R., 1981. Thermal alteration of Cretaceous black shale by diabase intrusions in the eastern Atlantic—II. Effects on bitumen and kerogen. *Geochimica et Cosmochimica Acta*, 45(9):1581–1602. https://doi.org/10.1016/0016-7037(81)90287-8
- Simoneit, B.R.T., and Lonsdale, P.F., 1982. Hydrothermal petroleum in mineralized mounds at the seabed of Guaymas Basin. *Nature*, 295(5846):198–202. https://doi.org/10.1038/295198a0
- Stock, J.M., and Lee, J., 1994. Do microplates in subduction zones leave a geological record? *Tectonics*, 13(6):1472–1487. https://doi.org/10.1029/94TC01808
- Sutherland, F.H., Kent, G.M., Harding, A.J., Umhoefer, P.J., Driscoll, N.W., Lizarralde, D., Fletcher, J.M., et al., 2012. Middle Miocene to early Pliocene oblique extension in the southern Gulf of California. *Geosphere*, 8(4):752–770. https://doi.org/10.1130/GES00770.1
- Svensen, H., Planke, S., Chevallier, L., Malthe-Sørenssen, A., Corfu, F., and Jamtveit, B., 2007. Hydrothermal venting of greenhouse gases triggering early Jurassic global warming. *Earth and Planetary Science Letters*, 256(3):554–566. https://doi.org/10.1016/j.epsl.2007.02.013
- Svensen, H., Planke, S., Malthe-Sørenssen, A., Jamtveit, B., Myklebust, R., Rasmussen Eidem, T., and Rey, S.S., 2004. Release of methane from a volcanic basin as a mechanism for initial Eocene global warming. *Nature*, 429(6991):542–545. https://doi.org/10.1038/nature02566
- Svensen, H., Planke, S., Polozov, A.G., Schmidbauer, N., Corfu, F., Podladchikov, Y.Y., and Jamtveit, B., 2009a. Siberian gas venting and the end-Permian environmental crisis. *Earth and Planetary Science Letters*, 277(3–4):490–500. https://doi.org/10.1016/j.epsl.2008.11.015
- Svensen, H., Schmidbauer, N., Roscher, M., Stordal, F., and Planke, S., 2009b. Contact metamorphism, halocarbons, and environmental crises of the past. *Environmental Chemistry*, 6(6):466–471. https://doi.org/10.1071/EN09118
- Takai, K., Nakamura, K., Toki, T., Tsunogai, U., Miyazaki, M., Miyazaki, J., Hirayama, H., Nakagawa, S., Nunoura, T., and Horikoshi, K., 2008. Cell proliferation at 122°C and isotopically heavy CH₄ production by a hyperthermophilic methanogen under high-pressure cultivation. *Proceedings of the National Academy of Sciences of the United States of America*, 105(31):10949–10954. https://doi.org/10.1073/pnas.0712334105
- Teske, A., Callaghan, A.V., and LaRowe, D.E., 2014. Biosphere frontiers of subsurface life in the sedimented hydrothermal system of Guaymas Basin. Frontiers in Microbiology, 5:362. https://doi.org/10.3389/fmicb.2014.00362
- Teske, A., Edgcomb, V., Rivers, A.R., Thompson, J.R., de Vera Gomez, A., Molyneaux, S.J., and Wirsen, C.O., 2009. A molecular and physiological survey of a diverse collection of hydrothermal vent *Thermococcus* and *Pyrococcus* isolates. *Extremophiles*, 13(6):905–915. https://doi.org/10.1007/s00792-009-0278-7
- Teske, A., Hinrichs, K.-U., Edgcomb, V., de Vera Gomez, A., Kysela, D., Sylva, S.P., Sogin, M.L., and Jannasch, H.W., 2002. Microbial diversity of hydrothermal sediments in the Guaymas Basin: evidence for anaerobic methanotrophic communities. *Applied and Environmental Microbiology*, 68(4):1994–2007. https://doi.org/10.1128/AEM.68.4.1994-2007.2002
- Teske, A., Lizarralde, D., and Höfig, T.W., 2018. Expedition 385 Scientific Prospectus: Guaymas Basin Tectonics and Biosphere. International Ocean Discovery Program. https://doi.org/10.14379/iodp.sp.385.2018
- Teske, A., McKay, L.J., Ravelo, A.C., Aiello, I., Mortera, C., Núñez-Useche, F., Canet, C., et al., 2019. Characteristics and evolution of sill-driven off-axis hydrothermalism in Guaymas Basin the Ringvent site. *Scientific Reports*, 9(1):13847. https://doi.org/10.1038/s41598-019-50200-5
- Teske, A., Wegener, G., Chanton, J.P., White, D., MacGregor, B., Hoer, D., de Beer, D., et al., 2021. Microbial communities under distinct thermal and geochemical regimes in axial and off-axis sediments of Guaymas Basin. *Frontiers in Microbiology*, 12:633649. https://doi.org/10.3389/fmicb.2021.633649
- Teske, A.P., 2006. Microbial communities of deep marine subsurface sediments; molecular and cultivation surveys. *Geomicrobiology Journal*, 23(6):357–368. https://doi.org/10.1080/01490450600875613
- Turgeon, S.C., and Creaser, R.A., 2008. Cretaceous Oceanic Anoxic Event 2 triggered by a massive magmatic episode. Nature, 454(7202):323–326. https://doi.org/10.1038/nature07076
- van Andel, T.H., 1964. Recent marine sediments of Gulf of California. *In* van Andel, T.H., and Shor, G.G., Jr. (Eds.), *Marine Geology of the Gulf of California: A Symposium.* AAPG Memoir, 3:216–310.

- Von Damm, K.L., Edmond, J.M., Grant, B., Measures, C.I., Walden, B., and Weiss, R.F., 1985. Chemistry of submarine hydrothermal solutions at 21°N, East Pacific Rise. *Geochimica et Cosmochimica Acta*, 49(11):2197–2220. https://doi.org/10.1016/0016-7037(85)90222-4
- Wankel, S.D., Germanovich, L.N., Lilley, M.D., Genc, G., DiPerna, C.J., Bradley, A.S., Olson, E.J., and Girguis, P.R., 2011. Influence of subsurface biosphere on geochemical fluxes from diffuse hydrothermal fluids. *Nature Geoscience*, 4(7):461–468. https://doi.org/10.1038/ngeo1183
- Weber, A., and Jørgensen, B.B., 2002. Bacterial sulfate reduction in hydrothermal sediments of the Guaymas Basin, Gulf of California, Mexico. *Deep Sea Research*, *Part I: Oceanographic Research*, 49(5):827–841. https://doi.org/10.1016/S0967-0637(01)00079-6
- Whelan, J.K., and Hunt, J.M., 1982. C₁–C₈ hydrocarbons in Leg 64 sediments, Gulf of California. *In Curray, J.R.,* Moore, D.G., et al., *Initial Reports of the Deep Sea Drilling Project,* 64: Washington, DC (US Government Printing Office), 763–780. https://doi.org/10.2973/dsdp.proc.64.123.1982
- Whelan, J.K., Simoneit, B.R.T., and Tarafa, M.E., 1988. C_1 – C_8 hydrocarbons in sediments from Guaymas Basin, Gulf of California—comparison to Peru margin, Japan Trench and California borderlands. *Organic Geochemistry*, 12(2):171–194. https://doi.org/10.1016/0146-6380(88)90253-7